
Beam-based alignment at the Cooler Synchrotron COSY for an Electric Dipole Moment measurement of charged particles

Von der Fakultät für Mathematik, Informatik und
Naturwissenschaften der RWTH Aachen University zur
Erlangung des akademischen Grades eines Doktors der
Naturwissenschaften genehmigte Dissertation

vorgelegt von
Tim Wagner, M. Sc.
aus Meschede

Berichter: Univ.-Prof. Dr. rer. nat. Jörg Pretz
Univ.-Prof. Dr. rer. nat. Thomas Stöhlker

Tag der mündlichen Prüfung: 31. August 2021

Diese Dissertation ist auf den Internetseiten der
Universitätsbibliothek verfügbar.

Abstract

One of the unsolved puzzles of physics is the matter over antimatter dominance in our universe. The required matter-antimatter asymmetry is not explained within the standard model of particle physics and cosmology and current measurements, thus more CP violating effects are needed to explain that discrepancy. One of the possible sources for CP violation is a non-vanishing Electric Dipole Moment (EDM) of elementary particles. So far, all the measurements only provide upper limits and are consistent with a vanishing EDM. The Jülich Electric Dipole moment Investigations (JEDI) collaboration wants to directly measure the EDM of the proton and deuteron, which has not been done so far. This is done in the Cooler Synchrotron (COSY) storage ring with a Radio Frequency (RF) Wien filter to observe a buildup of the vertical polarization proportional to the EDM. In addition the Magnetic Dipole Moment (MDM), which is orders of magnitude larger than the EDM, also influences the polarization of the stored beam. It is possible for the MDM to mimic the effect of an EDM in a non perfect machine. In order to eliminate that systematic effect one has to compare simulations to the measured data. To simulate the accelerator it is required to know the exact positions of all elements in the ring with a high precision. Therefore an alignment campaign of the magnets has been done. Unfortunately the Beam Position Monitors (BPMs), which are essential to know how the beam passes the magnets, could not be aligned with that campaign. Thus a dedicated method to align the BPMs was developed and implemented to measure their alignment. The chosen method is the beam-based alignment method, which is aligning the BPMs with respect to the quadrupole magnetic centers and thus also within the coordinate system of all the magnets. The beam-based alignment measurements show a shift of the BPMs of up to 5 mm with respect to their ideal position, which has been corrected for. In addition, now the correction of the orbit to the optimal position (zero) is better and needs less steering magnets, as one does not have to steer against the beam passing off-center inside the quadrupoles anymore.

Zusammenfassung

Eines der ungelösten Probleme in der Physik ist die Dominanz der Materie über Anti-Materie. Die dafür erforderliche Materie-Anti-Materie Asymmetrie kann nicht mit dem Standard Modell der Teilchenphysik und Kosmologie erklärt werden. Daher sind weitere CP verletzende Effekte erforderlich, um diese Diskrepanz zu erklären. Eine mögliche Quelle für weitere CP Verletzung ist ein nicht verschwindendes Elektrisches Dipolmoment (EDM) von elementaren Teilchen. Bisher ergeben alle Messungen des EDM elementarer Teilchen nur obere Schranken, welche kompatibel mit einem verschwindendem EDM sind. Die Jülich Electric Dipole moment Investigations (JEDI) Kollaboration hat es als Ziel, das EDM von dem Proton und dem Deuteron direkt zu messen, was bisher noch nicht geschafft wurde. Diese Messung wird an dem Cooler Synchrotron (COSY) Speicherring mittels eines Radiofrequenz Wien Filters durchgeführt. Dazu beobachtet man einen Aufbau der vertikalen Polarisation des Teilchenstrahls, welcher proportional zu der Größe des EDMs ist. Zusätzlich zu dem EDM beeinflusst auch noch das Magnetische Dipolmoment (MDM), welches um mehrere Größenordnungen größer ist, die Polarisation des Teilchenstrahls. Das MDM kann den Effekt eines EDMs in einem nicht perfekten Beschleuniger nachahmen. Um diesen systematischen Effekt zu eliminieren, vergleicht man Simulationen mit den Messungen. Für die Simulationen des Beschleunigers ist es nötig, die exakten Positionen aller Elemente mit sehr hoher Präzision zu kennen. Dies ist für die Magnete durch mehrere Messkampagnen gegeben, aber für die Strahlpositionsmonitore ist dies nicht der Fall. Die Strahlpositionsmonitore konnten mit den Messkampagnen nicht vermessen werden, sind aber essentiell um die Positionierung des Teilchenstrahls im Beschleuniger zu verstehen. Daher wurde eine Methode entwickelt um auch die Strahlpositionsmonitore präzise zu vermessen. Die Methode, das "beam-based alignment", ermöglicht es, die Strahlpositionsmonitore relativ zu dem magnetischen Zentrum der Quadrupole auszurichten und somit auch zu dem Koordinatensystem aller Magnete. Die Messungen zeigen einen Versatz der Strahlpositionsmonitore von bis zu 5 mm relativ zu ihrer idealen Positionierung. Dieser Versatz wurde korrigiert, sodass die Strahlpositionsmonitore nun ebenfalls ausgerichtet sind. Zusätzlich ist es jetzt besser möglich, den Pfad des Teilchenstrahls zur optimalen Position (Null) zu korrigieren und braucht weniger steuernde Magnete dafür, da man nicht mehr gegen ein Versatz in den Quadrupolen gegensteuern muss.

Acknowledgments

I would like to thank my supervisor Prof. Dr. Jörg Pretz for his advice and input during the time of my thesis and the opportunity to write my thesis at Forschungszentrum Jülich and RWTH Aachen University. The COSY accelerator group around Dr. Ralf Gebel supported me to develop the measurement algorithms and to implement and test them directly at the accelerator. I also would like to thank Markus Retzlaff and his power supply group of COSY for the help with the magnet re-cabling during the first measurement campaign and helping with the selection and connection of mobile power supplies for the second measurement campaign. Thanks to Frank Dahmen for helping with the design of connectors between the magnets and the mobile power supplies. I would like to thank Dr. Alexander Nass for his advice on the technical part surrounding the hardware during the thesis and also for his assistance and help during the measurement campaigns. I especially would like to thank Dr. Volker Hejny, Dr. Alexander Nass, Dr. Frank Rathmann and Dr. Vera Shmakova for their help with moving the mobile power supplies at impossible times in the day and night. Without them it would not have been possible to perform the measurement. Dr. Ilja Bekman was a great help with designing and implementing the BPM gain calibration, when it was noticed that this was required. Additionally, I thank my colleagues from the JEDI collaboration for their help with the measurement campaigns by volunteering for taking shifts and the interesting discussions in all the meetings. Finally I would like to thank my family and friends for all their support during the time of my PhD.

Contents

1	Introduction	1
2	Motivation	3
2.1	Matter Antimatter Asymmetry	3
2.2	C , \mathcal{P} and \mathcal{T} Transformations	4
2.3	Electric Dipole Moment	5
2.4	EDM Searches in Storage Rings	7
3	Beam Dynamics	9
3.1	Coordinate System	9
3.2	Lorentz Force	10
3.3	Transverse Motion	10
3.3.1	Bending Magnets - Dipoles	11
3.3.2	Focusing Magnets - Quadrupoles	11
3.4	Equations of Motion	13
3.5	Dispersion	14
3.6	Orbit Correction	15
4	Cooler Synchrotron (COSY)	17
4.1	General Overview	17
4.2	Quadrupoles	18
4.3	Beam Position Monitors	19
4.4	Orbit Control Software	23
5	Beam Position Monitor Gain Calibration	27
5.1	Beam Position Monitors and the Libera System	27
5.2	Calibration Method	28
5.3	Calibration Software	28
5.3.1	First Version	28
5.3.2	Improved Version	30
6	Beam-based Alignment	35
6.1	General Explanation	35
6.2	Usage of Beam-based Alignment in other Accelerators	36
6.3	Derivation of Formula for Orbit Change	36
6.4	Simulations	38

6.5	Measurement Procedure	40
6.6	Measurements of Quadrupole QT12	41
6.6.1	November 2017 Measurement	41
6.6.2	May 2018 Measurement	46
6.7	Measurement of all Quadrupoles with Back-leg Windings	48
6.7.1	February 2019 measurement	48
6.7.2	Fit	50
6.7.3	Results	50
6.7.4	Improvement of the Orbit	52
6.8	Measurement of all Quadrupoles in COSY	53
6.8.1	New Power Supplies	53
6.8.2	Software for the Power Supplies	54
6.8.3	Measurement Campaign	55
6.8.4	Analysis	56
6.8.5	Results	61
6.8.6	Final Calibration of all BPMs	61
6.8.7	Improvement of the Orbit	62
6.8.8	Crosscheck of the Mechanical Alignment of the Quadrupoles	63
6.9	Further Beam-based Alignment Measurements at COSY	69
7	Outlook: Future EDM Ring Design	71
7.1	BPMs and Alignment in other Accelerators	71
7.2	Prototype and All-electric Ring Design	71
7.2.1	Prototype Ring	72
7.2.2	All-electric Ring	72
7.3	Suggestions for the Ring Design	73
8	Summary and Conclusion	77
A	Appendix A	79
A.1	BPM Calibration	79
A.2	Mechanical Alignment Data of the Quadrupoles	79
	Bibliography	83
	List of Figures	89
	List of Tables	91
	Acronyms	93

CHAPTER 1

Introduction

In research one always searches for solutions for questions and problems one currently faces. One of those questions is quite fundamental: *"Why do we exist?"* It is not understood with current knowledge, why there is more matter than antimatter in our universe. The asymmetry of matter and antimatter could only occur when there are a number of criteria fulfilled, called the Sakharov conditions. One of those conditions is the violation of the CP symmetry. Several sources of this CP violation have already been found and included in the Standard Model of particle physics and cosmology, but there is still not enough CP violating effects in that model. Thus one searches for more sources of CP violation in order to complete the understanding of that question.

One possible source for additional CP violation is a non-vanishing Electric Dipole Moment (EDM) of elementary particles. If this would be found, then one would have a better understanding and could extend the Standard Model to get closer to the answer of that question. There are several searches going on for the EDM of different elementary particles, but so far only upper limits have been established, which are consistent with a vanishing EDM. One of those measurements is being carried out by the Jülich Electric Dipole moment Investigations (JEDI) collaboration, which wants to measure the EDM of protons and deuterons directly. This is done at the Cooler Synchrotron (COSY) storage ring.

In order to perform a precise measurement, one needs to know the accelerator to a precise level. For this reason, alignment campaigns of the accelerator components are being done regularly and are included in simulations for a precise prediction of the measurements. However several crucial elements of the accelerator is not included in these alignment campaigns, which are the Beam Position Monitors (BPMs). These are essential to understand the path of the particle beam through the accelerator, but unfortunately cannot be aligned with the alignment campaigns, as they are missing measurement markers. In order to still be able to include the alignment of the BPMs into the simulations and control system of the accelerator, a dedicated method to align them has been developed and used. This method is the beam-based alignment, where one alignes the BPMs with respect to the magnetic centers of the quadrupole magnets, which are in turn aligned with the alignment campaigns. Thus, after the beam-based alignment measurement, the BPMs are also aligned and can be reliably used for simulations and accelerator operations.

In chapter 2 the motivation for searches for the Electric Dipole Moment (EDM) of elementary particles is given. The following chapters 3 and 4 discuss the behavior of a particle beam inside an accelerator and the Cooler Synchrotron (COSY) accelerator in Jülich. Chapter 5 focuses on

the electrical calibration of the BPMs, which showed to be necessary during the beam-based alignment measurements. The beam-based alignment measurements of the BPMs is discussed in chapter 6, where the partial alignment campaigns and also the full alignment campaign for all BPMs are discussed. An outlook for the future projects to measure the EDM of charged particles by the JEDI collaboration and what one should keep in mind for the calibration of the BPMs is given in chapter 7. Finally, a summary is given in chapter 8.

2.1 Matter Antimatter Asymmetry

Our universe is entirely made out of matter as far as we know. The difference between matter and anti-matter in the universe can be estimated using the baryon asymmetry parameter η as follows:

$$\eta = \frac{N_B - N_{\bar{B}}}{N_\gamma}, \quad (2.1)$$

where N_B is the number of baryons, $N_{\bar{B}}$ is the number of anti-baryons and N_γ is the number of photons. Shortly after the big bang the temperature of the universe was high enough to constantly have pair creation and annihilation in equilibrium. After the temperature dropped below the threshold for pair creation, matter and anti-matter only annihilated and created photons and thus, $2N_\gamma \approx N_B + N_{\bar{B}}$. From the Cosmic Microwave Background, it is possible to deduce a number for η to be approximately 6×10^{-10} [1], whereas the standard model of particle physics and cosmology only accounts for a value of 1×10^{-18} [2]. This discrepancy shows that there has to be more that is not known yet.

There are two solutions that could explain this discrepancy. One would be that, there is an other anti-matter universe, which we do not see. The other one is that, there is a process in the annihilation that leads to leftover matter. For an asymmetric annihilation of matter and anti-matter Sakharov gives three conditions to be fulfilled [3].

1. Violation of the baryon number B , as the initial state of the system was a baryon number of zero, without it one could not end up with leftover baryons.
2. C and CP violation, as without this, each process that creates a particle would have a symmetric process which creates the corresponding antiparticle with equal probability. Thus the baryon asymmetry could have never developed.
3. Interactions out of thermal equilibrium, as in thermal equilibrium the expected value of physical quantities is stable and one could not transition from $B = 0$ to $B \neq 0$.

In the standard model, as mentioned above, there are CP violating processes included. However, the number and strength of those processes is too small to lead to the measured baryon asymmetry. As a result of that, one searches for more CP violating processes beyond the standard model. One of the options is the Electric Dipole Moment (EDM) of elementary particles.

2.2 C , \mathcal{P} and \mathcal{T} Transformations

Symmetries play an important role in physics, as they are linked to conservation laws. More than the currently known sources of violation of the C -, \mathcal{P} - and \mathcal{T} -symmetries lead to physics beyond the standard model. Thus, it is of highest interest to find processes that break those symmetries. The main discrete symmetries in particle physics are the parity transformation (\mathcal{P}), charge conjugation (C) and time reversal (\mathcal{T}) symmetry.

The parity transformation (\mathcal{P}) reverses the sign of all spatial coordinates in a process. If a process is \mathcal{P} -symmetric, then it behaves exactly the same under \mathcal{P} transformation. In 1956 the Wu experiment [4] was performed and showed that there are processes that violate \mathcal{P} -symmetry. In that experiment, the decay ${}^{60}_{27}\text{Co} \rightarrow {}^{60}_{28}\text{Ni} + e^- + \bar{\nu}_e + 2\gamma$ was observed for a polarized cobalt atom. The observation was made that the direction in which electron was emitted favored to be against the direction of the nuclear spin. With the application of the parity transformation the velocity of the electrons would flip the sign, but the polarization direction stays the same. This was the first observation of a parity violating process.

The charge conjugation (C) of a particle is the transformation into its antiparticle, where all additive quantum numbers change the sign. As the charge is an additive quantum number, only non-charged particles can be an eigenstate of the charge conjugation. Examples of that would be the π^0 -meson or the photon. The C -symmetry is however violated in the weak interaction, as left-handed anti-neutrinos do not interact in the weak sector.

The time reversal transformation (\mathcal{T}) of a process is the change of only the direction of the time coordinate. This can be understood as the fact that a reversible process has equal rates in both directions. In the electromagnetic and strong sector measurements do not show a violation of the \mathcal{T} -symmetry, however in the weak sector a violation was observed with the mixing of the $\bar{K}^0 \rightarrow K^0$ and $K^0 \rightarrow \bar{K}^0$ [5].

As all of these transformations are shown to be violated individually, one can combine them to find a symmetry that is not broken. Such a symmetry, the CPT -theorem, was implicitly proposed by Schwinger in 1951 [6], which says that if a local quantum field theory is Lorentz invariant, then the combination of C , \mathcal{P} and \mathcal{T} transformations in arbitrary order is conserved. From that one can then see that a \mathcal{T} symmetry violation directly leads to a $C\mathcal{P}$ symmetry violation in order to conserve the CPT theorem.

The first example of a $C\mathcal{P}$ violating process was found in 1964 by Cronin and Fitch with the measurement of the decay of the K_L^0 kaon [7]. The K_L^0 can decay into two pion and three pion final states, although the decay into a two pion final state would not be allowed if the K_L^0 would be a $C\mathcal{P}$ eigenstate. In order to include that effect into the theory of the standard model, the Cabibbo–Kobayashi–Maskawa (CKM) Matrix [8] was introduced, which describes the mixing of the six quarks, where the complex phase is proportional to the $C\mathcal{P}$ violation.

2.3 Electric Dipole Moment

The CP violating effects included in the standard model are not sufficient to explain the matter antimatter asymmetry, thus more CP violating effects are needed. The Electric Dipole Moment (EDM) of elementary particles is one option for that, as it violates CP symmetry [9]. The classical definition of the EDM is

$$\vec{d}_{\text{classical}} = \int \rho(\vec{r}) d\vec{r}, \quad (2.2)$$

where $\rho(\vec{r})$ is the electric charge density. Here, no CP violation arises so far as it is defined for a macroscopic structure like molecules. In comparison, if one has a look at the EDM at the particle level, then it has to be either parallel or anti-parallel to the spin of the particle, which is the only distinguishable direction as any other direction would give another degree of freedom to the particle. The definition for the EDM on a particle level is

$$\vec{d} = \eta \frac{q}{2mc} \vec{S}, \quad (2.3)$$

where \vec{S} is the spin, q is the charge, m is the mass of the particle and η is a dimensionless quantity giving the magnitude of the EDM. When now investigating the behavior of the EDM under parity transformation (\mathcal{P}) and time reversal transformation (\mathcal{T}), one can see that the Hamiltonian changes under either of the two transformations, which is depicted in figure 2.1. This change of the Hamiltonian would make it a different particle and thus violates that symmetry. In molecules EDMs are possible without violating CP due to the mixing of multiple degenerate ground states with different parity [9].

Particle	EDM / e cm	Reference
e	$< 1.1 \cdot 10^{-29}$ (90% CL)	[10]
μ	$< 1.9 \cdot 10^{-19}$ (95% CL)	[11]
n	$< 1.8 \cdot 10^{-26}$ (90% CL)	[12]
p	$< 2.1 \cdot 10^{-25}$ (95% CL)	[13, 14]

Table 2.1: Measured limits on EDMs for different particles

For measurements of EDMs of elementary particles there are upper limits available up to now (see table 2.1), which are all compatible with zero. The particles of interest for the Jülich Electric Dipole moment Investigations (JEDI) collaboration are the proton and the deuteron, where the upper limit for the proton has been obtained only indirectly and there is no measurement for the deuteron so far. Due to the charged nature of the two particles one has to utilize a storage ring for the measurement of the EDM. The predicted order of magnitude of the EDMs by the standard model is 10^{-32} to 10^{-31} e cm for charged hadrons. This is too small to be measured by the proposed experiment of the JEDI collaboration [15], but extensions of the standard model, such as super symmetry, predict higher values [16, 17], which can exceed 10^{-29} e cm and are expected to be within reach of storage ring experiments.

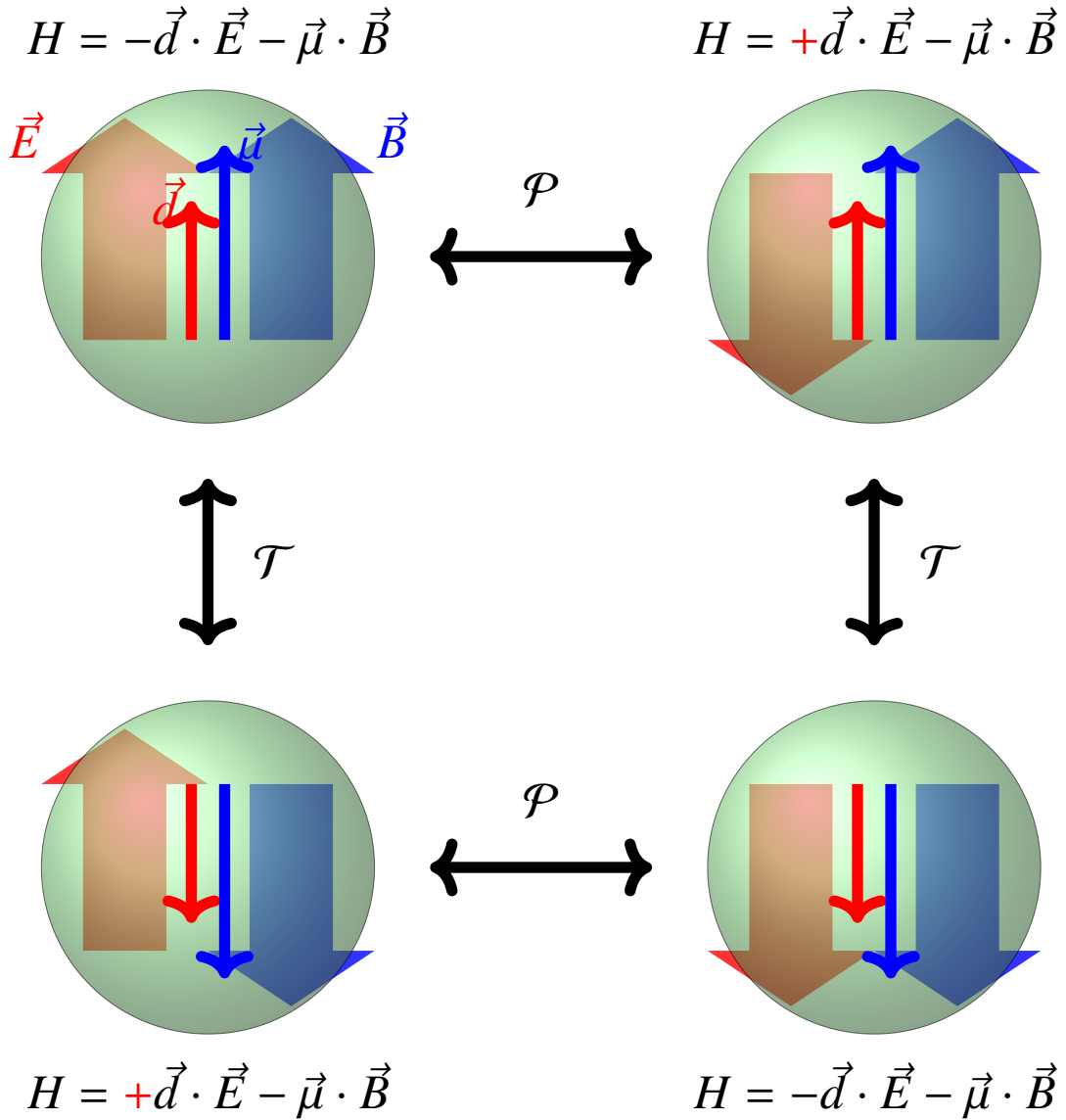


Figure 2.1: Behavior of the EDM (\vec{d}) and MDM ($\vec{\mu}$) under parity transformation (\mathcal{P}) and time reversal (\mathcal{T}). As the EDM and MDM are both aligned with the spin, both of them behave the same under parity transformation (\mathcal{P}) and time reversal (\mathcal{T}). However the fields (\vec{E} and \vec{B}), which they couple to, do not. Under parity transformation (\mathcal{P}) the electric field \vec{E} changes its sign, but the magnetic field \vec{B} and the spin direction, and thus the EDM and MDM, do not. This then leads to a different sign in the Hamiltonian and a violation of the symmetry. The same happens under time reversal (\mathcal{T}), where everything but the electric field changes its sign leading to the same Hamiltonian and also a violation of the symmetry. Combining both parity transformation (\mathcal{P}) and time reversal (\mathcal{T}) leads to every component flipping its sign and thus the initial Hamiltonian is restored.

2.4 EDM Searches in Storage Rings

The basic principle for a storage ring based EDM search is the same as for neutral systems, where the trapping of the particle is in a more confined space [18]. The trap for charged particles is the storage ring itself. The polarized particles are stored and their polarization is observed. Like with the neutral systems an electric field is applied with which the EDM of the particles interacts, which changes the spin direction of the particle and thus the polarization.

The general concept is explained in a little more detail below. A longitudinally polarized particle beam is injected into the storage ring, where it is trapped by the magnetic or electric fields. With a Lorentz transformation into the particles rest frame one can obtain the fields acting on the spin, which are a linear combination of the fields in the lab frame. Due to the interaction of the EDM with the fields, a vertical oscillation of the polarization is induced, which has the frequency

$$\vec{\omega}_{\text{EDM}} = -\frac{q}{mc} \frac{\eta_{\text{EDM}}}{2} (\vec{E} + c\vec{\beta} \times \vec{B}). \quad (2.4)$$

In addition, in the horizontal direction the polarization precesses due to the MDM with a frequency of

$$\vec{\omega}_{\text{MDM}} = -\frac{q}{m} \left[\left(G + \frac{1}{\gamma} \right) \vec{B} + \left(G + \frac{1}{1 + \gamma} \right) \vec{\beta} \times \frac{\vec{E}}{c} \right], \quad (2.5)$$

where it is assumed that the fields \vec{E} and \vec{B} and the velocity $\vec{\beta}$ are all perpendicular to each other. The factor G is the anomalous magnetic moment, which can be related to the g -factor by $G = \frac{g-2}{2}$.

One way to approach the problem is to try to keep the projection of the polarization in the horizontal plane parallel to the momentum by matching the revolution frequency of the particle to the precession induced by the MDM. This would be the "Frozen Spin" condition [19], where one has to match the magnetic and electric field in a certain way. This is possible in different ways for different particles. For particles with a positive G , only electric fields at a certain momentum and no magnetic fields are needed. Whereas for a negative G , both electric and magnetic fields are required. If the "Frozen Spin" condition is achieved then the only term contributing to the spin manipulation is due to the EDM and it would lead to a vertical polarization buildup.

As COSY is a purely magnetic ring, there is no option to use the "Frozen Spin" condition here and the revolution frequency of the particle and the precession frequency of the spin will be different. This will then not lead to a polarization buildup, but instead to a tiny oscillation of the vertical polarization. In order to still measure a polarization buildup a Radio Frequency (RF) Wien filter [20] can be used. The RF Wien filter has an electric and magnetic field which are perpendicular to the beam and oscillate with a set frequency. These electric and magnetic fields are set such that the Lorentz force on the particles vanishes and it does not disturb the beam path or momentum of the particles. Instead it will only have an effect on the spin of the particles. It will give a small kick to the spin of the particles and thus influence the spin precession in the accelerator. The working frequency of the RF Wien filter has to be a harmonic of the spin precession frequency and can be chosen according to equation (2.6).

$$f_{RF} = f_{rev}|k + \gamma \cdot G|, k \in \mathbb{Z} \quad (2.6)$$

Here f_{RF} is the frequency of the RF Wien filter, f_{rev} is the COSY revolution frequency, γ is the Lorentz factor of the particles and G is the anomalous magnetic moment. The most commonly used harmonic for the RF Wien filter at COSY is the $k = -1$ harmonic with a frequency of 871 kHz [21] for deuterons with a momentum of $0.97 \text{ GeV } c^{-1}$. When operating the RF Wien filter on such a harmonic, it will influence the spin such that it has a preferred direction while precessing in the horizontal plane [22]. Because of the preferred spin direction this will then lead to a slow build-up of a vertical polarization, which will depend on the EDM and thus gives a measurable signal.

In addition to the EDM, there are also other effects inducing a slow build-up of vertical polarization. These then have to be understood and included as systematic effects. A major contribution to the systematic effects are due to unwanted magnetic fields. An example for that would be if the beam is not centered inside a quadrupole, which one does not properly take into account in simulations. These can arise from unknown misalignments of magnetic elements. In order to reduce this effect, the magnets in COSY are regularly surveyed and aligned to the COSY coordinate system. The data from these surveys is then also used in the simulations to be closer to reality [23, 24]. The only problem is that the Beam Position Monitors (BPMs) in COSY are not included in that survey, as they lack measurement markers. The proper calibration and alignment of the BPMs is the main topic of this thesis. The calibration of the BPMs is explained in chapter 5 and the beam-based alignment measurements for the BPMs are given in chapter 6.

Beam Dynamics

In order to understand the measurement of the Electric Dipole Moment (EDM) or the beam-based alignment, one needs to know how a particle beam behaves in an accelerator. The particles are influenced by electric and magnetic fields, which keeps them in the accelerator. This evolution of the path of the particles is called beam dynamics. In this chapter, the coordinate system used in accelerators is explained. Then the interaction, via the Lorentz force, of different elements which an accelerator consists of is discussed. The descriptions in this chapter mainly follow [25].

3.1 Coordinate System

The coordinate system used in accelerator physics, the Frenet-Serret or curvilinear coordinate system, is usually split in two parts. The first part of it is used to describe the ideal particle path in the machine. The second coordinate system is a co-moving orthogonal coordinate system $(\vec{e}_x, \vec{e}_y, \vec{e}_z)$, where the deviation from the ideal path is expressed. The full particle coordinates can be expressed with a combination of both coordinate systems.

$$\vec{r}(s) = \vec{r}_0(s) + \delta\vec{r}(s) \quad (3.1)$$

Here the position $\vec{r}_0(s)$ is the position of the ideal particle, described by the global coordinate system and the deviation from that is $\delta\vec{r}(s)$, which is described by the co-moving coordinate system. For beam dynamics, the unit vectors \vec{e}_x and \vec{e}_z span the horizontal plane and \vec{e}_y and \vec{e}_z the vertical plane. A change of the unit vectors is determined by the curvatures (κ_x, κ_y) and connects them in the following way

$$\frac{d\vec{e}_x(s)}{ds} = \kappa_x \vec{e}_z(s) \quad \text{and} \quad \frac{d\vec{e}_y(s)}{ds} = \kappa_y \vec{e}_z(s). \quad (3.2)$$

The curvatures (κ_x, κ_y) are the curvatures in the horizontal and vertical plane respectively. The particle trajectory can now be described by

$$\vec{r}(s) = \vec{r}_0(s) + x(s)\vec{e}_x(s) + y(s)\vec{e}_y(s), \quad (3.3)$$

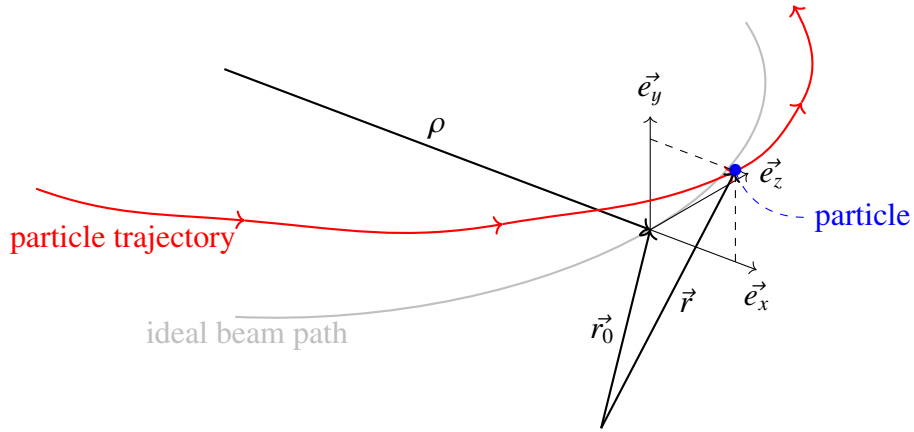


Figure 3.1: Depiction of coordinate system commonly used in accelerator physics. The ideal beam path, which is described by an arbitrary coordinate system \vec{r} is given in light gray. The particle trajectory (red) is given in relation to the ideal path \vec{r} in the co-moving coordinates $(\vec{e}_x, \vec{e}_y, \vec{e}_z)$.

where the coordinates $(x(s), y(s))$ describe the deviation from the ideal beam path. A depiction of the coordinate system can be seen in figure 3.1.

3.2 Lorentz Force

The elements, which an accelerator mainly consists of, have to interact with the beam to keep it in the accelerator. This is governed by the Lorentz force, which is used for bending the particles and focusing them to hold them close to the ideal path in the accelerator. The Lorentz force on a particle with the mass m and a single unit of charge e can be expressed by

$$\vec{F} = e\vec{E} + e[\vec{v} \times \vec{B}]. \quad (3.4)$$

\vec{E} and \vec{B} are the electrical and magnetic field vectors and \vec{v} is the velocity of the particle. In order to keep the beam inside the accelerator typically magnetic fields are used, as it is easier to generate magnetic fields of the order of 1 T compared to electric fields in the order of $3 \times 10^9 \text{ V cm}^{-1}$, which would roughly lead to the same force on a relativistic particle. However, for the acceleration of the particles magnetic fields can not be used, as they only bend the beam and can not change the magnitude of the velocity. Here electric fields are needed for this purpose.

3.3 Transverse Motion

The types of magnets installed in COSY are dipole, quadrupole and sextupole magnets. In each magnet an equilibrium between the Lorentz force and the centrifugal force is used to deflect the particles.

$$m\gamma v^2 \vec{k} + e[\vec{v} \times \vec{B}] = 0 \quad (3.5)$$

Here, $\vec{\kappa} = (\kappa_x, \kappa_y, 0)$ is the local curvature vector of the trajectory, which is the reciprocal of the bending radius

$$\kappa_{x,y} = \frac{1}{\rho_{x,y}}. \quad (3.6)$$

For the further discussion, it is assumed that the magnetic field \vec{B} is perpendicular to the velocity \vec{v} , which means only transverse fields are discussed. Also, the transverse velocity components of a relativistic particle are small compared to the absolute velocity of the particle.

3.3.1 Bending Magnets - Dipoles

For bending magnets only vertical or horizontal fields are used. When a particle with a momentum of $p = \gamma mv$ traverses a bending magnet the bending radius can be expressed by

$$\frac{1}{\rho_{x,y}} = \frac{e}{p} B_{y,x}. \quad (3.7)$$

Out of that one can conclude that a vertical magnetic field leads to a horizontal curvature and vice versa. In order to calculate the angle of deflection the particle obtains by passing a bending magnet, one has to integrate the curvature over the whole magnet

$$\theta = \int \frac{ds}{\rho} = \int B \frac{e}{p} ds = \frac{e}{p} B \cdot \ell. \quad (3.8)$$

Here, ℓ is the length of the magnet. These types of magnets are called dipoles and are used to bend the particles around the circular accelerator. In addition to the main dipoles, also smaller bending magnets are used to steer the beam, if a deviation from the ideal beam path defined by the main dipoles is desired.

3.3.2 Focusing Magnets - Quadrupoles

Next to dipole magnets, another essential magnet type needed to keep the beam inside the accelerator are focusing magnets, the quadrupoles. As the particle beam has an inherent divergence, they are needed to keep the beam together. Like with focusing of light rays, where a light ray is deflected with a lens by an angle to focus it on a focal point (figure 3.2), the same principle is used to focus the beam. The quadrupoles provide a magnetic field, which is proportional to the distance from the center of the magnet and thus will act the same as a lens does for light.

The deflection angle of a focusing magnet can be expressed with

$$\alpha = -\frac{\ell}{\rho} = -\frac{ec}{\beta E} B_\varphi \ell = -\frac{ec}{\beta E} g r \ell, \quad (3.9)$$

where ℓ is the path length of the particle trajectory inside the magnetic field B_φ with the field gradient $g = \frac{dB_\varphi}{dr}$ and E is the energy of the particle. The assumption that the length ℓ is short compared to the focal length and due to that, r does not change, is included in the equation.

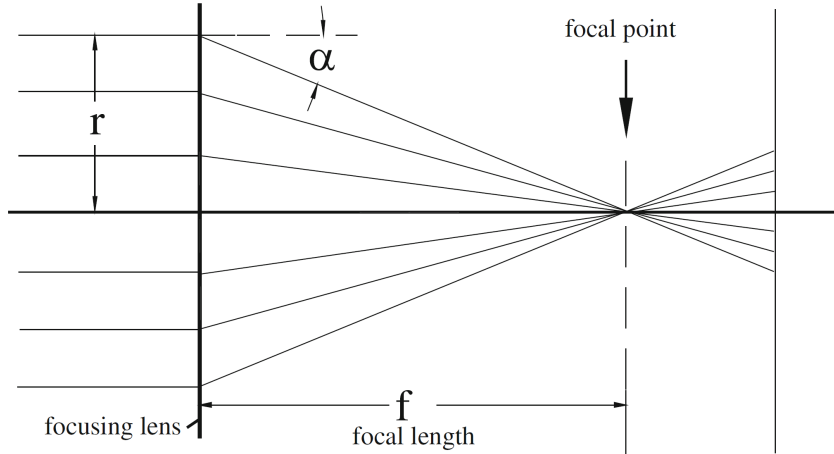


Figure 3.2: Picture illustrating the general principle of focusing, taken from [25].

The above equation is valid for any focusing magnet and will lead to focusing if the magnetic field B_φ or the magnet length ℓ linearly depend on r . With a quadrupole, the magnet length ℓ is constant and the magnetic field linearly depends on r . This is obtained due to the scalar potential of a quadrupole $V = -gxy$ and the derived magnetic fields of

$$-\frac{\partial V}{\partial x} = B_x = gy, \quad (3.10)$$

$$-\frac{\partial V}{\partial y} = B_y = gx. \quad (3.11)$$

A schematic depiction of the field pattern can be seen in Fig. 3.3. These magnetic fields deflect a particle proportional to its distance from the center, like a focusing element. The focusing strength of the quadrupole can be expressed as

$$k = \frac{e}{p}g = \frac{ec}{\beta E}g. \quad (3.12)$$

Which then leads to a focal length of

$$f = \frac{1}{k\ell}. \quad (3.13)$$

This way the quadrupole magnet deflects particles, which are not horizontally centered in the magnet, towards the center and leads to a focusing effect. At the same time any particle, which is not vertically centered will be deflected away from the center of the magnet. Thus a combination of focusing and defocusing magnets is needed to obtain a focusing effect in both planes. This then keeps the particles inside the accelerator, but also makes them oscillate around the ideal path. This oscillation is then called betatron oscillation.

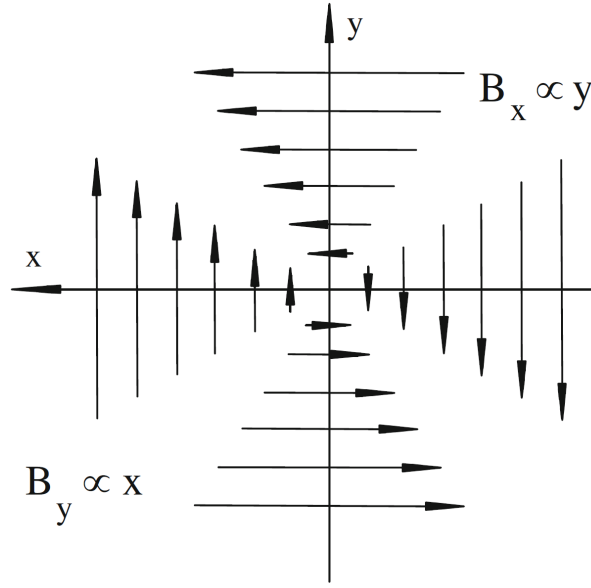


Figure 3.3: Pattern of the magnetic field of a quadrupole, taken from [25].

3.4 Equations of Motion

The betatron oscillations are solutions of the equations of motion for the particles in the accelerator. There are several ways to derive the equations of motion, e.g. via the Lagrangian or Hamiltonian, which are described in detail in [25]. An other way is via the Lorentz force, which will be shortly discussed here.

Dipoles are placed in locations where the beam needs to be deflected and otherwise, there are straight sections in between. Quadrupoles or higher order magnets in general do not influence the ideal path of the beam, but are used to keep the particles together. The coordinate system used is the curvilinear coordinate system, as described in section 3.1. The curvatures, see equation (3.2), are functions of the position along the beam path s and nonzero only inside the magnetic elements. In addition a real particle beam is never exactly monochromatic, thus momentum deviations have to be included.

$$\frac{1}{p} = \frac{1}{p_0(1 + \delta)} \approx \frac{1}{p_0}(1 - \delta + \dots) \quad (3.14)$$

This then also leads to the same change for the curvature.

$$\kappa_x \rightarrow \frac{1}{1 + \delta} \kappa_x = \frac{1}{1 + \delta} (\kappa_{0x} + kx + \frac{1}{2} m x^2 + \dots) \quad (3.15)$$

Here the curvature has been expanded into field components, where κ_{0x} is the curvature due to dipoles, kx due to quadrupoles with focusing strength k , and $\frac{1}{2} m x^2$ due to sextupoles, which have not been discussed. With this, one can calculate the equation of motion for the particles

in the horizontal plane, which is the bending plane, as

$$x'' + (k + \kappa_{0x}^2)x = \kappa_{0x}(\delta - \delta^2) + (k + \kappa_{0x}^2)x\delta - \frac{1}{2}mx^2 - \kappa_{0x}kx^2 + O(3). \quad (3.16)$$

The term $(k + \kappa_{0x}^2)x$ describes the focusing effects from the quadrupoles and also the geometric focusing from the dipoles. The geometric focusing is due to longer path lengths through the magnet for $x > 0$ and shorter path lengths for $x < 0$, which leads to a focusing in the deflecting plane. Particles which do not have the ideal design energy have a varying deflection angle, which is described by the $\kappa_{0x}(\delta - \delta^2)$ term. In addition, the focusing is also energy dependent, which is expressed by the $(k + \kappa_{0x}^2)x\delta$ term and creates chromatic aberrations (chromaticity), which are imaging errors due to energy deviations. These chromatic aberrations (chromaticity) can be corrected with the sextupole $-\frac{1}{2}mx^2$ term. The last term $-\kappa_{0x}kx^2$ only has to be included if there is focusing and bending in the same element.

The same calculation can also be done for the vertical direction, where in most cases κ_{0y} is 0, as the deflection occurs in the horizontal plane. Thus the equation of motion simplifies to

$$y'' - ky = -ky\delta + mxy + O(3). \quad (3.17)$$

The parameters of the magnets κ_0 , k and m are functions of the longitudinal coordinate s . They are constant, non zero, inside the magnets and zero in the drift spaces between the magnets. The design of an accelerator now requires the appropriate distribution of the magnets along the path to obtain the desired beam characteristics.

3.5 Dispersion

One thing one also has to take into account, while designing an accelerator is the dispersion. This is the fact that particles with different momenta have different paths through the dipoles and as such their orbit in the accelerator differs. The presence of dispersion is an intrinsic property of dipole magnets and can not be eliminated. The orbit of a particle is the sum of the desired orbit plus dispersion, thus it is just a different orbit and then subject to the focusing properties of the other accelerator magnets. In order to not have to deal with dispersion all along the ring, one can suppress it in several ways, most of which need placement of extra magnets. One way to suppress dispersion is with extra quadrupoles [26], which can be set to suppress dispersion and simultaneously keep the desired beam characteristics afterwards. This method is relatively flexible and keeps the geometry of the accelerator unchanged, but in general requires the quadrupoles used for suppression to be stronger. An other example would be to the "missing bend" method [27] to suppress dispersion, which would need a modified accelerator geometry and only works with certain magnet settings in the arcs, but needs no additional quadrupoles. There are several more options how to suppress dispersion [26, 28] and in general they are also combined to obtain the advantages of them, while reducing the disadvantages.

3.6 Orbit Correction

As one can not build an accelerator perfectly, there will always be alignment and field errors. This then leads to a distortion of the closed orbit, where the particles do not follow the ideal beam path, but a different one instead. In order to counteract that effect there are a number of correction magnets used in accelerators. These corrector magnets are smaller dipoles compared to the main dipoles, which are used to bend the beam around the accelerator. The corrector magnets are installed for both horizontal and vertical direction, in order to be able to correct for both of the directions. The effect of these corrector magnets can be expressed with the following equation.

$$\Delta u_i = \frac{\sqrt{\beta_i}}{2 \sin \pi Q} \sum_{k=1}^n \theta_k \sqrt{\beta_k} \cos(\phi_i - \phi_k - \pi Q) \quad (3.18)$$

The derivation of this equation will not be explained, but can be looked up in [25]. The change in the orbit Δu measured at the i -th Beam Position Monitor (BPM) is effected by the beta functions (β) and betatron phases (ϕ) at both the position of the BPM and the correctors, which correct with a kick of θ_k . The sum is over the all corrector magnets n . In addition, also the betatron tune Q enters that equation. This equation assumes no coupling and also no dispersion. When one measures an orbit distortion u_i one can calculate the needed corrector kicks θ to correct it. For all m BPMs and n corrector magnets together that can be expressed as a matrix equation.

$$\begin{pmatrix} \Delta u_1 \\ \Delta u_2 \\ \vdots \\ \Delta u_m \end{pmatrix} = \begin{pmatrix} M_{11} & M_{12} & \dots & M_{1n} \\ M_{21} & M_{22} & \dots & M_{2n} \\ \vdots & \vdots & \ddots & \vdots \\ M_{m1} & M_{m1} & \dots & M_{mn} \end{pmatrix} \begin{pmatrix} \theta_1 \\ \theta_2 \\ \vdots \\ \theta_n \end{pmatrix} \quad (3.19)$$

Where each matrix element can be calculated as

$$M_{ik} = \frac{\sqrt{\beta_i} \sqrt{\beta_k}}{2 \sin \pi Q} \cos(\phi_i - \phi_k - \pi Q). \quad (3.20)$$

This matrix \mathbf{M} is called the Orbit Response Matrix (ORM). With that, the orbit can be corrected at the positions of the BPMs by choosing the corrector kicks θ_k such that $\Delta u_m = -u_m$ or by solving

$$\vec{\theta} = -\mathbf{M}^{-1} \vec{u}. \quad (3.21)$$

One can see that it is possible to solve that equation if $n \geq m$, where one can either solve it exactly or not use some of the correctors. In principle, the correction this way is possible, but not always the optimal way to do it, as a perfectly corrected orbit at the BPMs leaves orbit distortions in between them. In order to avoid this, one has to have enough BPMs and correctors distributed along the accelerator. In addition, it is better to correct based on a chi squared minimization procedure, where one minimizes the sum of squares of the orbit distortions at the BPMs, or with the help of a Singular Value Decomposition (SVD), where one can use a cutoff for small singular values, and this way avoids extreme corrector settings, which could occur due to the previous requirement to have a perfect correction. Also, for an optimization procedure it is not required to have more steerers n than BPMs m anymore. The orbit correction

at COSY will be explained in section 4.4.

Cooler Synchrotron (COSY)

The particle accelerator Cooler Synchrotron (COSY) at Forschungszentrum Jülich is operated with protons or deuterons which can be used for internal or external experiments. In the following, an overview of the facility is given and then, a more detailed explanation of the relevant systems used for the performed measurements.

4.1 General Overview

The accelerator complex consists out of multiple parts. First, the ion sources for polarized and unpolarized H^- and D^- ions. These particles are then transferred to the Jülich Isochronous Cyclotron (JULIC) where the particles are first accelerated to kinetic energies of 45 MeV (momentum $p = 295 \text{ MeV } c^{-1}$) or 76 MeV ($p = 540 \text{ MeV } c^{-1}$) for the H^- and D^- respectively [29]. From there on they are transferred through the 94 m injection beam line [30] into the main accelerator COSY. For a sketch of the accelerator complex see figure 4.1. With the injection, they are also stripped of their two electrons at a thin carbon foil and are now protons or deuterons and not the H^- or D^- ions anymore. In the COSY racetrack accelerator with a circumference of 184 m the particles can be accelerated up to a momentum of $3.7 \text{ GeV } c^{-1}$ [31].

The COSY accelerator consists out of two straight sections with a length of 40 m each and two arcs with a length of 52 m each [32]. In each arc there are 12 dipoles each bending by 15° with a maximum field of 1.58 T [33]. Next to the dipoles, there are also 12 quadrupoles in the arcs which allows for a three fold symmetry in each arc. One of the three cells is also mirrored within itself and consists out of a QF-bend-QD-bend and then bend-QD-bend-QF structure [32]. Here QF refers to a focusing quadrupole, QD to a defocusing quadrupole and bend to a bending element, i.e. dipole. The straight sections contain 16 quadrupoles each, which are grouped as four sets (containing 4 quadrupoles each), which allows a tuning of the straight sections to a 1:1 imaging with a π or 2π phase advance.

In the straight sections, multiple devices for beam manipulation are installed. The most important one is the acceleration cavity which is located in the last part of the first straight section after the injection point. In the same straight section there is also an electron cooler with electron energies of 0.025 MeV to 2 MeV, which has been installed in 2013 in COSY [34]. An older electron cooler with electron energies up to 100 keV, which was installed in 1993 in COSY [35], is located in the other straight section and used for the JEDI experiments. The principle of electron cooling is that an electron beam with the same velocity as the proton or deuteron

beam is injected in a short section of the ring and overlapped with the main beam. These electrons scatter elastically with the particles in the beam and reduce the transverse momentum of the particle beam. This then leads to a phase space reduction and smaller beam profiles. In addition, a stochastic cooling system is also available for usage with a beam momentum above $1.5 \text{ GeV } c^{-1}$. Here, the beam is sampled by a pickup detector and the deviation from the optimal orbit is evaluated. This information is then sent to the diagonally opposite side of the ring and a correction is applied by a kicker. This method also allows for a reduction in phase space.

In order to manipulate the spin of the particles during polarized beam operation a RF solenoid, a Siberian Snake, and an RF Wien filter is also installed in the straight sections. In addition, there are two polarimeters installed to resolve the polarization of the beam during the experiment. One is the Wide-Angle Shower Apparatus (WASA) forward polarimeter and the other one is the Jedi Polarimeter (JePo) [36]. Both are able to measure the polarization of the beam and also resolve the spin precession in the horizontal plane. The more recently (2019) installed JePo polarimeter is capable of higher rates than the WASA polarimeter and thus more often used.

The typical amount of particles in the accelerator depends whether those are polarized or unpolarized, as the unpolarized particle source can provide about one order of magnitude higher number of particles. Typical values for the number of particles for an unpolarized beam are in the range of 10^{10} accelerated particles in the accelerator. For the polarized beam that is about an order of magnitude lower in the range of 10^9 accelerated particles.

4.2 Quadrupoles

There are a total of 56 quadrupoles in COSY. 24 of them are in the arcs and the other 32 are in the straight sections. The quadrupoles in the straight sections have a magnetic length of 0.65 m and a maximal gradient of 7.65 T m^{-1} , whereas the ones in the arcs only have a magnetic length of 0.29 m and a maximal gradient of 7.5 T m^{-1} [37]. The quadrupoles in the straight sections are grouped in sets of four quadrupoles to form a quadrupole triplet with four of those sets per straight section. The four quadrupoles form a triplet, as the central two quadrupoles are acting the same way and thus can be interpreted as one element. They are powered by eight main power supplies in total, where the connection to the quadrupoles is done symmetrically for each straight section around the center of the straight section. A depiction of the connections can be seen in figure 4.2. Each set of four quadrupoles is also mounted on one frame for alignment purposes, as they are located closely together. For the arcs the quadrupoles are located in a QF-bend-QD-bend and then bend-QD-bend-QF structure, as already mentioned before. Here the QF and QD quadrupoles are powered by the same power supply for each section. In addition they also share the power supply with the same structure in the other arc. Thus there are six power supplies in total for the arc quadrupoles. An overview picture for that can be seen in figure 4.3. The quadrupoles in the arcs are used for tune changes, where specific main power supplies only shift the horizontal and others the vertical tune, provided there is no coupling.

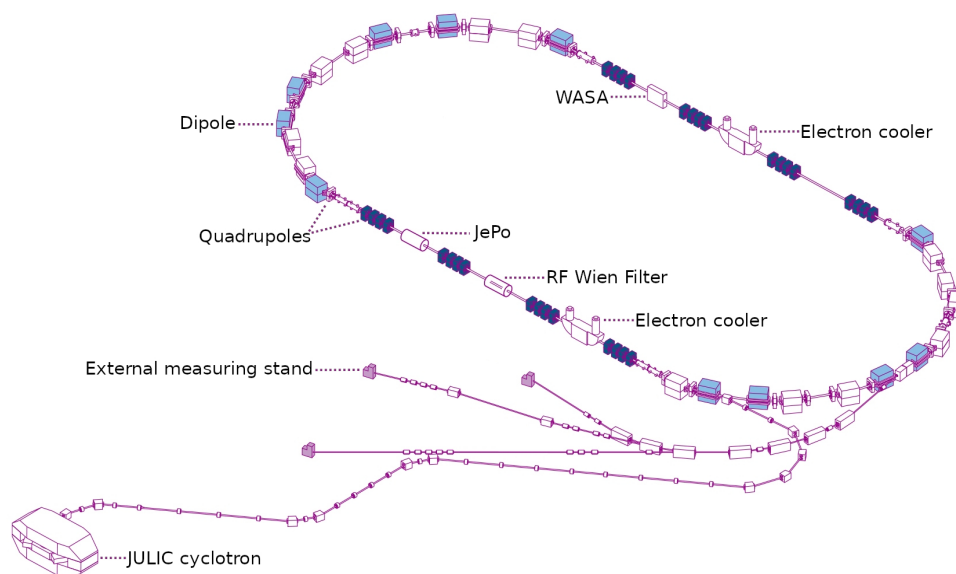


Figure 4.1: Schematic showing the accelerator Cooler Synchrotron (COSY) including the Jülich Isochronous Cyclotron (JULIC), the injection beam-line connecting the two, and three possible extraction beam-lines. In addition the electron coolers, polarimeters (JePo and WASA) and the RF Wien filter is labelled.

4.3 Beam Position Monitors

The majority of the Beam Position Monitors (BPMs) installed in COSY are diagonally cut BPMs which are either a cylindrical shape with a 150 mm diameter or a rectangular shape with dimensions of 150 mm \times 60 mm [38]. An example how a diagonally cut cylindrical BPM looks like is shown in figure 4.4. The two different shapes of the BPMs are needed, as the beam pipe is round in the straight sections and rectangular in the arcs to fit into the dipole magnets. In addition to those BPMs, there are also two special geometry BPMs within the beam pipe of the 2 MeV electron cooler [39] and two thin rogowski coil BPMs [40, 41] close to the RF Wien filter. The BPMs in the electron cooler and close to the RF Wien filter each use a special readout system, which is different from the others.

All the other BPMs are read out by the same system of electronics, which has been upgraded in 2016 [43]. The Libera Hadron system [44] is used in combination with pre-amplifiers to read the signal induced by the beam and to evaluate the position. Each BPM has 4 plates which pick up the position signal based on the principle of charge division between two opposite plates. In figure 4.5, one can see a block diagram of the electronics of one BPM. The figure shows the pickup plates of the BPM connected to two amplifiers, where the first one has a fixed gain of 20 dB and the second one has a variable gain from 0 dB to 50 dB. Then the signal is digitized

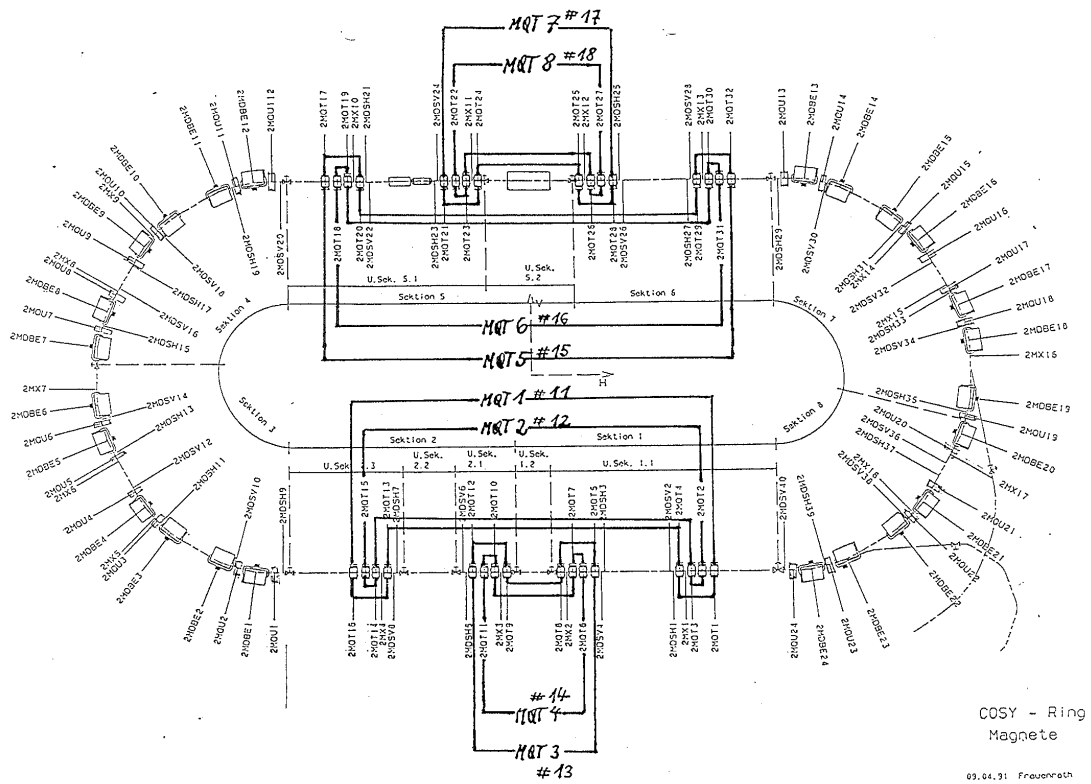


Figure 4.2: Scan of the original document depicting the connection of the main power supplies of the quadrupoles to the individual quadrupoles in the straight sections. The slightly thicker black lines indicate the connections of the quadrupoles and their corresponding main power supply. In total there are eight main power supplies, each powering four quadrupoles.

in the Libera Hadron system and the position is evaluated with the following formulas:

$$X = K_x \left(\frac{V_L - V_R}{V_L + V_R} \right) + X_{\text{offset}}$$

$$Y = K_y \left(\frac{V_U - V_D}{V_U + V_D} \right) + Y_{\text{offset}}$$

Where V_L, V_R, V_U, V_D are the values of the input signals after amplification and digitization, K_x and K_y are geometry factors related to the sensitivity of the sensors and X_{offset} and Y_{offset} are offsets one can apply in the software in case the BPM is not perfectly on axis.

As it is possible that not all signal paths through the amplifiers are exactly equal, there is also a calibration circuitry shown in figure 4.5. One can inject a test pulse into the BPM readout system, which is generated by a signal generator and then split to all four pickup plates of the BPM. This way one can ensure that all amplifying branches of the BPM behave the same and that there is no wrong calibration due to different gains of the amplifiers in each branch. For this calibration, an automated system has been developed to set the gains of the variable amplifiers, which is described in more detail in chapter 5.

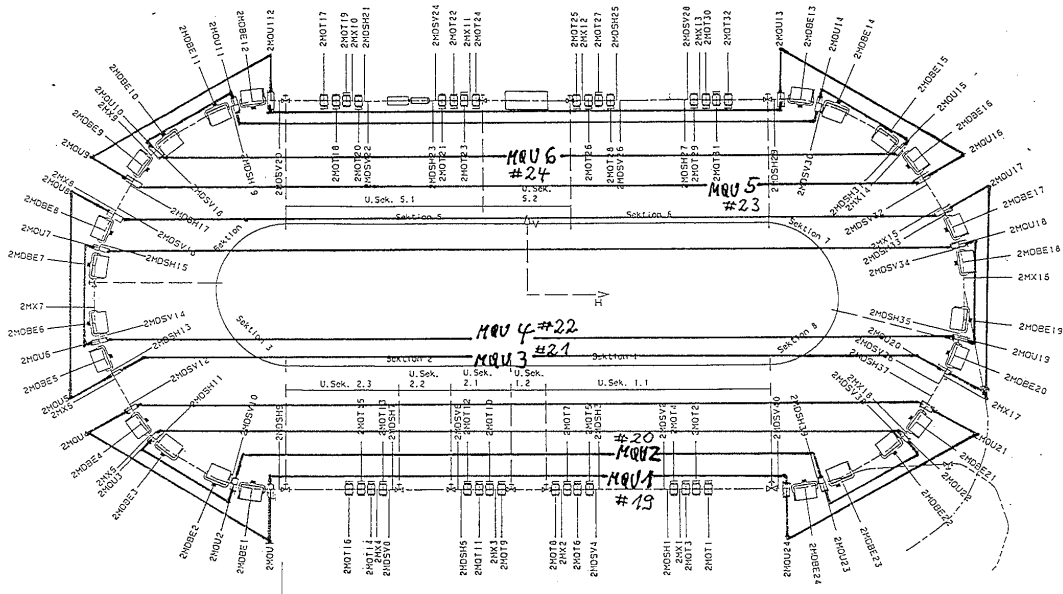


Figure 4.3: Scan of the original document depicting the connection of the main power supplies of the quadrupoles to the individual quadrupoles in the arcs. The slightly thicker black lines indicate the connections of the quadrupoles and their corresponding main power supply. In total there are six main power supplies, each powering four quadrupoles.

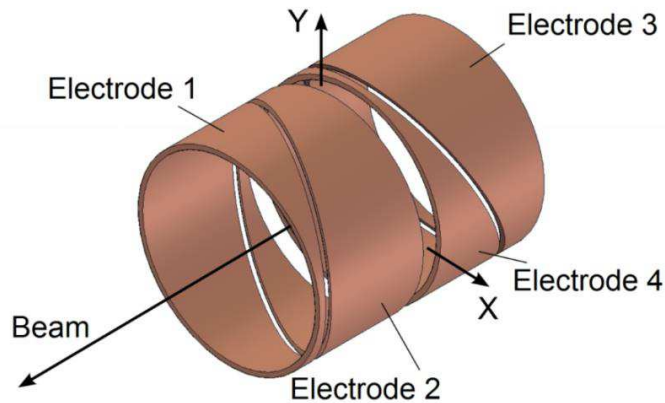


Figure 4.4: Illustration of a diagonally cut cylindrical BPM, where the cylindrical pipe surrounding the beam is cut diagonally to separate it into two electrodes for position detection for each direction. With the voltage ratio of electrodes 1 and 2, typically called right and left, one can determine the horizontal (x) position of the beam. Electrodes 3 and 4, typically called up and down, work the same way for the vertical (y) direction. Picture taken from [42].

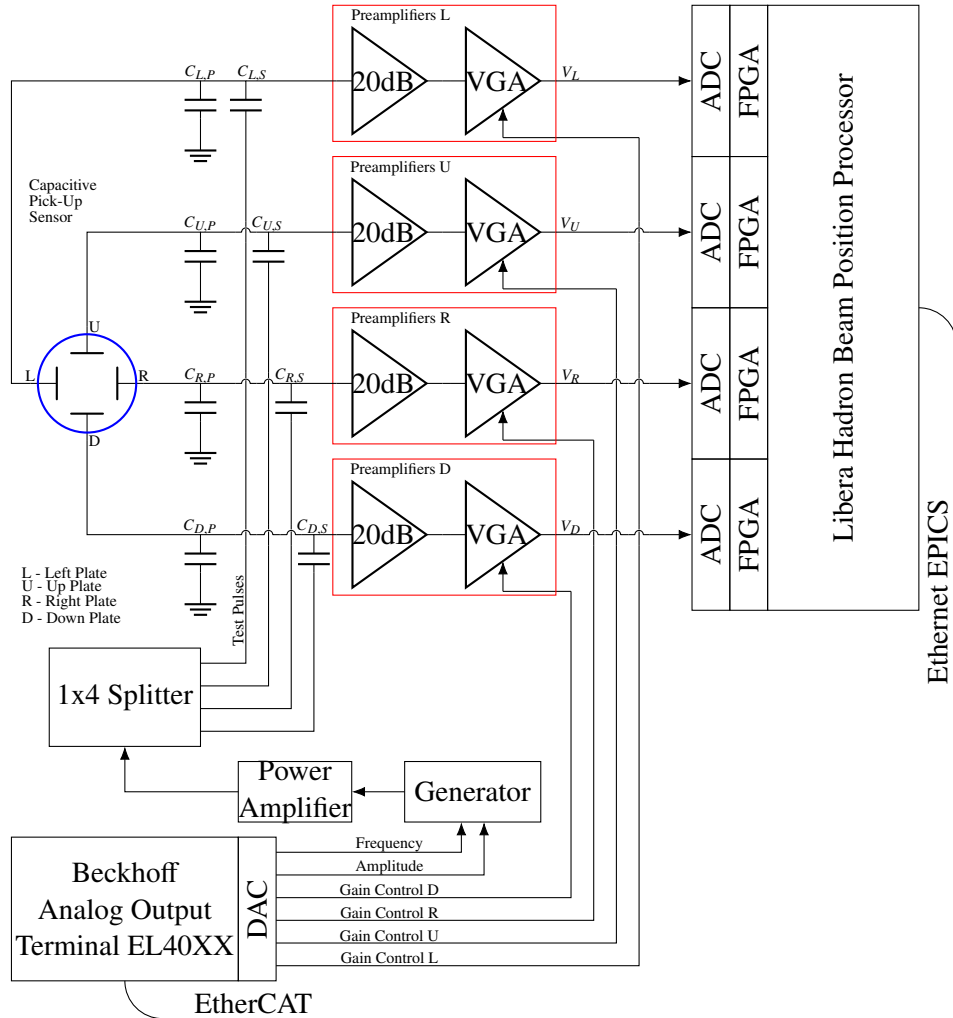


Figure 4.5: Block diagram showing the electronics for one BPM. The pickup plates are shown surrounded by the circular beam pipe on the left side of the diagram. From there the signal from each pickup passes through two amplifying stages. The first one is a fixed amplification of 20 dB and the second one in a Variable Gain Amplifier (VGA) with a gain from 0 dB to 50 dB. Then the signals are digitized by the Libera Hadron System and the beam position is evaluated. For the control system, the position is then provided via an Ethernet connection. In addition, the calibration electronics are also shown at the bottom of the block diagram. It is possible to inject an artificial signal before the amplification stage of the BPM in order to make sure that each amplification stage behaves the same. For this, a signal can be generated and then distributed to each pickup. The output can be observed and the gains adjusted accordingly, such that all amplification stages behave the same.

4.4 Orbit Control Software

The orbit control software is used to correct the orbit in the accelerator to a predefined orbit. In order to do that, it uses the measured orbit in the machine and calculates the changes needed to be done to the correcting magnets, also called steerers, in order to get to the desired orbit with the use of the Orbit Response Matrix (ORM) (see equation (3.19)). The Orbit Response Matrix contains entries for all steerer and BPM combinations and how a change of one steerer has an effect on a BPM, which can be used to determine the optimal steerer setting to get as close to the desired orbit as possible. There are two options to get an Orbit Response Matrix to use it for the orbit correction. The more simple way is to calculate an Orbit Response Matrix from the model of the accelerator. This then gives quite good results already, but a measured Orbit Response Matrix gives a better optimization, as it reflects the current machine state. In the earlier times of usage of the orbit control software, the Orbit Response Matrix was calculated from the model, as no fast automated procedure to measure an Orbit Response Matrix was available. Nowadays, such an automated measurement procedure for the Orbit Response Matrix exists and mostly a measured Orbit Response Matrix is used for the orbit optimization. After determining the optimal steerer settings for the desired orbit with the help of the Orbit Response Matrix, one can apply them to the machine. The optimal steerer settings are determined by using Singular Value Decomposition (SVD) to invert the Orbit Response Matrix. While doing so, the small singular values are dropped. The cut-off threshold can be chosen by the user, but is mostly left fixed. Then the desired orbit change is multiplied with the inverted Orbit Response Matrix to calculate the needed steerer changes. Large steps in steerer settings can lead to beam loss, which is why only a fraction of the calculated change is applied in one step. Then a next step is calculated and applied again. This repeats until one is as close as possible to the desired orbit.

The orbit control software can be used in several ways. It can only measure the orbit and not calculate and apply any corrections to the orbit. This way it can be utilized as a visualization tool for the orbit. It can selectively correct in one plane (horizontal or vertical), both at the same time, or use a coupled correction. The user can set the fraction of the correction that should be applied in one step and also define the time in between the individual steps. The default operation is that the time frame is 2 s and the applied fraction of the correction is 5 - 20%. With higher percentages there is the risk of beam loss and for shorter time periods the communication to the steerers might not be fast enough to actually apply the changes and have a new orbit measurement using the new settings available.

The interface of the orbit control software can be seen in figure 4.6. One can see the display of the orbit measurement on the top, where one can show several different curves. Options for that are the currently measured orbit, a saved reference, the desired golden orbit, or the difference between the measured orbit and the saved reference. All of these different orbits can be shown for both horizontal and vertical direction. The x-axis goes along the accelerator and the y-axes show the BPM measurements, where the axis for the vertical orbit is on the left side and the axis for the horizontal orbit is on the right side to make it possible to scale them independently. Below the display of the orbit in the accelerator one can see the power of the steerers, where one can then easily see which steerers are modified by the orbit correction and their corresponding strengths. Below that there is some statistical information and several

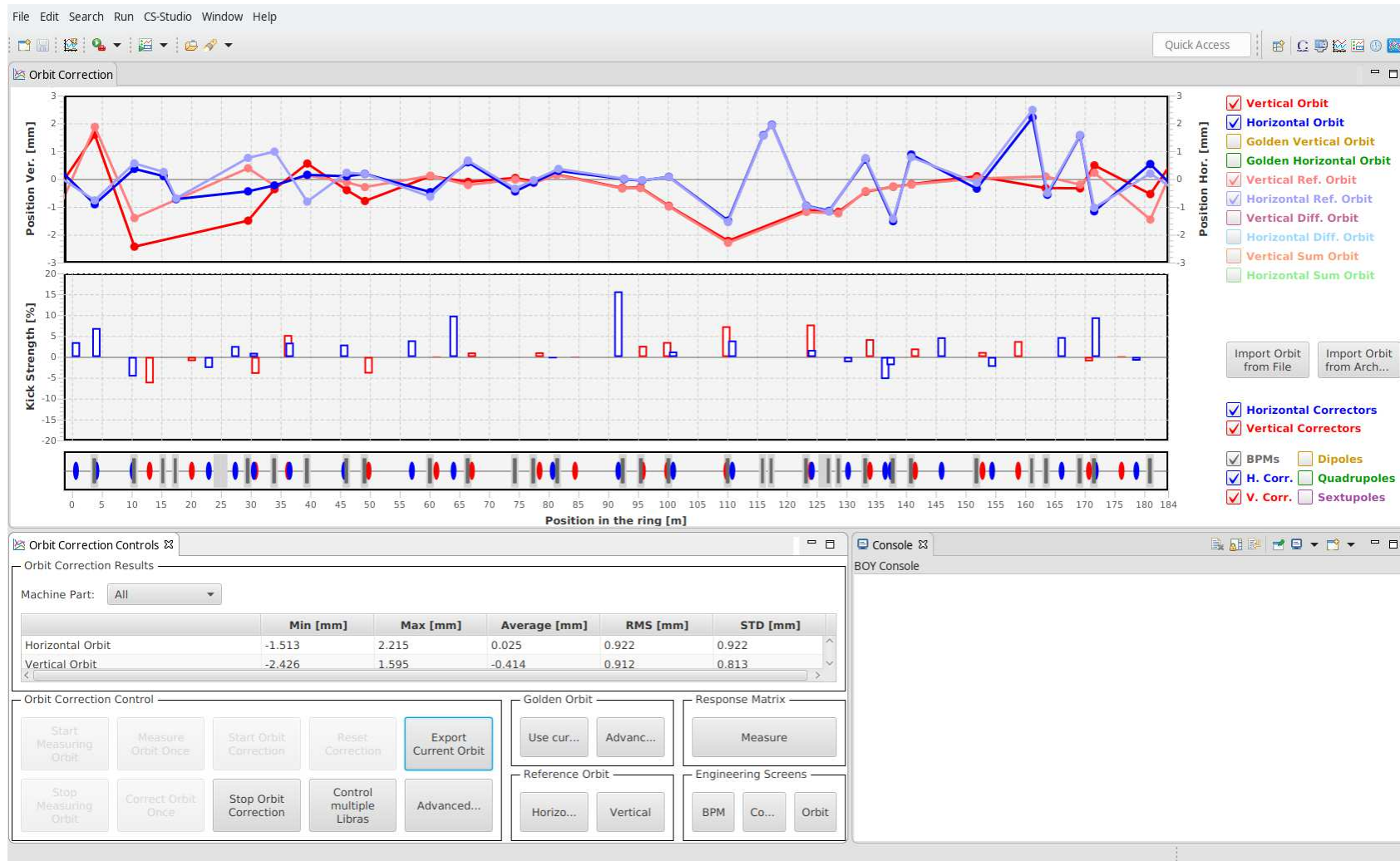


Figure 4.6: The picture shows the interface of the orbit correction software. It is a dedicated perspective in the Control System Studio (CSS) program [45]. The top graph shows the measured orbit in the accelerator, where one can also show various different other comparisons, by enabling them with the check-boxes on the side. The bar graph below that shows the steerer strengths of the currently in use steerers, which the orbit correction software can control. In the table below that several values which can be used to judge the orbit quality can be seen. At the bottom there are the buttons used to control the orbit correction software and switch between the different modes, where some of the buttons have been disabled as in the screenshot the orbit correction is currently running.

buttons, which are mostly self explaining according to their label.

In the settings of the orbit correction, which can be seen in figure 4.7, one can select the BPMs and steerers to be used for the orbit correction. By disabling certain BPMs or steerers one can optimize the orbit correction if some BPMs are misbehaving or fix the values for some steerers which should not be changed during the orbit optimization. An example where that is needed is when using the electron cooler, as one has to set the surrounding steerers up to compensate for the electron cooler fields, which should not be compromised by the orbit correction. Below that one can set the parameters of the orbit correction, which were already mentioned above. One is the correction period and the others being the correction strength of the horizontal and vertical plane. These correction strengths can be set independently if the correction of the orbit is separate for both planes. In the case of a coupled correction this is not the case, as both are corrected at the same time with the same correction percentage.

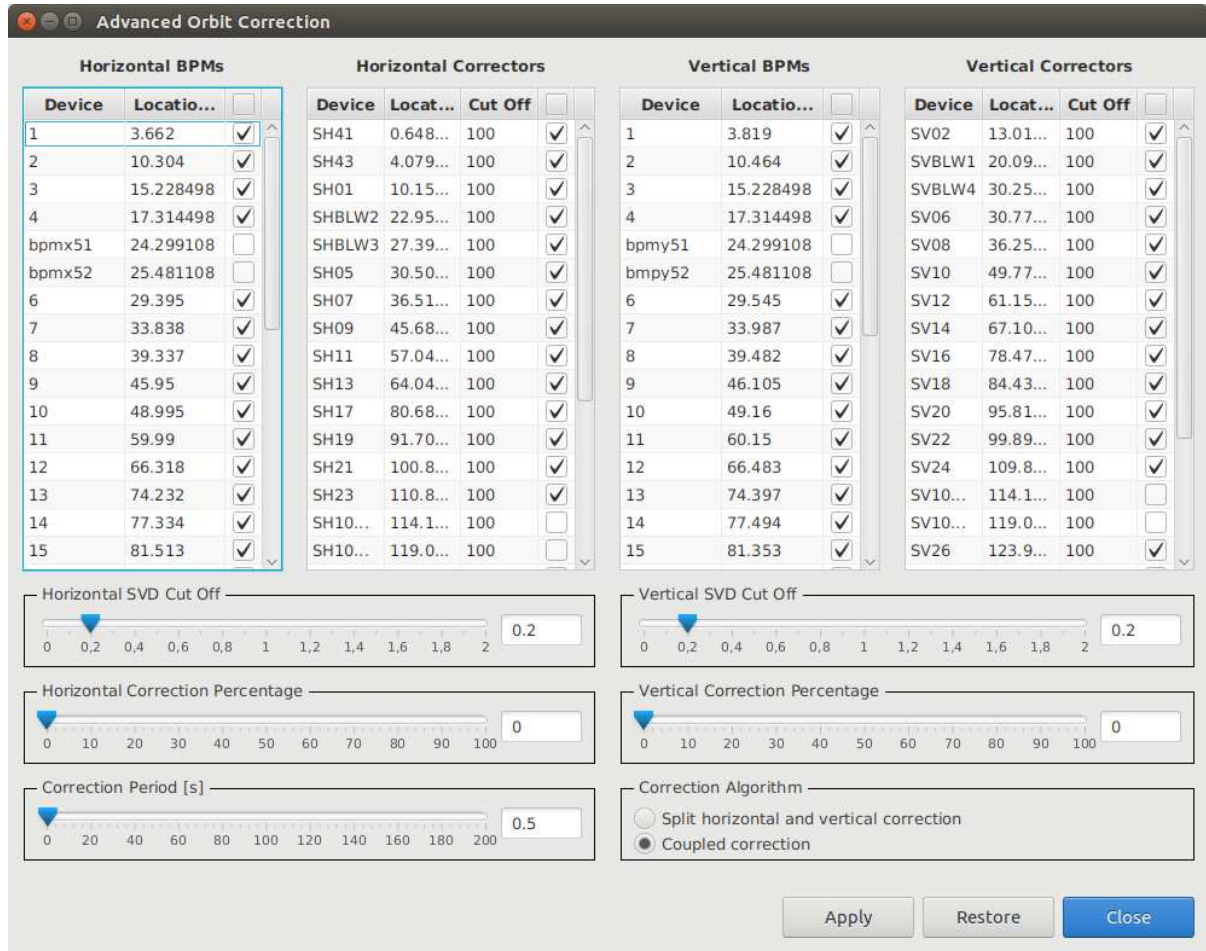


Figure 4.7: Settings window of the orbit correction. The lists show the BPMs and steerers for horizontal and vertical direction, where one can select whether to use them for the orbit correction or not. Below them the settings for the correction can be set. The "SVD Cut Off" sliders can be adjusted to change the settings for the Singular Value Decomposition used for the correction algorithm, but are usually left at default. The "Correction Percentage" slider is used to set the fraction of the calculated change which should be applied in one step and "Correction Period" sets the time interval between corrections. In addition it can be chosen whether a coupled correction or a correction in both planes separated is wanted by choosing the appropriate correction algorithm.

Beam Position Monitor Gain Calibration

In order to get the correct orbit position out of the Beam Position Monitors (BPMs), they have to be properly calibrated. The signals coming from the pickups go through several amplification stages and if those are not equal, the result will not reflect the actual position. The most simple assumption is that if one sets all amplifiers of the pickups, that are needed for the position calculation, to the same gain, then one should be quite close. This is however not the optimal case. In reality, all the amplifiers differ a little bit and thus these small differences have to be taken into account. In order to understand how the calibration is done, at first the readout system will be explained and then the calibration itself.

5.1 Beam Position Monitors and the Libera System

In COSY there are 30 pickups with 4 plates each used for the determination of the beam position. The basic principle of the measurement is charge division between two opposing plates. Each of the plates is connected to two amplifiers, where the first one has a fixed gain of 20 dB and the second one is adjustable between 0 dB and 50 dB. After the amplifiers the signal is fed into the “Libera Hadron Beam Position Processor” unit. There the signal is digitized with 16 bit ADCs and with that the position is calculated by the following formulas [44]:

$$X = K_x \left(\frac{V_L - V_R}{V_L + V_R} \right) + X_{\text{offset}} \quad (5.1)$$

$$Y = K_y \left(\frac{V_U - V_D}{V_U + V_D} \right) + Y_{\text{offset}} \quad (5.2)$$

Here V_L , V_R , V_U and V_D are the values of the input values after amplification and digitization. K_x and K_y are geometry factors related to the sensitivity of the BPM and X_{offset} and Y_{offset} are offsets one can apply in case the BPM is not perfectly centered.

These expressions are valid when the signal transfer from all the pickups is the same, else these expressions do not produce the correct result. In general, the signal transfer is always a little different, as the gain of all the amplifiers is not exactly the same and it is also temperature dependent. That is why additional calibration is needed. There is an additional connection to the signal transfer line in front of the amplifiers, where one can give a calibration signal from a frequency generator to mimic the beam. This signal is split equally on all the amplifier chains.

For a sketch of the connections between the BPM pickups, amplifiers and calibration signal see figure 4.5 in the previous chapter. When the system was set up it was made sure that there is no difference between the individual lines to the pick up plates. With that procedure one can apply the same signal to all plates of the BPM and thereby get a zero reading (or the set offset X_{offset} or Y_{offset}) from the system. If the result is not zero the signal transfer is not the same and it can be corrected for.

5.2 Calibration Method

The method of the electronic calibration of BPMs is relatively simple. In order to calibrate the BPMs one feeds the same signal to both pickups used for the position calculation and then one adjusts the gain of the amplifiers in such a way that the position is zero¹. The only problem with this method is that the signal has to correspond to the signal a beam in the accelerator would induce. Therefore, there are multiple frequency generators installed for the BPMs. These frequency generators generate a signal with the same frequency as the accelerator revolution frequency and thus mimic the signal of the beam. In addition, one can set the amplitude of the signal in order to mimic different beam currents in the machine. One frequency generator is used for multiple BPMs by fanning out the signal. This way it is made sure that the same signal is applied to the pickups.

With this system, one can calibrate the BPMs manually by checking the beam position and adjusting the gain of the correct amplifier. The user interface, where the frequency generators and amplifiers can be adjusted is shown in figure 5.1. This, of course, takes quite some time and can not be done during a measurement period of the machine. Therefore, it is done once and the drifts of the amplifiers with temperature or other external conditions are assumed to be small, although they are not necessarily small. In order to improve this, an automatic procedure has been developed to do this much faster. The faster automatic calibration can then also be applied during a measurement period in order to correct for drifts of the amplifiers.

This automatic procedure basically performs the same task as the manual procedure but faster. It checks whether the position read is not zero and adjusts the gains of the amplifiers accordingly. The details are explained in the next section.

5.3 Calibration Software

5.3.1 First Version

As the whole control system of COSY uses the Control System Studio (CSS) environment, the calibration should also be included there. With the CSS framework it is possible to access Process Variable (PV) quite easily. In addition, the Graphical User Interface (GUI) design is also straight forward. Thus the calibration software was designed inside that framework. The source code is referenced in [46]. The Graphical User Interface can be seen in figure 5.2. There one sees two parts of the calibration GUI. The upper part is where the settings are made and

¹ If an offset is applied to the BPM, then one has to correct such that one obtains the offset instead of zero.



Figure 5.1: Interface used to adjust the gain of the BPMs and set the frequency generators. Either one can set the setting for each BPM individually or apply a global setting to all the BPMs. The individual setting can be set in the row for each BPM. The global setting can be set to all selected BPMs (with the check-boxes at the beginning of the rows) by entering a value at the very bottom of the interface. The common gain is used to amplify the signal to an appropriate level, where the setting depends on the beam current. The gains for the four directions have to be adjusted such that all four branches behave the same. These are the gains to be changed by the gain calibration. On the right side the settings for the frequency generators are shown. There are eight frequency generators available, where their assignment is shown with the sectioning by the horizontal lines. The first two BPMs are served by the same frequency generator as the last two BPMs. The setting for the frequency generator at the very bottom is a global setting for all of them. In this figure one can see one example for the gains for calibrated BPMs. The common gain is chosen by the user to get a good signal and then for the calibration, one does small adjustments for the individual directions.

the calibration is started. The lower part, where all the BPMs and their gains and read positions are listed, is used for debugging purposes and a possible crosscheck. The main work upon pressing the “Calibrate” button is done by an external python script.

The script processes all the required tasks to calibrate the BPMs. It turns on the frequency generators as needed and checks if the BPM is already sufficiently calibrated. The threshold under which the BPM is considered calibrated can be set by the user. In case the BPM is not calibrated it adjusts the gain of the BPM iteratively. The step size of the gain can also be set by the user. When adjusting the gain, the script makes sure that the average gain stays constant in order to prevent the gain from running away and the signals would get amplified too much. It also checks if it reaches the maximal or minimal threshold of the gain in order to prevent impossible settings for the amplifiers. If in an iteration step the gain of a BPM is changed it will be remembered. This way it is possible to check if the new setting was already chosen that would have lead to an infinite recursion. If this is the case, the user is told which BPM could not be calibrated. Also, if a maximal number of iterations is done the script will also stop and inform the user about non calibrated BPMs. This way, the user can adjust the configuration parameters in order to restart the calibration with either a lower gain step size or a higher threshold for the position to be considered zero. If all BPMs are calibrated, the script only reads the positions with activated frequency generators and then finishes. This is very fast and thus can also be done during a measurement period. In case only a few BPMs are not properly calibrated it only performs the calibration for them. In figure 5.3 one can also see a flowchart depicting the workflow of the software. This way of implementation unfortunately has some downsides. The first thing that can be improved is to parallelize the calibration of all BPMs, as in the current implementation of the script it reads them sequentially. Another issue is the way the calibration is called from the CSS interface. When a python script is called from CSS it will freeze CSS until the python script is done. This does not only affect the single window where the script is called from, but the whole CSS instance. Thus, even with an execution time of a few seconds, it is not particularly user friendly. An other improvement is to not only use single steps given by the user, but use a predictive search algorithm to be able to predict the optimal gain setting and start the iterative search closer to the optimum. All these changes required major changes to the python script, which was used for the calibration procedure. Instead of changing the python script it was decided to move the computation out of CSS into a standalone Epics Input / Output Controller (IOC) and only have the graphical interface remain in CSS. This way the execution does not freeze the CSS instance and the user can use the software and look at the progress of the gain calibration in real-time.

5.3.2 Improved Version

These improvements were then implemented into an IOC [47], where the parallelization was easier to implement right from the start. This version of the calibration software is based on the first version developed by myself, which was shown and explained in the previous section. The basic principle of operation stays the same, while improving on the performance. As a first step of the performance improvement, all computation is parallelized. In addition, before using an iterative search procedure a predictive computation is done. The first two measurement points for the gains are further apart (± 1 dB) and then a linear interpolation predicts where the

The screenshot shows the 'Gain Calibration' window. At the top left, there are input fields for 'Threshold' (0.1) and 'Gain step' (0.25), and a 'Calibrate' button. Below these is a checkbox labeled 'Show all values' which is checked. The main area contains two tables. The first table lists BPMs with their gain settings and measured positions. The second table lists Frequency Generators with their frequency, amplitude, and status.

BPM	Common Gain	Left	Up	Right	Down	Position X	Position Y
1	10.00 dB	0.00 dB	0.00 dB	0.04 dB	0.07 dB	17.302105 mm	-7.186958 mm
2	10.00 dB	0.07 dB	0.27 dB	0.00 dB	0.00 dB	15.739575 mm	-5.823766 mm
6	10.00 dB	0.20 dB	0.16 dB	0.00 dB	0.00 dB	-3.107360 mm	1.754482 mm
7	10.00 dB	0.00 dB	0.31 dB	1.04 dB	0.00 dB	7.811839 mm	-3.187512 mm
8	10.00 dB	0.00 dB	0.03 dB	0.01 dB	0.00 dB	23.021304 mm	-6.892785 mm
9	10.00 dB	0.00 dB	0.00 dB	0.35 dB	0.06 dB	16.978901 mm	-7.477725 mm
10	10.00 dB	0.00 dB	0.00 dB	0.06 dB	0.19 dB	21.321882 mm	-4.228368 mm
11	10.00 dB	0.00 dB	0.11 dB	0.10 dB	0.00 dB	12.142235 mm	2.177173 mm
12	10.00 dB	0.00 dB	0.00 dB	0.36 dB	0.03 dB	16.394705 mm	2.871536 mm
13	10.00 dB	0.29 dB	0.00 dB	0.00 dB	0.08 dB	20.678373 mm	4.480351 mm
14	10.00 dB	0.00 dB	0.59 dB	0.18 dB	0.00 dB	15.913045 mm	6.242171 mm
15	10.00 dB	0.00 dB	0.09 dB	0.00 dB	0.00 dB	17.313201 mm	5.992084 mm
16	10.00 dB	0.01 dB	0.11 dB	0.00 dB	0.00 dB	18.292261 mm	-0.460307 mm
17	10.00 dB	0.05 dB	0.00 dB	0.00 dB	0.11 dB	13.642566 mm	-1.868075 mm
18	10.00 dB	0.05 dB	0.25 dB	0.00 dB	0.00 dB	17.200025 mm	-2.490239 mm
19	10.00 dB	0.00 dB	0.24 dB	0.73 dB	0.00 dB	-11.243551 mm	-0.185746 mm
ecolgun	15.00 dB	0.90 dB	0.00 dB	0.00 dB	0.45 dB	-9.647478 mm	-1.016443 mm
ecolcol	15.00 dB	0.13 dB	0.16 dB	0.00 dB	0.00 dB	-10.873920 mm	-0.809781 mm
20	10.00 dB	0.41 dB	0.00 dB	0.00 dB	0.14 dB	-18.714880 mm	0.781387 mm
anke2	10.00 dB	0.00 dB	0.32 dB	0.10 dB	0.00 dB	-5.603156 mm	-0.728424 mm
21	10.00 dB	0.00 dB	0.01 dB	0.19 dB	0.00 dB	6.722239 mm	-0.854487 mm
22	10.00 dB	0.00 dB	0.24 dB	0.23 dB	0.00 dB	6.959612 mm	-0.813000 mm
23	10.00 dB	0.19 dB	0.00 dB	0.00 dB	0.43 dB	12.027931 mm	-0.088929 mm
24	10.00 dB	0.00 dB	0.00 dB	0.12 dB	0.21 dB	13.613575 mm	4.392247 mm
25	10.00 dB	0.64 dB	0.00 dB	0.00 dB	0.00 dB	27.553686 mm	-0.195262 mm
26	10.00 dB	0.06 dB	0.05 dB	0.00 dB	0.00 dB	22.542366 mm	1.509122 mm
27	10.00 dB	0.00 dB	0.00 dB	0.13 dB	0.07 dB	18.415321 mm	-0.447803 mm
28	10.00 dB	0.22 dB	0.13 dB	0.00 dB	0.00 dB	17.706343 mm	0.788435 mm
29	10.00 dB	0.00 dB	0.00 dB	0.12 dB	0.43 dB	24.689328 mm	-9.241250 mm

Freq. Gen.	Frequency	Amplitude	On / Off	Remote
6	1500.0 kHz	1000.00 mV	OFF	REMOTE
10	1500.0 kHz	1000.00 mV	OFF	REMOTE
12	1500.0 kHz	1000.00 mV	OFF	REMOTE
16	1500.0 kHz	1000.00 mV	OFF	REMOTE
ecolgun	1500.0 kHz	1000.00 mV	OFF	REMOTE
21	1500.0 kHz	1000.00 mV	OFF	REMOTE
24	1500.0 kHz	1000.00 mV	OFF	REMOTE
28	1500.0 kHz	1000.00 mV	OFF	REMOTE

Figure 5.2: Screen capture of the first version of the gain calibration GUI. The smaller part in the top left of the window is always shown, whereas the details about all the BPMs and their gains, etc. are only shown if "Show all values" is checked. In the two text fields one can enter the threshold under which the BPMs should be considered calibrated in mm and the step size of the gains in dB. The software then performs the search with those settings if the "Calibrate" button is pressed. The detailed information, which makes up most of the window is hidden by default. There one can see the gain settings and measured positions of all BPMs and the Frequency generators settings. Note that the picture was taken during a maintenance, where there was no beam or calibration signal, thus the BPM positions just show an arbitrary last recorded value.

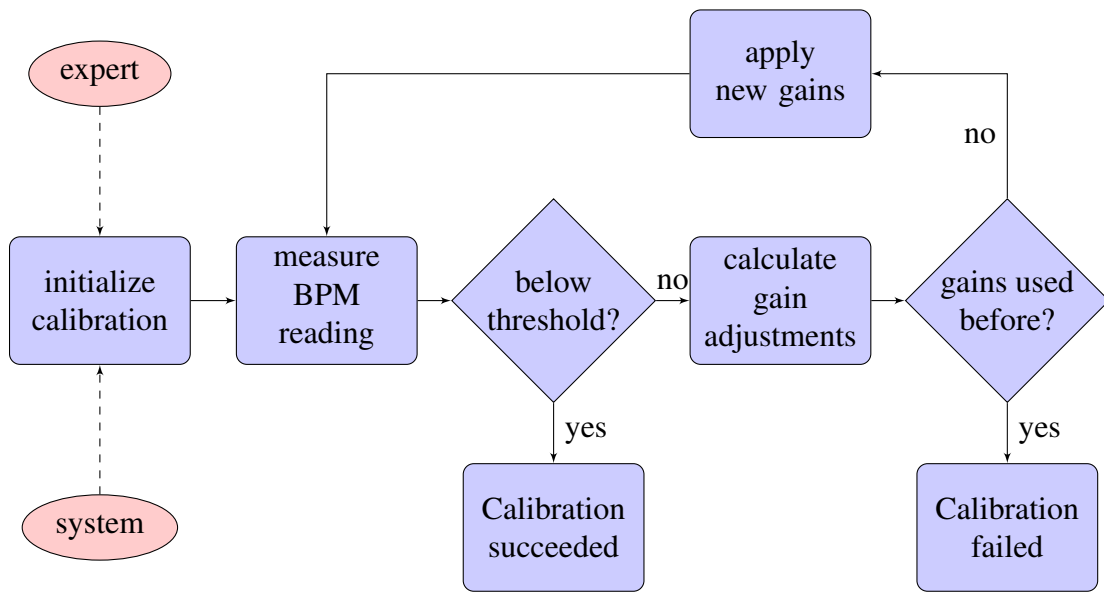


Figure 5.3: The expert gives the parameters for the calibration of the BPMs and the system prepares all needed hardware. Then the BPM reading with the signal from the frequency generator is taken and compared to the threshold. If it is below the threshold then the BPM is considered calibrated. If not then a gain adjustment, with the step size given during setup, is calculated and applied if it has not been tried before. If it has been applied before it would lead to an endless loop of calibration attempts and the calibration is failed. If it has not been tried before then it is applied and the process starts from the beginning. In addition, after a certain number of iterations the calibration is also considered to be failed if it did not succeed beforehand.

optimal gain setting should be. Then the iterative search is performed around the predicted optimal setting with a very fine step-size, like the first version of this software did. One change is, that the average gain will not be kept at the previous value, but instead one of the gains will be kept at zero, while the other one is increased. This will then also prevent the gains from running away, as one is fixed at zero, while the other one is used for the proper settings. Also, it is not checked if a gain setting has been used before, which might lead to an infinite loop. This can then be seen by the user and aborted. As the workload is now offloaded to an IOC and it does not freeze CSS anymore, one can see the procedure optimize the gains in real-time. The optimization takes a few seconds until it converges. In addition, a larger user interface has been designed, where one can see the parameters of the calibration quite easily (see figure 5.4). There one has an overview of the optimization parameters of each BPM and can also start individual BPMs for gain calibration with individual buttons.

		ON ●	Global Ready/OK ■	0,0500			7,0 sec to 160,0 sec		113,80 / 120,0 sec						
		all ON ●													
BPM	ENA	OK	ITER	STEP	DELTA	SLOPE	OFFSET	BPM	ENA	OK	ITER	STEP	DELTA	SLOPE	OFFSET
1 X	<input type="checkbox"/>	<input checked="" type="checkbox"/>	2	0,001C	0,0137	7,8505	-0,6376	1 Y	<input checked="" type="checkbox"/>	<input checked="" type="checkbox"/>	2	0,001C	0,0167	7,8151	1,2499
2 X	<input type="checkbox"/>	<input checked="" type="checkbox"/>	2	0,001C	0,0005	7,8115	-1,1371	2 Y	<input checked="" type="checkbox"/>	<input checked="" type="checkbox"/>	3	0,001C	0,0272	7,7970	-3,9851
6 X	<input type="checkbox"/>	<input checked="" type="checkbox"/>	2	0,001C	0,0135	7,8360	-2,0361	6 Y	<input checked="" type="checkbox"/>	<input checked="" type="checkbox"/>	3	0,001C	0,0177	7,8230	-6,0611
7 X	<input type="checkbox"/>	<input checked="" type="checkbox"/>	3	0,001C	0,0181	7,8128	-0,2861	7 Y	<input checked="" type="checkbox"/>	<input checked="" type="checkbox"/>	2	0,001C	0,0023	7,8170	-2,5311
8 X	<input type="checkbox"/>	<input checked="" type="checkbox"/>	2	0,001C	0,0034	7,8118	-3,8761	8 Y	<input checked="" type="checkbox"/>	<input checked="" type="checkbox"/>	2	0,001C	0,0061	7,8115	-2,6181
9 X	<input type="checkbox"/>	<input checked="" type="checkbox"/>	3	0,001C	0,0172	7,8369	-0,5591	9 Y	<input checked="" type="checkbox"/>	<input checked="" type="checkbox"/>	2	0,001C	0,0043	7,8235	-0,0491
10 X	<input type="checkbox"/>	<input checked="" type="checkbox"/>	2	0,001C	0,0080	7,8270	-0,3301	10 Y	<input checked="" type="checkbox"/>	<input checked="" type="checkbox"/>	2	0,001C	0,0022	2,9485	-0,7611
11 X	<input type="checkbox"/>	<input checked="" type="checkbox"/>	2	0,001C	0,0121	7,8102	-1,4051	11 Y	<input checked="" type="checkbox"/>	<input checked="" type="checkbox"/>	2	0,001C	0,0003	2,9554	0,1994
12 X	<input type="checkbox"/>	<input checked="" type="checkbox"/>	3	0,001C	0,0175	7,8511	-3,3231	12 Y	<input checked="" type="checkbox"/>	<input checked="" type="checkbox"/>	2	0,001C	0,0006	2,9572	-0,0851
13 X	<input type="checkbox"/>	<input checked="" type="checkbox"/>	3	0,001C	0,0217	7,8340	-4,5601	13 Y	<input checked="" type="checkbox"/>	<input checked="" type="checkbox"/>	2	0,001C	0,0053	2,9538	-1,6901
14 X	<input type="checkbox"/>	<input checked="" type="checkbox"/>	2	0,001C	0,0035	7,8078	-2,0751	14 Y	<input checked="" type="checkbox"/>	<input checked="" type="checkbox"/>	2	0,001C	0,0049	2,9646	-1,0011
15 X	<input type="checkbox"/>	<input checked="" type="checkbox"/>	2	0,001C	0,0119	7,8158	-1,0561	15 Y	<input checked="" type="checkbox"/>	<input checked="" type="checkbox"/>	2	0,001C	0,0025	2,9401	-0,5851
16 X	<input type="checkbox"/>	<input checked="" type="checkbox"/>	3	0,001C	0,0267	7,8532	0,1767	16 Y	<input checked="" type="checkbox"/>	<input checked="" type="checkbox"/>	2	0,001C	0,0067	2,9458	1,3208
17 X	<input type="checkbox"/>	<input checked="" type="checkbox"/>	2	0,001C	0,0077	7,8053	-1,3941	17 Y	<input checked="" type="checkbox"/>	<input checked="" type="checkbox"/>	3	0,001C	0,0103	7,7956	-0,1941
18 X	<input type="checkbox"/>	<input checked="" type="checkbox"/>	3	0,001C	0,0134	7,8190	-5,9431	18 Y	<input checked="" type="checkbox"/>	<input checked="" type="checkbox"/>	3	0,001C	0,0099	7,8053	-3,0511
19 X	<input type="checkbox"/>	<input checked="" type="checkbox"/>	3	0,001C	0,0218	7,8236	4,2698	19 Y	<input checked="" type="checkbox"/>	<input checked="" type="checkbox"/>	3	0,001C	0,0185	7,8273	-5,7171
ecolgun X	<input type="checkbox"/>	<input checked="" type="checkbox"/>	3	0,001C	0,0114	5,3103	-4,1421	ecolgun Y	<input checked="" type="checkbox"/>	<input checked="" type="checkbox"/>	3	0,001C	0,0087	5,3054	7,5616
ecolcol X	<input type="checkbox"/>	<input checked="" type="checkbox"/>	2	0,001C	0,0120	5,3225	2,0592	ecolcol Y	<input checked="" type="checkbox"/>	<input checked="" type="checkbox"/>	3	0,001C	0,0192	5,2909	5,6000
20 X	<input type="checkbox"/>	<input checked="" type="checkbox"/>	3	0,001C	0,0276	7,8380	-5,4771	20 Y	<input checked="" type="checkbox"/>	<input checked="" type="checkbox"/>	3	0,001C	0,0175	7,8124	0,9170
anke2 X	<input type="checkbox"/>	<input checked="" type="checkbox"/>	3	0,001C	0,0149	7,8116	-0,6521	anke2 Y	<input checked="" type="checkbox"/>	<input checked="" type="checkbox"/>	3	0,001C	0,0030	7,8045	-1,9531
21 X	<input type="checkbox"/>	<input checked="" type="checkbox"/>	3	0,001C	0,0199	7,8442	0,7223	21 Y	<input checked="" type="checkbox"/>	<input checked="" type="checkbox"/>	2	0,001C	0,0135	7,8315	-1,5621
22 X	<input type="checkbox"/>	<input checked="" type="checkbox"/>	3	0,001C	0,0095	7,8191	0,0021	22 Y	<input checked="" type="checkbox"/>	<input checked="" type="checkbox"/>	3	0,001C	0,0196	7,8205	-2,1841
23 X	<input type="checkbox"/>	<input checked="" type="checkbox"/>	3	0,001C	0,0109	7,8242	-0,4311	23 Y	<input checked="" type="checkbox"/>	<input checked="" type="checkbox"/>	3	0,001C	0,0073	2,9533	1,6896
24 X	<input type="checkbox"/>	<input checked="" type="checkbox"/>	3	0,001C	0,0012	7,8316	0,3705	24 Y	<input checked="" type="checkbox"/>	<input checked="" type="checkbox"/>	2	0,001C	0,0025	2,9535	-0,8461
25 X	<input type="checkbox"/>	<input checked="" type="checkbox"/>	3	0,001C	0,0231	10,0672	15,986	25 Y	<input checked="" type="checkbox"/>	<input checked="" type="checkbox"/>	0	0,001C	1,5099	0,0000	0,0000
26 X	<input type="checkbox"/>	<input checked="" type="checkbox"/>	2	0,001C	0,0023	7,8157	-2,1201	26 Y	<input checked="" type="checkbox"/>	<input checked="" type="checkbox"/>	2	0,001C	0,0042	2,9432	1,1303
27 X	<input type="checkbox"/>	<input checked="" type="checkbox"/>	2	0,001C	0,0034	7,7851	-2,1571	27 Y	<input checked="" type="checkbox"/>	<input checked="" type="checkbox"/>	2	0,001C	0,0048	2,9684	0,4217
28 X	<input type="checkbox"/>	<input checked="" type="checkbox"/>	2	0,001C	1,0572	8,0002	-2,1201	28 Y	<input checked="" type="checkbox"/>	<input checked="" type="checkbox"/>	2	0,001C	0,0053	2,9529	2,5003
29 X	<input type="checkbox"/>	<input checked="" type="checkbox"/>	2	0,001C	0,0084	7,8125	-3,2561	29 Y	<input checked="" type="checkbox"/>	<input checked="" type="checkbox"/>	3	0,001C	0,0234	7,7818	1,0523

Figure 5.4: A screen capture of the new version of the gain zero calibration. The individual BPMs are listed in their row with several numbers giving information about the state of the calibration of the BPM. The "ENA" button allows the start of an individual calibration of a single BPM. The "OK" LED indicates if the BPM can be calibrated right now, by looking at several boundary conditions, like no beam, the Libera system and frequency generators running and others. Next to it, in the "ITER" field, the number of iterative steps needed for the calibration to converge are displayed or the current step is given if it is running. In case the calibration does not converge, this number will keep counting up and the calibration can be aborted by the user. The "STEP" entry field allows of configure the step-size for the gain changes of the iterative calibration procedure. The important number one optimizes is "DELTA", which gives the deviation of the BPM from a zero reading and thus proper calibration. As a default optimization goal 0.05 mm (top text box) is given. "SLOPE" and "OFFSET" are calculated and used in the predictive search to find a good starting point for the iterative procedure. They are computed as parameters of the first predictive measurement and one can see that the BPM behaves as expected as one has an expectation, what the "SLOPE" should be for certain BPMs and if it deviates by a lot, then further investigation is needed, to figure out which part of the BPM is malfunctioning.

Beam-based Alignment

6.1 General Explanation

Beam-based alignment is used to determine the offset between the centers of Beam Position Monitors (BPMs) and quadrupoles. As the name already indicates it uses the beam to determine that offset. In general, one looks at the change of the orbit when changing the strength of one quadrupole and tries to minimize that orbit change. The position where there is no orbit change is the optimal position inside the quadrupole. The change of the orbit can be described with equation (6.1), which is later on derived in section 6.3.

$$\Delta x(s) = \frac{\Delta k x(s_0) \ell}{B\rho} \cdot \frac{1}{1 - k \frac{\ell \beta(s_0)}{2B\rho \tan \pi Q}} \cdot \frac{\sqrt{\beta(s)} \sqrt{\beta(s_0)}}{2 \sin \pi Q} \cdot \cos(\phi(s) - \phi(s_0) - \pi Q) \quad (6.1)$$

The description of the parameters of this equation can be seen in table 6.1. As one does not know all the parameters in this equation precisely, one has to do multiple measurements and fit

Parameter	Meaning
Δx	Orbit change
s	Measurement position
s_0	Position of quadrupole
Δk	Change in quadrupole strength
$x(s_0)$	Position of the beam with respect to the magnetic center of the quadrupole
ℓ	Length of quadrupole
$B\rho$	Magnetic rigidity of the beam
k	Quadrupole strength
β	Beta function
Q	Betatron tune
ϕ	Betatron phase

Table 6.1: Explanation of the parameters of equation (6.1).

a merit function in order to find the optimal position. The merit function used for that is given by:

$$f = \frac{1}{N_{\text{BPM}}} \sum_{i=1}^{N_{\text{BPM}}} (x_i(+\Delta k) - x_i(-\Delta k))^2 \propto (\Delta x(s))^2 \propto (x(s_0))^2 \quad (6.2)$$

This merit function takes two measurements, once with increased and once with decreased quadrupole strength. The position measurements for both settings are then subtracted from each other and added in quadrature. This yields a merit function which has the shape of a parabola around its minimum, where the minimum of the parabola is the optimal position inside the quadrupole.

6.2 Usage of Beam-based Alignment in other Accelerators

Beam-based alignment is a commonly used technique in many accelerators [48, 49, 50, 51]. There are multiple ways to approach the problem, but finally everything requires usage of the equation given in (6.1). A common approach is the method used with the merit function as described above. If each magnet is individually powered by a power supply one can easily vary the current through the magnet and thus its strength, as one would otherwise measure an overlaid effect of the multiple varied quadrupoles. This approach, using quadrupoles with individual power supplies, has been used in [48]. If more than one magnet is powered by one power supply, one has to use different methods to vary the individual quadrupole strength. One option is to use shunt resistors to bypass some of the current of the quadrupole and thus reduce its strength [52]. An other option is to add additional back-leg windings to the quadrupoles, with which one can then vary the strength by powering them independently [53].

For the experiment at COSY, both, back-leg windings and active shunts are used to perform the beam-based alignment, as each of the quadrupoles do not have an individual power supply. The measurements with back-leg windings are described in sections 6.6 and 6.7 and the measurements with the active shunts are described in section 6.8.

6.3 Derivation of Formula for Orbit Change

In order to understand where equation (6.1) is coming from, one can start with the Orbit Response Matrix (ORM). For a more detailed description of the ORM see section 3.6. The ORM describes the behavior of the orbit when one changes the strength of one element in the ring. It is intended to give a connection between the change of a steerer strength and the corresponding orbit change. Thus the effect of a dipole, which are used as steerers, can be extracted out of the ORM. The formula for that is

$$\Delta x(s) = \theta \times \frac{\sqrt{\beta(s)} \sqrt{\beta(s_0)}}{2 \sin \pi Q} \cos(\phi(s) - \phi(s_0) - \pi Q). \quad (6.3)$$

Here the parameter θ describes the kick of the dipole and the other parameters are the same as given in table 6.1. The kick of a dipole can be expressed with the magnetic field by

$$\theta = \frac{\Delta B(s_0)\ell}{B\rho}, \quad (6.4)$$

where ΔB is the change of the magnetic field of the magnet and $B\rho$ is the magnetic rigidity, which is a constant quantity for the accelerator.

When one changes the strength of a quadrupole the effect on the orbit is quite similar to the change of a dipole kick. The change of the strength with a shifted quadrupole is an effective change of the dipole field, which the beam sees. In general, this is more complicated, thus, a first order approximation is used. The change in tune, beta function and betatron phase are all effects of second order when changing the quadrupole strength and can be assumed to be constant for the derivation.

At first, the change of the effective dipole field has to be calculated. For this one uses

$$\Delta B = (k + \Delta k)(x + \Delta x) - kx = \Delta kx + \Delta xk + O(\Delta k\Delta x), \quad (6.5)$$

as the magnetic field of a quadrupole along one axis is given by $B = kx$. The term of equation (6.5), which includes both Δx and Δk , is small and can also be neglected for a first order approximation. Now, one can insert equation (6.4) and equation (6.5) into equation (6.3) with $s = s_0$ in order to get

$$\Delta x = \frac{(\Delta kx + \Delta xk)\ell}{B\rho} \frac{\beta}{2 \sin \pi Q} \cos \pi Q. \quad (6.6)$$

This can be solved for Δx and one arrives at

$$\Delta x = \Delta kx \frac{\kappa}{1 - \kappa}, \quad \text{with } \kappa = \frac{\beta\ell}{2B\rho \tan \pi Q}. \quad (6.7)$$

With this, one can insert equation (6.7) into equation (6.5) and after some simplification one gets

$$\Delta B = \Delta kx \frac{1}{1 - k\kappa}. \quad (6.8)$$

Finally, one inserts equation (6.4) and equation (6.8) into equation (6.3) to arrive at the result of

$$\Delta x(s) = \frac{\Delta kx(s_0)\ell}{B\rho} \cdot \frac{1}{1 - k\frac{\ell\beta(s_0)}{2B\rho \tan \pi Q}} \cdot \frac{\sqrt{\beta(s)}\sqrt{\beta(s_0)}}{2 \sin \pi Q} \cdot \cos(\phi(s) - \phi(s_0) - \pi Q), \quad (6.9)$$

which is exactly the same as equation (6.1).

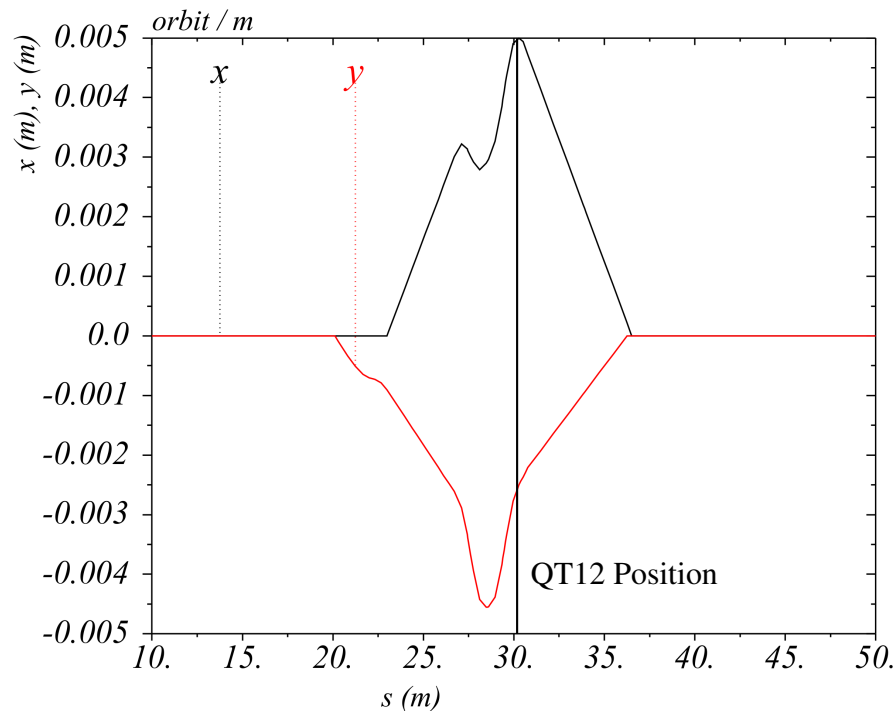


Figure 6.1: Simulated bump at the position of the quadrupole QT12. The black curve is the horizontal orbit and the red one is the vertical orbit. Outside of the bump region the orbit is perfectly flat. The bumps are constructed such, that at the position of quadrupole QT12, which is indicated by the vertical line, they are 5 mm in horizontal and -2.5 mm in vertical direction. Note that the y-scale is depicted in meters.

6.4 Simulations

In order to see that the expected behavior, as derived just before, is also present in the COSY lattice, one has to do some simulations to confirm that. This has been done with MAD-X¹ [54] and the procedure and results are discussed in the following.

In the simulations there are two ways to create a situation where the beam does not go central through the quadrupole. One is to move the beam with nearby steerers, which can also be done in the experiment. The other is to shift the quadrupole around and leave the beam where it is. This is not possible in the experiment, as it is not easy to move a quadrupole magnet quickly and precisely. The beam movement was realized with nearby steerers around the desired quadrupole, QT12, which was also the first to be looked at in the experiment. All the other steerers were left turned off in the simulation. A depiction of one simulated bump can be seen in figure 6.1.

Several different combinations of bumps of different magnitude were calculated and then used for the simulations. These different bumps spanned a grid of 7×7 points with a step size of 2.5 mm beam movement at the position of the quadrupole. While the bumps were applied in the simulation, the strength of the individual quadrupole was modulated by $\pm 3\%$ to see the effect

¹ <http://madx.web.cern.ch/madx/>

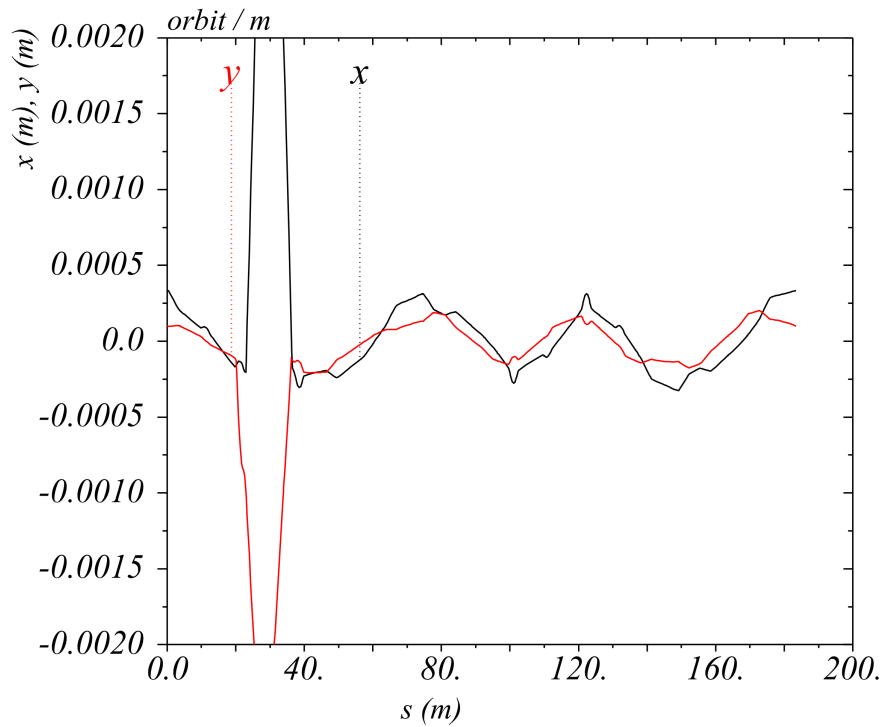


Figure 6.2: Example for the orbit distortion seen in the simulations with a quadrupole strength change of 3% and a bump setting of 5 mm in horizontal and -2.5 mm in vertical direction. One can see an orbit distortion due to the changed quadrupole strength with an amplitude of about 0.5 mm. The vertical distortion is a little smaller, than the horizontal one, as the bump in vertical direction is also smaller by a factor of 2. It does not mean that with the same bump size there will be the same orbit distortion, as the beta functions in horizontal and vertical direction differ. The y-scale has been zoomed in to show the orbit distortion and not only the bump as a main feature. Note that the y-scale is given in meters.

on the orbit. This modulation of the quadrupole strength then leads to an orbit distortion all over the ring, which can be described with equation (6.1). One example of the orbit distortion can be seen in figure 6.2.

For each simulated point, the merit function (see equation (6.2)) was computed. Then a fit to the computed values of the merit function was performed and the result, as expected, gave the optimal beam position at 0 mm. A depiction of the paraboloid fit can be seen in figure 6.3. In that plot one can also nicely see that the effect is not the same in horizontal and vertical direction. This is due to the fact that the beta functions at the position of the quadrupole are different in both planes and thus the magnitude of the orbit distortion changes accordingly, which is also reflected in equation (6.1).

The second method, where one moved the quadrupole in the simulation, was also simulated in a similar way. Instead of moving the beam, the quadrupole was moved and then also modulated by $\pm 3\%$. It gave the same result that the optimal position is at 0 mm, as expected with the simulation.

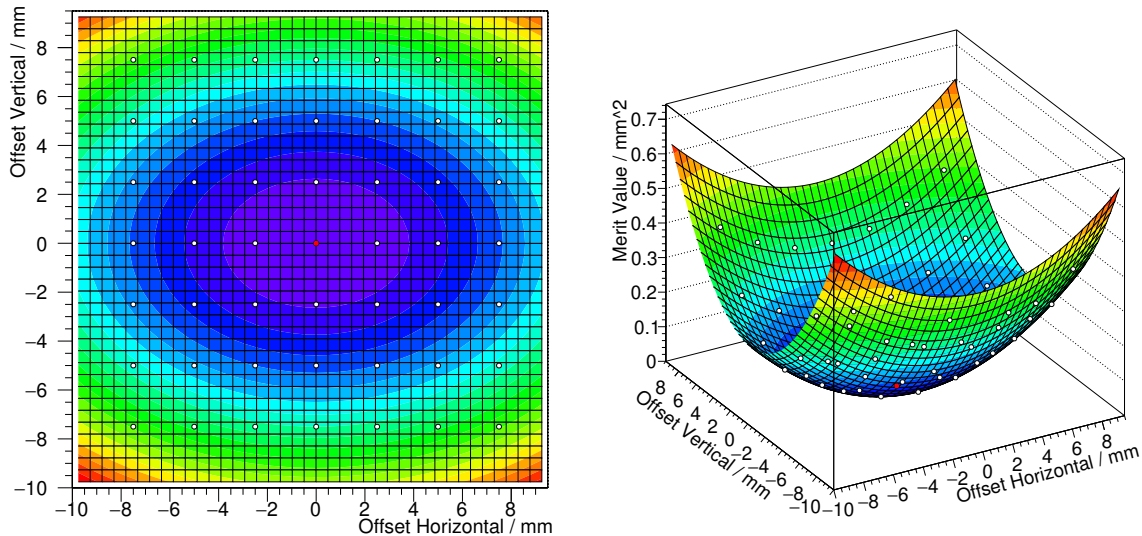


Figure 6.3: Paraboloid fits of the simulated beam-based alignment. The beam was moved to the white points and the effect on the orbit, when changing the quadrupole strength of QT12 by $\pm 3\%$ simulated. Then a fit to the computed merit function was done. The minimum, i.e. the optimal beam position, was perfectly at the center, as expected.

6.5 Measurement Procedure

If one has a look at the merit function used (see equation (6.2)), it is quite clear what has to be measured. One needs an orbit measurement with slightly increased and with slightly reduced quadrupole strength. But in order to obtain that, the accelerator settings have to be changed during the measurement. This was done via the orbit control software (see section 4.4). Usually the orbit control software is used to correct the orbit to a predefined optimal orbit, but if one sets the correction strength to zero it can also be used to change the orbit easily with external scripts. After the beam preparation, one can set the steerer parameters through this software to create local orbit bumps and also change the quadrupole strength. The change of the quadrupole strength through the orbit control software was only possible for a subset of all quadrupoles. This subset of all quadrupoles had back-leg windings installed. These are usually configured and used as steerers, but it is possible to re-cable them to act as a quadrupole in addition to the main quadrupole. For the quadrupoles which do not have those back-leg windings, an other method was developed and will be explained later in section 6.8.

For the first measurement in November 2017, a very basic procedure was used for the measurement. A bump was applied for multiple cycles and from cycle to cycle the quadrupole strength was changed. This method takes quite some time, but yields a lot of data for the orbit measurement. The downside of this method is that one does not have a reference orbit for each cycle, as the bump and quadrupole strength change is always set. This then leads to additional systematic errors depending on the precision of the beam injection. As a result of that a new method was developed for the next measurements in order to get a reference measurement for each cycle.

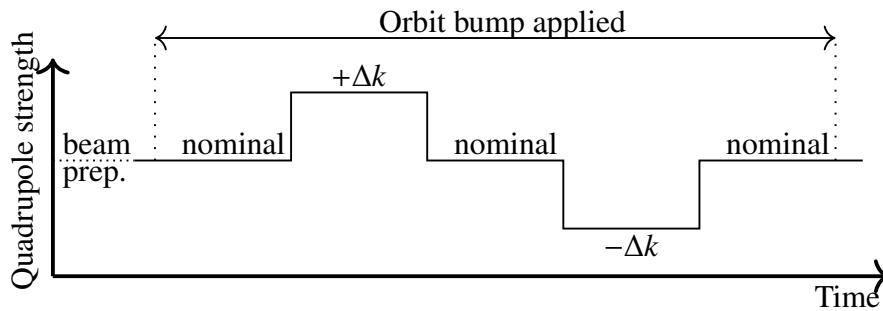


Figure 6.4: Depiction of the measurement pattern used for the measurements done in May 2018 and February 2019. After the beam preparation the reference orbit was measured for a short time frame and then the bump was applied. During the time, when the bump was applied the quadrupole strength was varied by $\pm\Delta k$ while going back to the nominal quadrupole strength in between the variations. At the end the bump was removed and a short measurement of the reference orbit was performed.

This new method was used in the May 2018 and February 2019 measurements. It does the application of the bump and adjustment of the quadrupole strength during the cycle, instead of being static for the full duration of the cycle like the previous method. Thus one gets a reference orbit measurement and is able to correct for possible changes from cycle to cycle. After the beam preparation, one takes a measurement of the reference orbit and then applies the bump. The next step is to take a measurement of the orbit with the bump and then change the quadrupole strength to a slightly higher value, go back to the original quadrupole strength value and then go to a slightly lower value. After that one goes back to the original quadrupole strength value and then removes the bump. At the end one takes a reference orbit measurement again. This leads to two measurements for the reference orbit at the start and the end and one also gets three measurements of the bump, one when it is applied, one in between and one before it is removed. This enables a correction for all possible changes of the orbit during the measurement, as there is always a reference value in between. A depiction of that structure is given in figure 6.4.

6.6 Measurements of Quadrupole QT12

For quadrupole QT12 multiple measurements were done. The first measurement was performed in a JEDI beam time in November 2017, where the method of beam-based alignment was tested as a proof of principle. The second measurement with quadrupole QT12 was done in an other JEDI beam time in May 2018, where the previous measurement was repeated with a faster procedure for more statistics.

6.6.1 November 2017 Measurement

During first measurement in November 2017, 19 data points were measured. These data points were distributed along the horizontal and vertical axis in order to fit them independently. The

merit function which was used to evaluate the data is given in equation (6.2) in section 6.1.

Measurement Procedure

The procedure for the beam-based alignment measurement was that a change of magnet settings happened once every cycle. This means that it took six cycles of three minutes each for the collection of one data point. The first cycle was used to set the measurement up and the remaining five are used for the actual measurement with a change of quadrupole setting each cycle. The restriction to perform the measurement this way was due to the scripts used for the measurement and the boundary conditions, as it was performed during an other JEDI beam time, where the cycle length was not well adjusted for the beam-based alignment measurement. As a first step an orbit bump was applied at the position of the quadrupole QT12. Examples how a horizontal and vertical orbit bump looked like during the measurement can be seen in figure 6.5. The adjustment and application of the bump took one of the six cycles. During the next five cycles the back-leg winding of quadrupole QT12 was set to -800 bit, -400 bit, 0 bit, 400 bit and 800 bit (out of a total range of -2047 bit to 2048 bit, which correspond to ± 30 A), each for one cycle. These settings are proportional to the current through the back-leg winding and therefore the quadrupole strength. During the next cycle the bump was removed and the bump for the next data point was applied. The variation of the current through back-leg winding resulted in a strength change of the quadrupole, as it is mounted on the quadrupole QT12 and was configured to provide an additional quadrupole field.

During the measurement time of one shift (8 hours) it was possible to take 19 data points. 10 of them are in horizontal direction and 10 of them are in vertical direction, where one point was shared.

Fitting of Data

For each of those data point the merit function was calculated. This was done separately for the ± 400 bit and ± 800 bit settings, as the effect of the magnitude of the quadrupole strength change was also of interest. The cycles needed for the computation of the merit function were extracted from the measured orbit data taken during the measurement and the merit function was computed. With the computed points of the merit function one could then fit a parabola to the data for each direction and extract the minimum of that parabola. The parabola fits for ± 400 bit are shown in the figures 6.6 and 6.7. In addition to just fitting the data for one direction, also a combined fit with a 3d paraboloid was performed, which is shown in figure 6.8. The minimum of the paraboloid then gives the optimal position of the beam inside the quadrupole. The optimal position is at (-1.981 ± 0.009) mm in horizontal direction and (1.156 ± 0.003) mm in vertical direction. The error on these values is the fit error, with the data points given an equal weight each.

Comparison between ± 400 bit and ± 800 bit Strength Changes

These results given in the text and shown in the pictures are for the measurement with ± 400 bit settings. The same analysis has also been done for the ± 800 bit settings, where the quadrupole

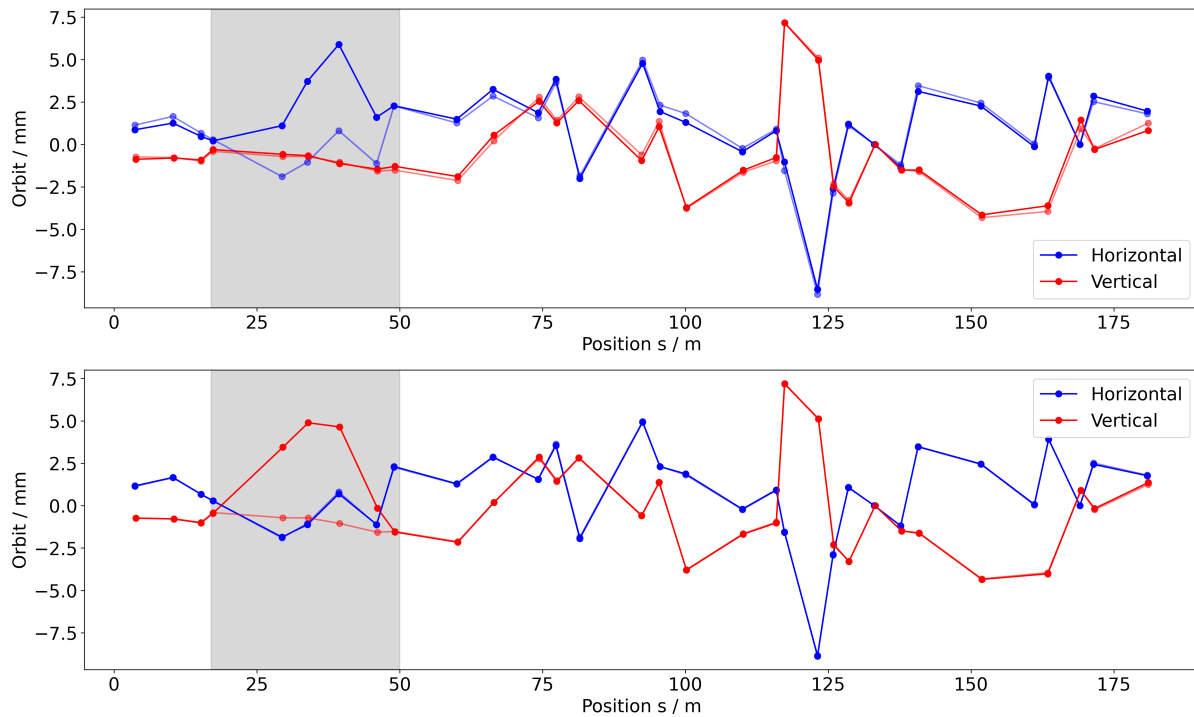


Figure 6.5: Example pictures showing the orbit bumps used during the measurement. The region where the bump is visible is shaded in gray to catch the eye. The blue lines depict the horizontal orbit and the red lines the vertical one. The more transparent lines show the reference orbit with no bump applied, whereas the solid lines show the orbit with the bump applied. In the top picture, a positive horizontal bump at ≈ 30 m is depicted and a positive vertical bump in the bottom one. One can see that the horizontal bump used was not quite perfectly closed, as the dark blue line also deviates from the reference (lighter blue line) outside of the bump region. However in the vertical direction the bump is closed very well, as such a deviation is not there. For the measurement the fact that the horizontal bump was not as well closed has no effect.

strength change is stronger and thus the orbit deviation larger. One effect one could see there is that the values of the merit function are four times as large, which was expected as the strength change was twice as big, thus the orbit changes were also twice as big and the merit function is quadratic.

A comparison for the optimal positions with ± 400 bit and ± 800 bit can be seen in Table 6.2. The results agree quite nicely with each other and one can also see that one does not necessarily need a higher change in quadrupole strength to get a result.

These results for the optimal position mean that if one positions the beam at that position the orbit will not be disturbed by a change of quadrupole strength and therefore one is at the magnetic center of the quadrupole. Additionally, the spin of the particles will also not be disturbed by the quadrupole, as the beam passes through the magnetic center.

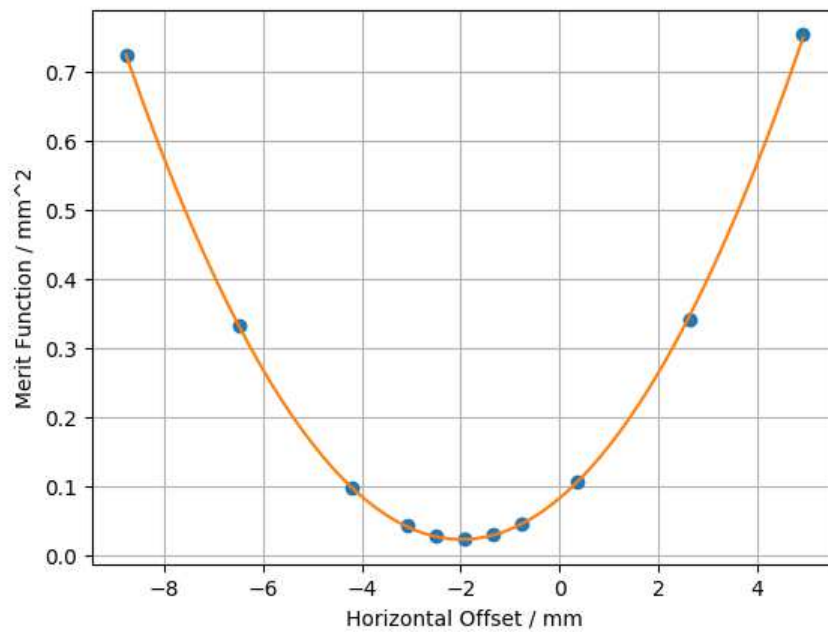


Figure 6.6: Parabola showing the fit of the merit function for the horizontal direction. For the fit all the data points were given an equal weight.

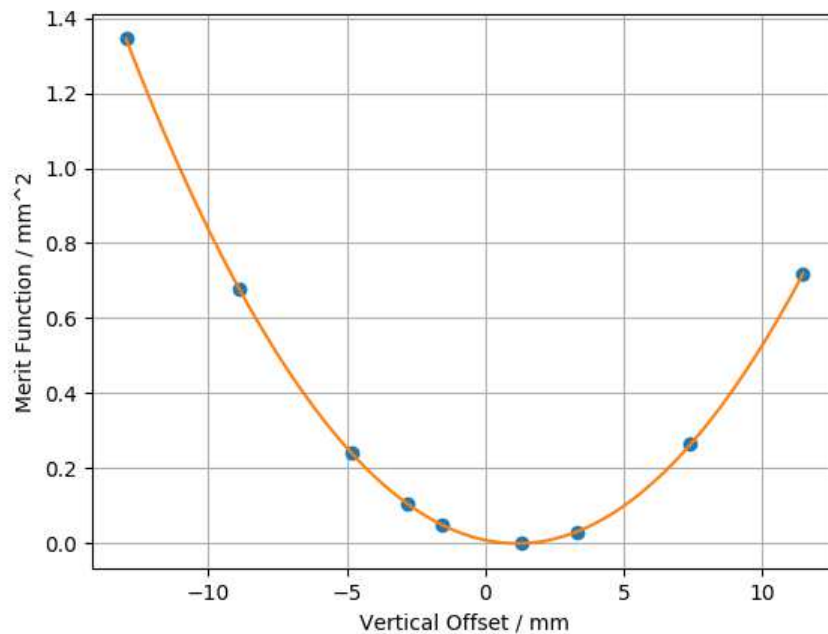


Figure 6.7: Parabola showing the fit of the merit function for the vertical direction. For the fit all the data points were given an equal weight.

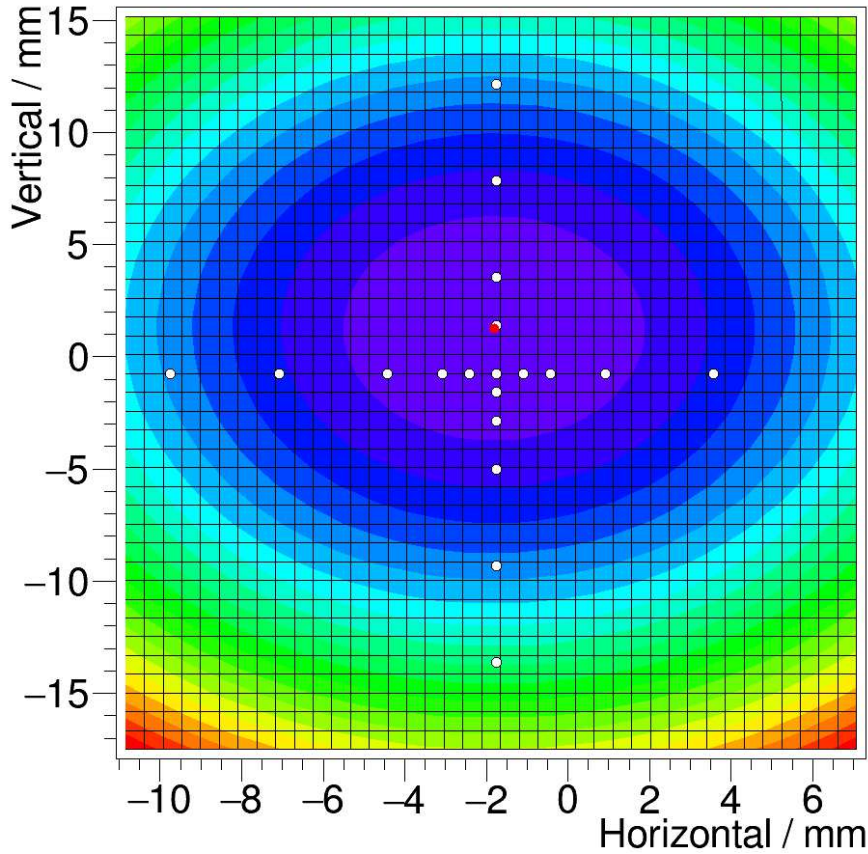


Figure 6.8: Paraboloid taking both horizontal and vertical direction into account for the fit of the merit function. For the fit all the data points were given an equal weight. The minimum, which is indicated by the red dot, is located at (-1.981 ± 0.009) mm in horizontal and (1.156 ± 0.003) mm in vertical direction.

Strength change	Optimal position	
	Horizontal	Vertical
± 400 bit	(-1.981 ± 0.009) mm	(1.156 ± 0.003) mm
± 800 bit	(-1.988 ± 0.007) mm	(1.160 ± 0.005) mm

Table 6.2: Comparison of the calculated optimal position for different settings for the back-leg winding and thus magnitudes of strength changes of the quadrupole.

6.6.2 May 2018 Measurement

For the second measurement in May 2018, a faster measurement procedure has been developed. This procedure does not use one cycle for each change of setting, but instead does all the changes in one cycle. Therefore, it only needs one cycle for one data point. In addition, one also prevents an influence from changes from cycle to cycle on the measurement of a data point, as different injection points of several μm have been observed [55]. This way it was possible to take more data in order to get more statistics and verify the measurement done in November 2017.

Measurement and Fits

The pattern for the quadrupole strength change and application of the bump used by the script was already shown in figure 6.4. At first, the beam is prepared and the reference orbit is recorded for a short time. Then the bump is applied and the quadrupole strength changes were made. Near the end of the cycle the bump was removed and the process started again with the next cycle. All of that was automated to have the changes happen at the same time points and also to make it easier for the people on shift and to prevent human error.

During this measurement four data sets of 51 points each were taken. The points were chosen to be randomly distributed in order to not get any bias due to choosing a specific pattern. The increase in data made it possible to do multiple independent fits to get an estimate for the variation of the optimal position. The fit of one such set of points can be seen in figure 6.9. Here the data points have an error assigned, which is computed from the BPM reading errors, which was not the case for the previous November measurement. The optimal position was extracted out of all sets and the comparison of them can be seen in figure 6.10. A thing one directly notices is that the variation of the optimal position is very small, thus the error estimate on the reading of the beam position monitors is most likely too large.

With this measurement it was shown that it is easily possible to determine the optimal position inside the quadrupole and that the measurement is consistent. As a next step one has to measure the optimal positions for more quadrupoles to see if the BPMs are off, or if this specific quadrupole is the only one with an offset BPM. The expectation was that all of the BPMs are off by some amount, as they are mounted on the beam pipe and not aligned with any of the alignment campaigns done at COSY.

Comparison to November 2017 Measurement

What one can see if one compares the results of the measurement done in November 2017 to the one in May 2018 is that they do not agree with each other. The measurement result from this measurement (May 2018) is an optimal beam position at (-1.14 ± 0.02) mm in horizontal direction and (2.08 ± 0.03) mm in vertical direction, whereas the measurement from November 2017 has a result of (-1.981 ± 0.009) mm in horizontal direction and (1.156 ± 0.003) mm in vertical direction. They differ by 0.84 mm in horizontal and 0.92 mm in vertical direction, which is significantly larger than the errors of the measurements would allow. This at first was unexpected, but it can be explained. During those measurements it was not made sure that

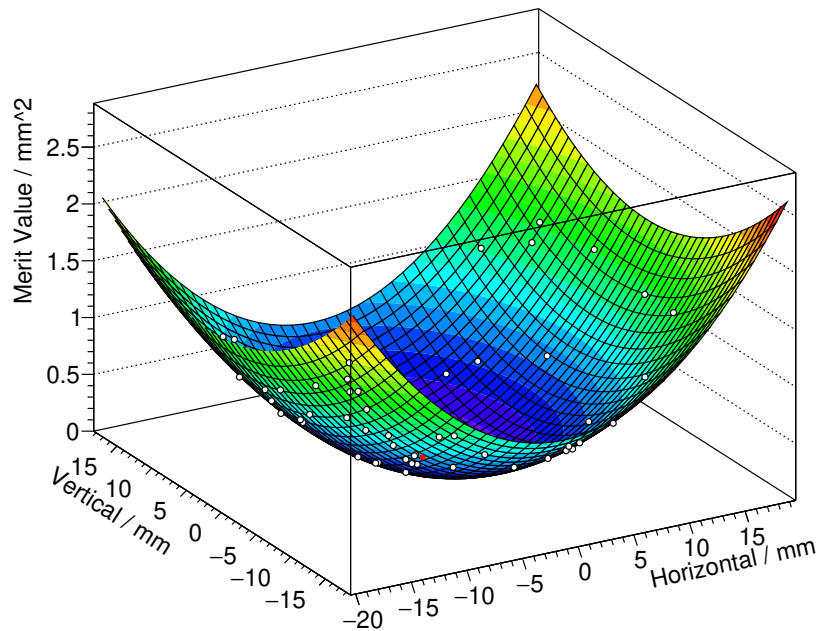


Figure 6.9: Fit example for one of the four measured sets in May 2018. All the white points shown are measured data points. The colored paraboloid is a fit to them, and the red point is the location of the minimum. The minimum is located at (-1.13 ± 0.04) mm in horizontal direction and (2.09 ± 0.04) mm in vertical direction.

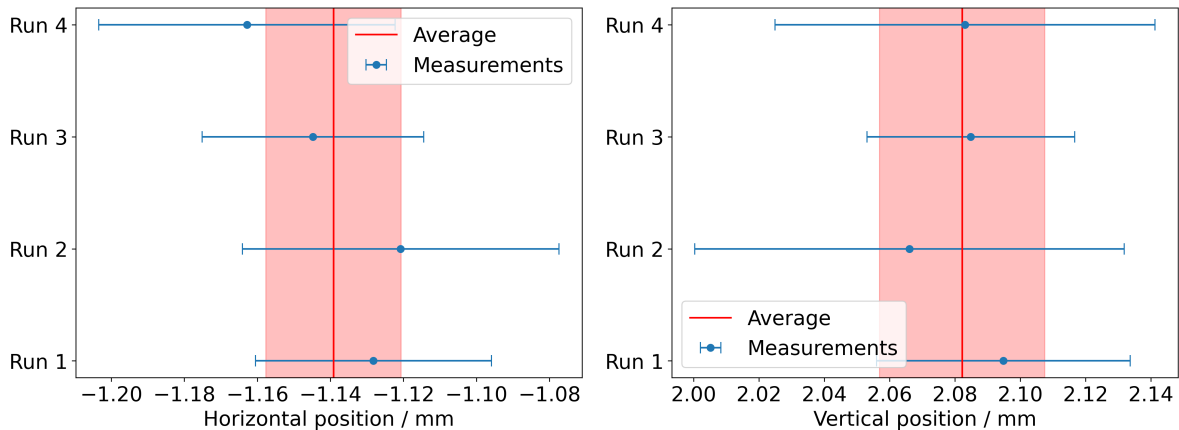


Figure 6.10: Comparison of optimal positions in quadrupole QT12 measured in multiple measurements in May 2018. The different runs/measurements each contain 51 randomly distributed data points used for the fit. The resulting optimal positions in quadrupole QT12 agree nicely. When looking at the size of the error bars and the spread of the data points it seems that the errors have been overestimated. The calculated average of the measurements is (-1.14 ± 0.02) mm in horizontal direction and (2.08 ± 0.03) mm in vertical direction.

the BPMs are correctly calibrated. More precisely, that the gain of the BPMs is properly set, such that equal signal on all pickups of the BPM leads to a zero position. In response to that observation, an automatic gain calibration for the BPMs has been developed (see chapter 5) to prevent this from happening in the future. Thus future measurements, done after these, will use the automatic gain calibration to make it consistent and comparable.

Number of Required Measurement Points

In order to get an idea what the optimal number of measured points for the next beam-based alignment measurement would be, the effect of the number of measured points was also determined. For that the four data sets were combined and different number of points were randomly drawn from the pool of 204 measured points. A total of 10000 fits with randomly drawn points were done for each choice for the number of points. Some examples for the resulting distributions of the optimal positions depending on the number of chosen points can be seen in figure 6.11. There one can clearly see, that with an increasing number of points, one can determine the optimal position better, as one would expect. The error of the fit, which is depicted in each of the lower panels, behaves as expected with an $N^{-\frac{1}{2}}$ trend. The standard deviation of the distribution for the optimal position (upper panel) also shrinks, whereas the mean stays the same. The standard deviation does not follow a $N^{-\frac{1}{2}}$ behavior, but decreases faster than that. As the standard deviation of the distribution for the optimal position reaches the BPM precision of 0.02 mm at 50 points, this amount of points was chosen for the future measurements, to balance time taken for the measurement and the precision of the measurement.

6.7 Measurement of all Quadrupoles with Back-leg Windings

During the February 2019 beam time, a measurement for all quadrupoles that have back-leg windings was performed. Although there were some delays at the start of the beam time due to accelerator problems, it was still possible to measure all twelve quadrupoles with back-leg windings. The measurement principle was the same as in May 2018 with an automated measurement script to make the measurement as easy as possible for the people on shift.

6.7.1 February 2019 measurement

Multiple measurements for each of the twelve quadrupoles were performed in order to have more statistics and a better result. The number of measurements for each quadrupole were mostly seven measured sets each, where some quadrupoles had more sets measured and others had less due to discarding failed measurements. The measurements took about half a day for each quadrupole and five to ten sets of 51 points each were generated. All those sets were fit and the optimal position was extracted. For a detailed explanation of the fit procedure please refer to the next section. With these extracted offsets one could average them to obtain one final value for each quadrupole for horizontal and vertical direction. This result can be seen in

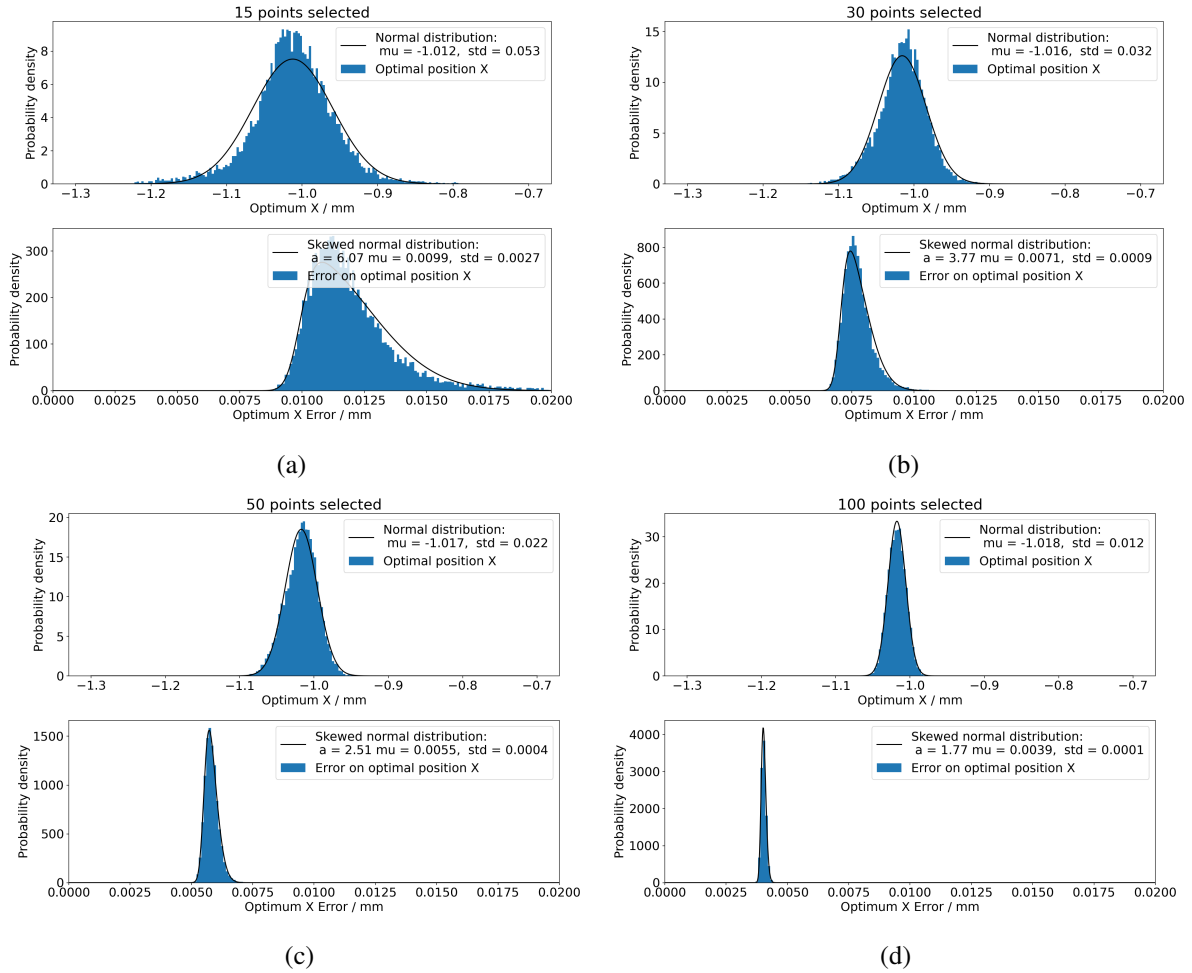


Figure 6.11: Distribution of optimal position for the x (horizontal) direction for 10000 fits with a number of randomly drawn points out of 204 points from the measured data of May 2018. The number of drawn points are 15, 30, 50 and 100 points for the corresponding panels (a) to (d), as given in the title of the plots. The upper panel for each chosen number of points shows the optimal position from the fit and the lower panel shows the fit error on that. For the optimal position a normal distribution was fitted to the distribution to determine the mean and standard deviation. One can clearly see that the mean does not change, depending on the chosen number of points, but the standard deviation does. One can see that the width of the distribution does shrink with an increasing number of points, but does not follow a $N^{-1/2}$ behavior. The fit error on the optimum has an asymmetric shape, thus a skewed normal distribution was chosen for the fit. Here the mean of the skewed normal distribution shows a $N^{-1/2}$ behavior, as one would expect. One can also see that the skewness of the function, which is the factor a , decreases as the number of points grow. This is due to the random choice of the points, as with higher number of points, there is a lower possibility to choose points with bad coverage of the fit area and thus a bad fit.

figure 6.14, which is located in the next section. There, one can see the optimal position of the beam inside the quadrupole to be in the center of it.

6.7.2 Fit

In order to extract the optimal position out of the measured data one first has to understand the measured pattern. The pattern is depicted in figure 6.4. At first the beam preparation is done, this part of the cycle is not interesting for the analysis. When the preparation is complete there is a small time frame where the orbit with out the applied bump is measured, this is to be able to crosscheck that the bump has the desired size. After that the bump is applied and the orbit is measured, this is one of the needed references. Then the quadrupole strength is varied to $+\Delta k$. Then again the quadrupole is set back to its default setting, this orbit is an other reference. Next the quadrupole strength is set to $-\Delta k$. After that again to the default value, where the third reference is. In the end the bump is removed and there is an additional time frame to crosscheck the size of the bump.

The three times where the bump is applied and the quadrupole is at default strength are there for detecting a potential drift of the orbit in the accelerator and being able to correct for that in case it appears. All three orbit measurements are compared and in case there is a drift, a correction for that is applied to the actual relevant time frames of the measurement, when the quadrupole strength is changed.

The two time points where the quadrupole strength is changed to $\pm\Delta k$ are the two time frames relevant for the measurement (compare with the merit function equation (6.2)). The orbit of those time frames are given as the input to the merit function to calculate the value for the current bump size. If required the values are corrected for potential orbit drifts, which is computed with the three reference measurements.

After all the values of the merit function for all positions in the measured data set are calculated a paraboloid is fit to the data. With that paraboloid one can extract the optimal position of the beam inside the quadrupole to be the minimum of the paraboloid.

To clean up the measurement an additional manual step of the analysis has been done. When the measured point and the fit did not agree well enough, the cycle where the point was measured has been checked. This way it was possible to exclude cycles where the measurement failed to apply the bump or execute the correct pattern due to software issues with COSY. It was found that the orbit control software became unresponsive in the night when the backup of the COSY computers was running and for all days this specific cycle, where the backup was running, had to be discarded.

An example showing one of those fits can be seen in figure 6.12. There, one fit for quadrupole QT04 is shown and a comparison of all the eight fits for quadrupole QT04 are shown in figure 6.13. There, one can see that the fits for all eight measured sets of 51 points each agree quite nicely with each other. The final values for all quadrupoles are shown in figure 6.14.

6.7.3 Results

With the now obtained optimal positions of the beam inside the quadrupole (see figure 6.14) the offset for some Beam Position Monitors (BPMs) can be calculated. For that, one has to have

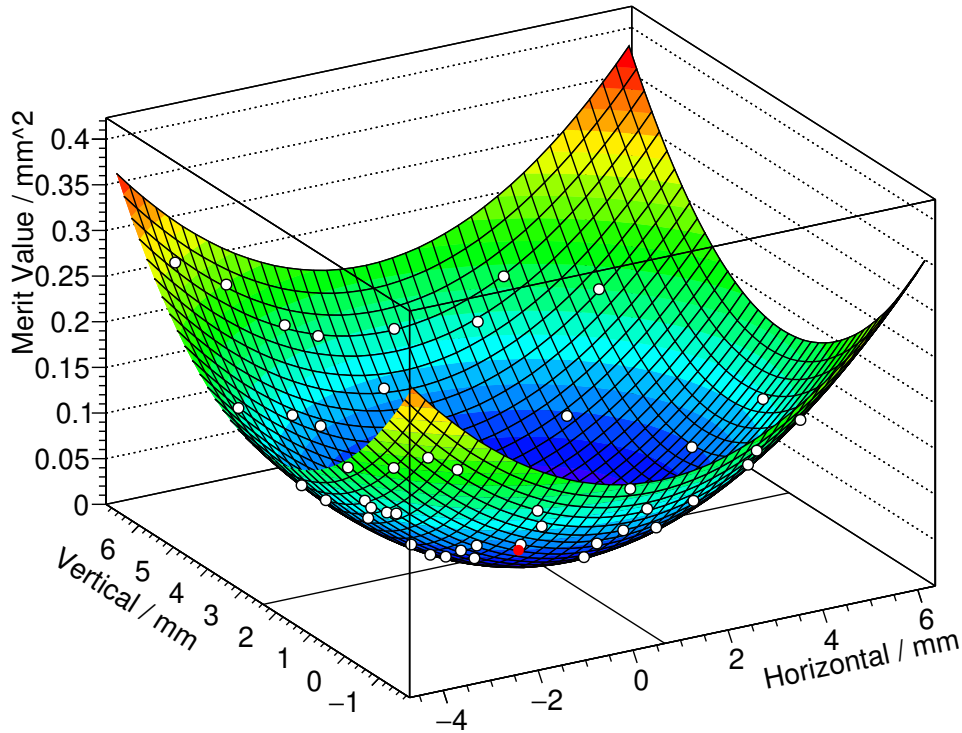


Figure 6.12: Example fit for the measurement of quadrupole QT04. The white points are the measurement points and the colored plane is a paraboloid fit to them. The minimum is marked by the red dot. The lines at the bottom are to guide the eye for reading the values.

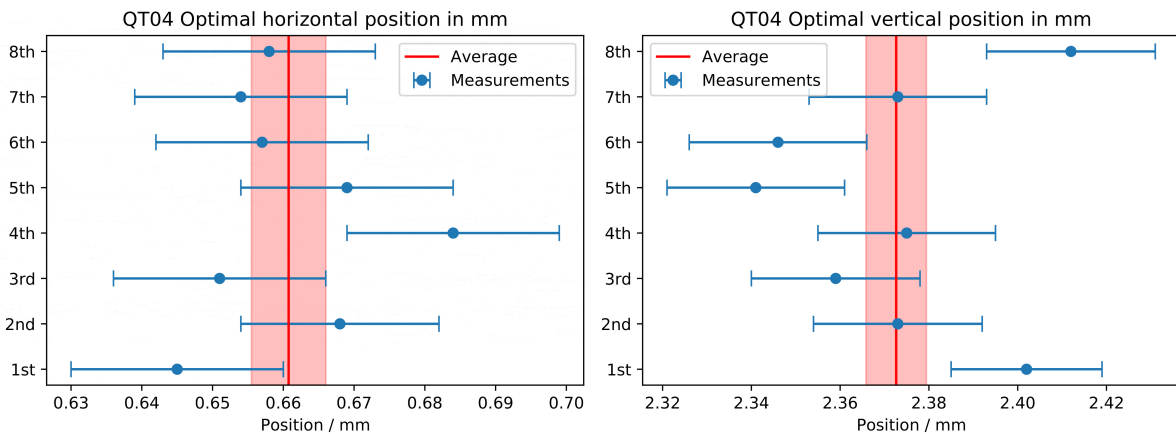


Figure 6.13: Comparison of all the eight fits for quadrupole QT04. The left plot shows the results for the horizontal direction and the right plot shows the results for the vertical direction. Each paraboloid fit, like depicted in figure 6.12, gives one value for the optimal horizontal and optimal vertical beam position inside the quadrupole. All eight results are compared here and an average of them is computed and shown with the red bar. The values agree quite nicely with each other.

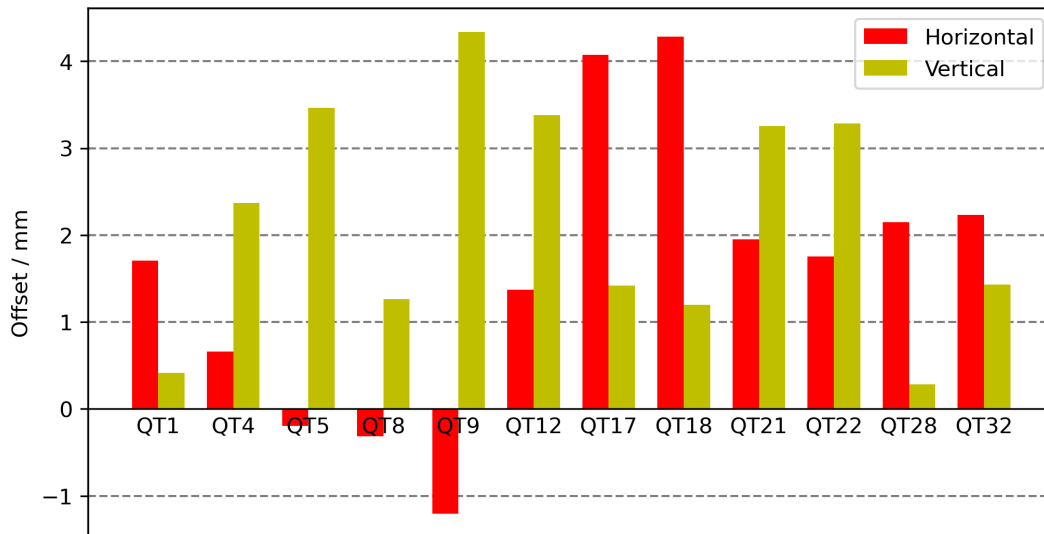


Figure 6.14: Optimal beam position inside the 12 quadrupoles with back-leg windings. The individual values are obtained from averaging several measurements for the optimal beam position inside the quadrupole.

a quadrupole up- and downstream of the BPM and can then interpolate the optimal positions measured in the quadrupoles to the BPM, to obtain its offset. An other option is available, when the BPM is very close to a quadrupole. Then one can take the optimal position inside the quadrupole as the offset of the BPM. This choice is not optimal, but better than no calibration at all for that BPM.

With the twelve quadrupoles measured it was possible to calculate the offset of six BPMs in total. Two of them in one straight section and four in the other. Four of the optimal positions inside the quadrupoles could not be used for a calibration of a beam position monitor, as they had no BPM sufficiently close by. In order to calibrate all BPMs, one has to measure the optimal position for all quadrupoles individually, to have one quadrupole on each side of the BPM. The resulting BPM calibration numbers are given in table 6.3.

6.7.4 Improvement of the Orbit

The offsets were first implemented in the April 2019 JEDI beam time. A short comparison was done between the orbit correction with and without the offsets applied. Out of that comparison it was visible that the offsets improved the orbit in the accelerator. Unfortunately, one can only see that in numbers for the vertical direction, as for the horizontal direction other parameters were also changed at the same time. In order to compare the orbits, the Root Mean Square (RMS) of the measured orbits has been computed. For the vertical direction, the orbit RMS_y decreased from 1.21 mm to 1.01 mm (by 17%) while at the same time the steerer currents needed to achieve that correction also decreased from an RMS_y current of 2.66 A to 2.10 A (by 21%). This improvement is significant as only six out of all 31 BPMs were calibrated and a further calibration should lead to an even better orbit in the machine.

BPM name	Horizontal Offset	Vertical Offset
BPM02 (s = 10.4 m)	(1.705 ± 0.008) mm	(0.416 ± 0.005) mm
BPM06 (s = 29.5 m)	(1.371 ± 0.007) mm	(3.382 ± 0.011) mm
BPM18 (s = 100.2 m)	(4.177 ± 0.007) mm	(1.308 ± 0.005) mm
BPM19 (s = 110.1 m)	(1.868 ± 0.005) mm	(3.273 ± 0.010) mm
BPM20 (s = 123.3 m)	(2.149 ± 0.007) mm	(0.281 ± 0.007) mm
BPM21 (s = 133.2 m)	(2.232 ± 0.008) mm	(1.430 ± 0.006) mm

Table 6.3: The calculated offsets that have been applied to the Beam Position Monitors (BPMs) are listed in this table. These offsets have to be subtracted from the BPM reading in order to be in the center of the quadrupole with a zero reading of the BPM. They were obtained via interpolation between quadrupoles up- and downstream of the BPM or directly taken from the optimal position inside the quadrupole, in case the BPM is right next to the quadrupole.

6.8 Measurement of all Quadrupoles in COSY

The measurement explained in the following has also been published in [56] and will be explained here in more detail compared to that publication.

6.8.1 New Power Supplies

In order to utilize the beam-based alignment measurement all around the ring, one needs a method to change the strength of one individual quadrupole. In the measurement, which was described in the previous section, it was done with back-leg windings, but not all quadrupoles are equipped with them. Therefore, now an other method has been used by bypassing or adding some current through the main coils of the quadrupoles, instead of creating an additional overlaid field like before.

In order to add or bypass a fraction of the current, source-sink power supplies² have been acquired and connected in parallel to one magnet. In total, four of those power supplies exist, thus one has to connect them as needed during the measurement. A schematic diagram showing how they are connected is depicted in figure 6.15 and a picture showing the power supply connected can be seen in figure 6.16. There one sees that the additional power supplies are connected in parallel to one magnet with fuses and a switch realized with a relay. This is done in order to not have them connected during the acceleration phase, which could damage the main power supplies of the quadrupoles or also the additional source-sink power supplies. During the beam time it turned out that it was indeed required to have the power supplies disconnected during the acceleration ramp, as due to a software malfunction it happened that one of the power supplies stayed connected during the acceleration ramp and that lead to a shutdown of the main power supply as the interlock triggered. Nothing was damaged due to that, but repeating this several times could damage the main power supplies and also no beam could be accelerated.

² Model NL20V20C40, bipolar - 4 quadrant power supply, Höcherl & Hackl, <https://www.hoecherl-hackl.de/>

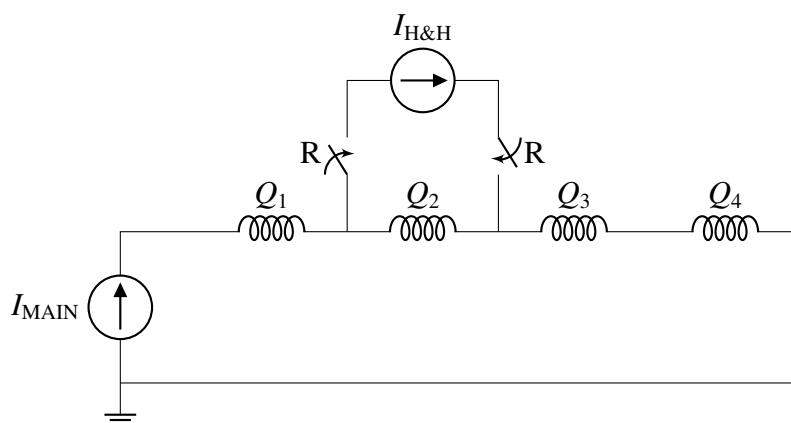


Figure 6.15: Schematic showing one additional power supply connected to a family of quadrupoles powered by a main power supply. The individual quadrupoles (Q_1 , Q_2 , Q_3 , Q_4) are all powered in series by the main power supply (I_{MAIN}). One of the quadrupoles has the additional power supply ($I_{\text{H\&H}}$) connected in parallel to add or bypass some current for that individual magnet. This additional power supply is disconnected with a relay (R) during the acceleration. Fuses, interlock and other components have been skipped for simplicity.

6.8.2 Software for the Power Supplies

The communication to the mobile power supplies was realized via an Ethernet connection, as that was the only and a simple way to address them, while also keeping them mobile. Each of the power supplies was equipped with a 50 m Ethernet cable which was connected to the COSY network. This way, one can use any computer connected to the network to send instructions to the power supplies and it does not depend on the computer running the software. Internally, at the power supplies themselves, the commands were passed through an Ethernet to serial connection conversion and then handled as serial commands. One can use SCPI³ commands to give instructions to the power supplies.

The code for communicating with the power supplies was implemented in Python. There were several parts that needed communication, the most important being the script that sends the instructions during the measurement to the power supplies. In addition, an Epics Input / Output Controller (IOC) was created for the power supplies to hold the information (currents, status of the output and relay, etc.) about them and pass them on to an archiver for later analysis. The IOC was populated by a python script fetching the current status from the power supplies and writing it into the variables of the IOC every half second.

The user interfaces used during the beam time can be seen in figure 6.17 and figure 6.18. In figure 6.17 one can see the display of all the variables of the power supplies stored in the IOC as a simple overview. In addition one could also see if some variables did not update recently by turning the text red, indicating a communication problem. In figure 6.18 one can see the interface of the measurement software. Here the selection of the quadrupole to be measured was done and settings for the measurement were set.

³ Standard Commands for Programmable Instruments

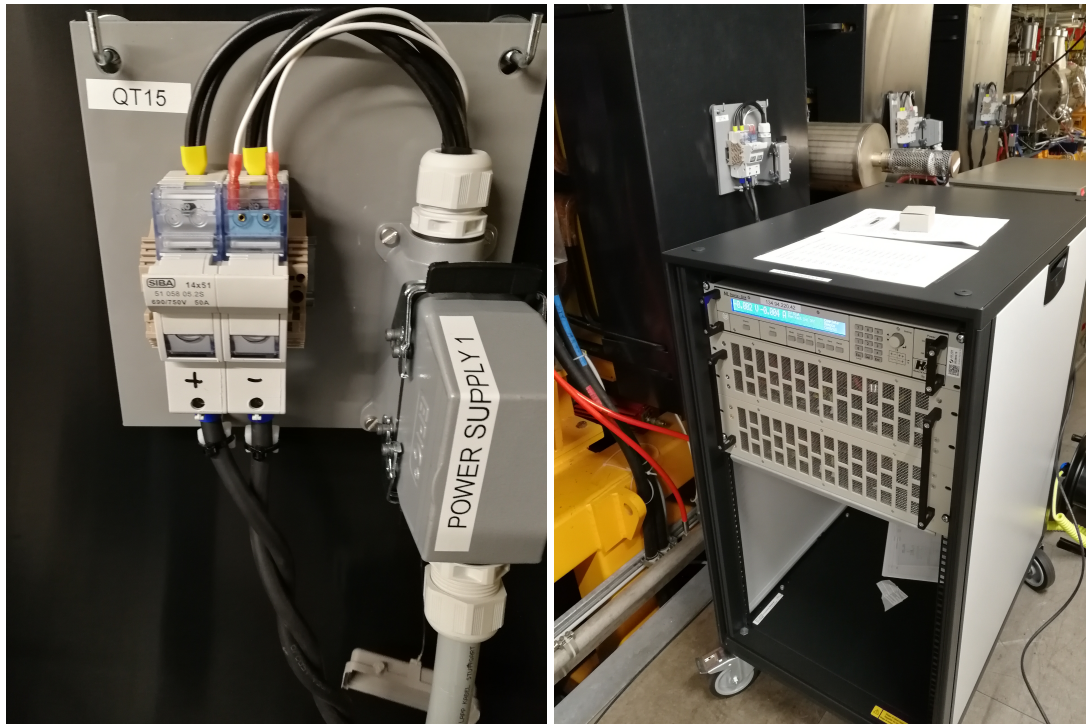


Figure 6.16: Picture of the additional power supplies connected in parallel to the quadrupoles to add or bypass some current. The first, left, picture shows the connector, which is labelled with the power supply number for easy identification, plugged into the socket at one magnet. It is connected via fuses to the quadrupole (here QT15). The black cables coming out of the socket carry the current and the white cables are used for the interlock. The cables coming out of the bottom of the fuses are going to the magnet. In the second, right, picture one can see the power supply mounted in the movable cabinet, while being connected to the quadrupole. The cabinet of the power supply is easily movable to quickly switch from one magnet to another. It is connected to regular 230 V power with a long extension cord and an Ethernet cable to the network.

6.8.3 Measurement Campaign

During the beam time, the measurement was performed in 84 second cycles during which the quadrupole strength was varied. After beam preparation the orbit was measured to get a reference. Then the beam was moved to the desired position for that cycle. Afterwards the quadrupole strength was varied as seen in figure 6.19. The quadrupole strength was changed by $\pm\Delta k$ with a reference point in the middle to correct any potential drifts of the orbit over the cycle. In the analysis it turned out that this reference point was actually not needed, as the orbit was very stable. For the measurement, hysteresis does not need to be considered, as the quadrupoles were always ramping in the same way and thus the measurement of one quadrupole always had the same hysteresis curve. In addition, even if the magnetic field of a quadrupole was not exactly symmetrically changed by Δk but slightly differently due to hysteresis, it will always be the same for all measured points. For the merit function (see equation (6.2)) one does not require a symmetric change of the quadrupole strength and thus a potentially asymmetric change of quadrupole strength does not impact the measurement.



Power Supply 1		Power Supply 2	
MEASCURRENT	-0.007 A	MEASCURRENT	-0.008 A
SETCURRENT	+0.000 A	SETCURRENT	+0.000 A
RELAIS	0	RELAIS	0
OUTPUT	0	OUTPUT	0
CONNECTEDTO	QT07	CONNECTEDTO	QT09
LOCATION	21m	LOCATION	27m
IP	134.94.220.42	IP	134.94.220.43
Power Supply 3		Power Supply 4	
MEASCURRENT	-0.001 A	MEASCURRENT	+0.001 A
SETCURRENT	+0.000 A	SETCURRENT	+0.000 A
RELAIS	0	RELAIS	0
OUTPUT	0	OUTPUT	0
CONNECTEDTO	QT27	CONNECTEDTO	QT29
LOCATION	122m	LOCATION	130m
IP	134.94.220.44	IP	134.94.220.45

Figure 6.17: Screenshot of the PV Display interface. It shows all the required PVs of the power supplies to be able to observe them easily during the measurement. The interesting ones during the measurement are the current it currently supplies and the state of the output and the relay, where a 0 indicates "off" and a 1 indicates "on". To which quadrupole the power supply is connected is also an important information. In addition the location in the COSY ring is given for the ease of finding it in COSY if something is not working.

At the start of the beam time only a subset of all quadrupoles was measured in order to roughly calibrate all of the BPMs. For that measurement two sets of 50 points for each of those quadrupoles has been measured. Then the optimal positions inside these quadrupoles were calculated and the BPMs calibrated appropriately. This was done to get the orbit close to the optimal point and then measure all of the quadrupoles, where then the expected optimum is around zero. The optimal position expected around zero permits to scan a not as big area for the beam positions and get a more precise measurement. Then for all of the quadrupoles, again, two sets of 50 measurement points each were measured to get the optimal beam position in all the quadrupoles. For some of the quadrupoles more than two sets of 50 measurement points have been taken if the preliminary analysis of the two already measured sets did not match quite well and more information was desired.

6.8.4 Analysis

The analysis of all quadrupoles follows the analysis from the February beam time closely, as the measurement principle is the same. The main difference is that the change of quadrupole strength is done with the external power supplies instead of the back-leg windings and thus is done in a more controlled way and is easier to access. In comparison to the measurement done with the back-leg windings the timing of the quadrupole strength changes is more precise, as it is directly controlled and not forwarded through the orbit correction software, where the change of quadrupole strength can be delayed by up to 2 s. The measured current of the external power supplies was recorded in EPICS and archived. With that, one can then determine when the

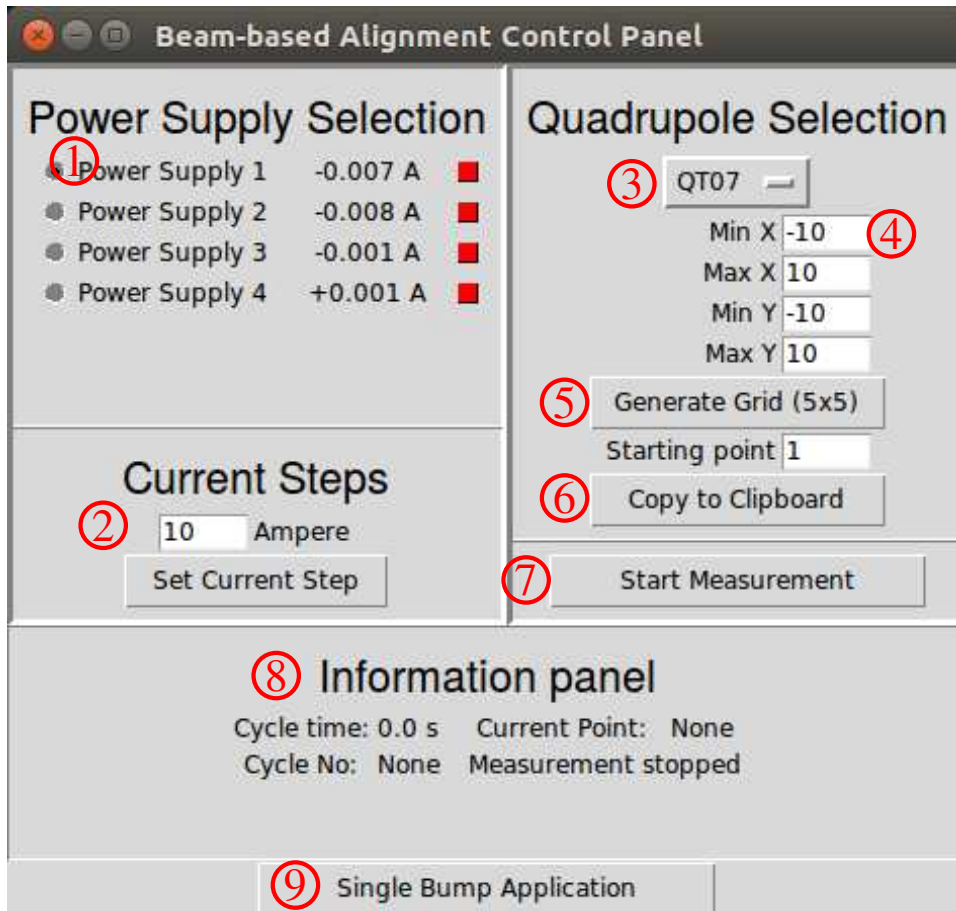


Figure 6.18: The interface for controlling the measurement consists out of several parts, which had to be operated in a certain order. At first the desired power supply used for the measurement had to be selected (1). There one can also see the currently measured current that the power supply gives and the state of the output and relay indicated by the LED. Afterwards, one has to decide on a step size of the current during the measurement (2). A typical value used for that was 10 A. Next, the quadrupole was selected (3), where the selection was only limited to the one connected quadrupole. Then the size of the orbit bump was set by giving the minimal and maximal values for the bump calculation in both horizontal and vertical direction (4). In order to find out which values are supposed to be entered there, one could manually apply bumps (9). When the decision was made how large the measurement area should be then the measurement grid can be generated (5) and the measurement can be started (7). If required, the measurement can also be interrupted with the same button (7) and it is possible to resume, if the starting point is set accordingly. In order to have a complete documentation of all information, the settings could be copied to the clipboard (6) and entered into a logbook entry. In the lower part of the interface (8) the status of the measurement is displayed. It gives the cycle time, currently measured point and counts the cycle numbers to be able to keep track of the measurement.

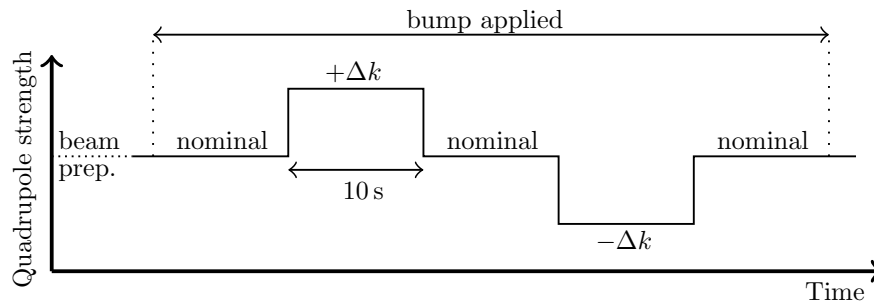


Figure 6.19: The measurement pattern used for the measurement of all the quadrupoles in September/October 2019. At first the beam is prepared, i.e. accelerated, bunched and positioned as desired with the use of an orbit bump. Then the quadrupole strength is left at the nominal strength to have a reference point to see if something changes during the measurement time due to outside effects. Next the quadrupole strength is increased by $+\Delta k$ and afterwards again set to nominal strength. Then the quadrupole strength is set to $-\Delta k$ and afterwards also set to nominal strength again. This is a complete pattern for one data point for the merit function.

quadrupole strength was changed by $\pm\Delta k$ and extract the corresponding orbit at that time point in the cycle. Afterwards the same computation as with the measurement with the back-leg windings was done to evaluate the merit function and perform a fit. One example of such a fit can be seen in figure 6.20, where the horizontal and vertical directions have already been converted into mm for the ease of reading, instead of leaving it as a script setting which was internally used.

As the bumps were applied by a script during the measurement and the set value of the script was recorded, the result of the paraboloid fit was in a script setting, which had to be linearly converted to a reading in mm of the two nearby BPMs. With that, one can interpolate into the quadrupole and get the optimal position of the beam inside the quadrupole. The interpolation also has to take steerers and the kick angle of them into account to correctly interpolate into the quadrupoles. For most of the quadrupoles there was no steerer between the next two BPMs. For the cases where there was one or more steerers between the BPMs next to the quadrupole, the kick angle of the steerer(s) for the optimal script setting has been calculated. This calculation of the kick angle is easily possible, as it is exactly known how the bump was calculated. With the known optimal beam path through the quadrupole defined by the measurement of the BPMs and the kick angle of the steerer(s), one can then solve the set of equations to get the optimal position inside the quadrupole. This set of equations in the case of one steerer is a quadratic one and thus yields two possible solutions, where one could be excluded due to the knowledge of the kick direction of the steerer. The calculation works similarly for the case with more than one steerer and also gives the optimal position inside the quadrupole.

Error Calculation

For each quadrupole there are two to four measured data points with each their individual error from the fit. Most of the time there are exactly two data points. For a final result for the quadrupole these have to be averaged, but they are spread by a random amount. When taking

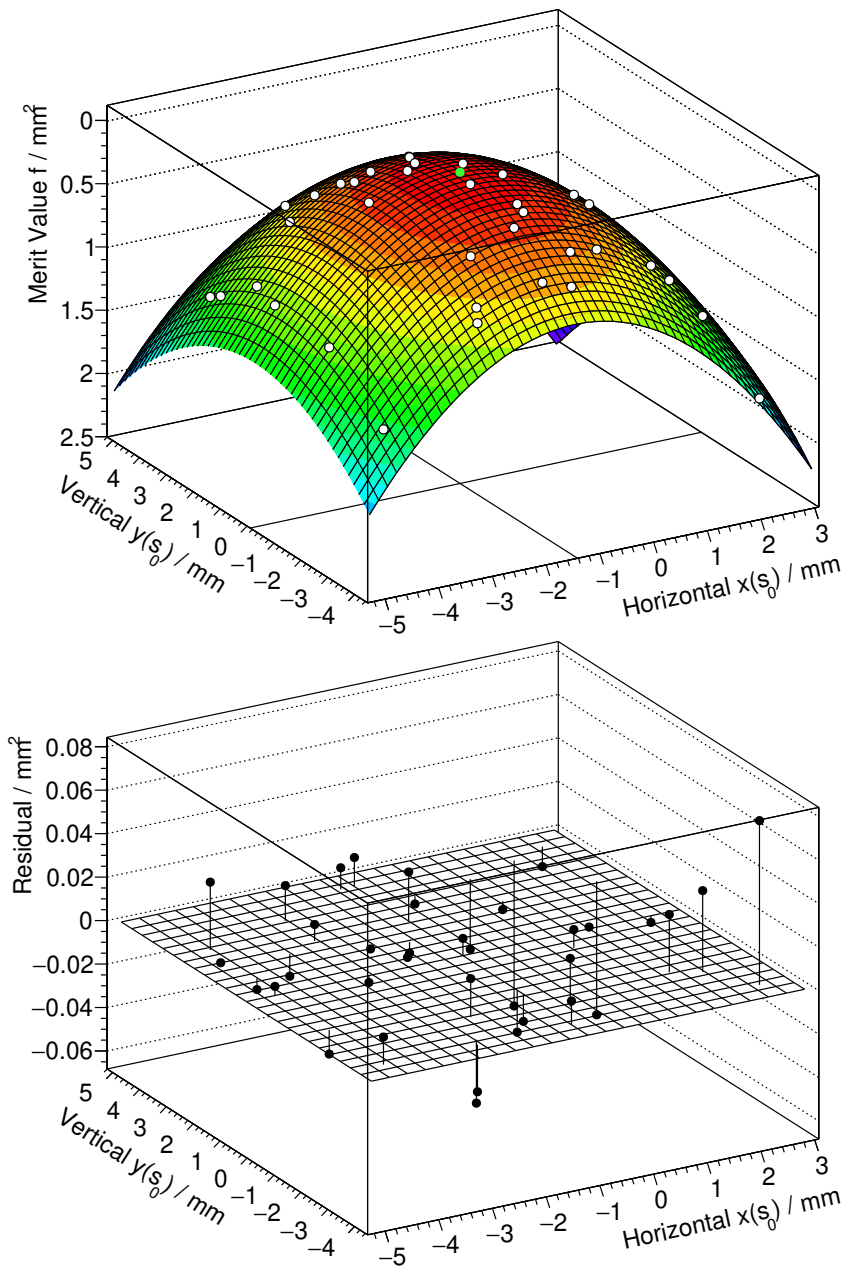


Figure 6.20: An example of a fit for the determination of the optimal position inside a quadrupole is shown. This example shows a measurement of QU17, which is located in one of the arcs. The white points are the data points, where on the x - and y -axis the horizontal and vertical displacements of the beam inside the quadrupole are shown, and on the z -axis the calculated merit function $f(x(s_0), y(s_0))$ is depicted. The displacement of the beam inside the quadrupole is obtained by extrapolation from BPMs up- and downstream of the quadrupole. The z -axis has been drawn upside down to make the minimum (highest point in the plot) easier to identify. The data points have a small error ($\approx 0.008 \text{ mm}^2$), which is not displayed here. The fit to the data is the colored paraboloid, where the green dot marks the minimum of the fit. In order to guide the eye where the minimum is two lines at the bottom of the plot have been added. The bottom plot depicts a residual plot. It shows the difference of the data points from the fit. Here one can see that for positive horizontal positions there seems to be more of a disagreement between the data and the fit. This figure has also been included in [56].

two data points and calculating the error of the average of these it is half of the spread of the data points. This does not make sense, as some data points are very close together by chance and thus would have a small error, whereas others are spread more apart and obtain a bigger error. Thus, all the data points have been taken into account for the error calculations. The distribution for the spread of the data points for all the quadrupoles has been calculated and can be seen in figure 6.21. There one can see that most of the data points are close together, except for some outliers. If one looks at that distribution, with only the quadrupoles with more than 2 data points, i.e. three or four, then it looks different (see figure 6.22). Here one can see a small tend to slightly higher values, as expected. With that, one can then estimate the error on the measurements in a better way. The median of that part of the distribution, while ignoring outliers above $200\ \mu\text{m}$, is $79\ \mu\text{m}$, which is approximately the average distance between the data points and half of that is the error for the average of two data points. Thus an error of $40\ \mu\text{m}$ has been assigned to all of the data points irrespective of their actual spread. The quadrupoles, where there are three or four measurements done are those where the first two measurements were not satisfyingly close together. Thus there is an inherent bias towards a higher spread when restricting to more than two measurements and also an inherent bias towards smaller spread when only two measurements were done. This then means that the error estimation of $40\ \mu\text{m}$ is a slight overestimation of the actual error, but anyways smaller than the absolute BPM resolution ($\approx 100\ \mu\text{m}$). In order to show that the value of $40\ \mu\text{m}$ fits for cases where there are multiple measured data points, an example for two quadrupoles is shown in figure 6.23.

BPM Offset Calibration

From the optimal positions inside the quadrupoles, one can compute the new BPM calibration such that the optimal position in the quadrupoles is close to zero. This was done in an iterative way, as a change in the BPM calibration changes the local coordinate system and thus the optimal position inside the quadrupole. The computation of the new BPM calibration uses the optimal position in the nearby quadrupoles and interpolates back into the BPM taking the two quadrupoles next to the BPM for that computation. In the straight sections one could in addition use more quadrupoles for the interpolation, as they are closely packed in sets of four quadrupoles with typically one BPM inside. With the knowledge of the new BPM calibration, one can then calculate the new optimal position inside the quadrupoles, which is expected to be at zero. An example how the optimization looks in the straight section can be seen in figure 6.24. A comparison between the optimal beam position inside the quadrupole before and after the BPM calibration can be seen in figure 6.25. The iterative procedure was chosen, as it also works if only a small section of the accelerator is optimized.

At a later time point the calculation of the BPM calibration has been repeated with the use of a matrix formalism and Singular Value Decomposition (SVD). This method gave the same result, but was faster and computationally more efficient, which at this point is not important, but it could be relevant for future applications.

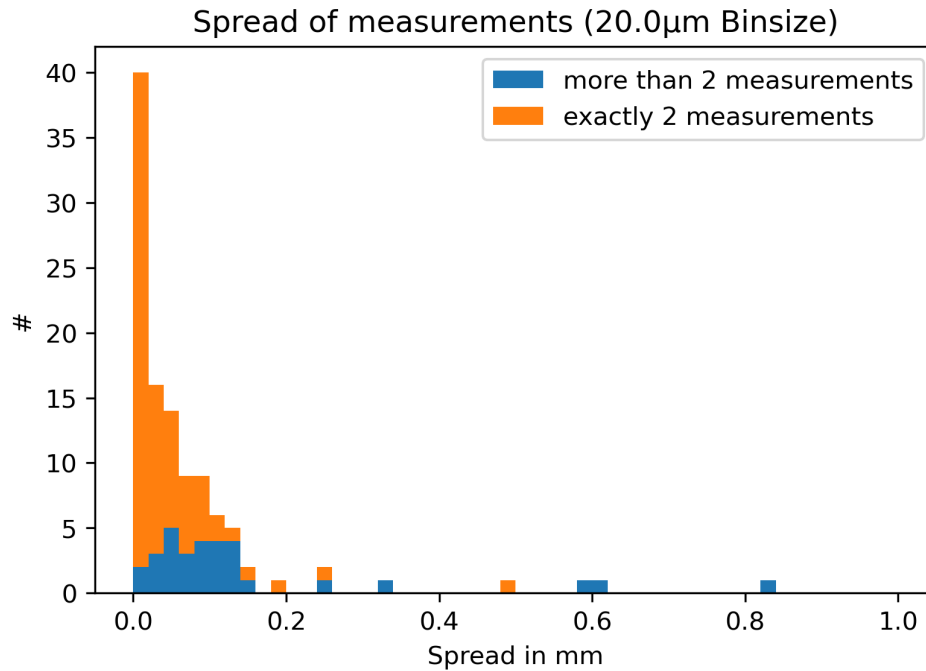


Figure 6.21: The spread of all measurements for all quadrupoles. The spread is defined as the maximal distance between all the measurements. For the cases where there are only two measurements, that is just the distance between the two measurements and for more than two measurements the maximal distance between all of the measurements was taken. One can see a high peak from $0\ \mu\text{m}$ to $20\ \mu\text{m}$ and then a quick drop off. The maximal spreads are around $150\ \mu\text{m}$, except for some outliers. For a closer look at the distribution with three or four measurements see figure 6.22.

6.8.5 Results

As a result, one gets a new calibration of the BPMs, which is shown and discussed in the next section. In addition, it was also noticed that for the calibration in the straight sections one had to exclude some of the quadrupoles from the sets of four quadrupoles, as the measurement of the optimal positions showed that they were not on one straight axis with the other quadrupoles in that set, although they are expected to be. This then lead to an investigation of those outliers and it was seen that they are indeed a little bit off. These details are discussed later in section 6.8.8.

6.8.6 Final Calibration of all BPMs

In figure 6.26 one can see the final calibration applied to the BPMs. The numbers are additionally listed in table A.1 in appendix A. This calibration has been obtained as explained in the analysis section before. In the figure one can see the measured position inside the BPM which should correspond to the zero position, thus that value has to be applied as a negative offset to the BPMs (compare to equations (5.1) and (5.2) in section 5.1). The deviation of the electrical zero of the BPMs and the actual zero for the orbit is up to 6 mm, which is a significant deviation when compared to the 0.2 mm alignment measurement of the magnets done by the company

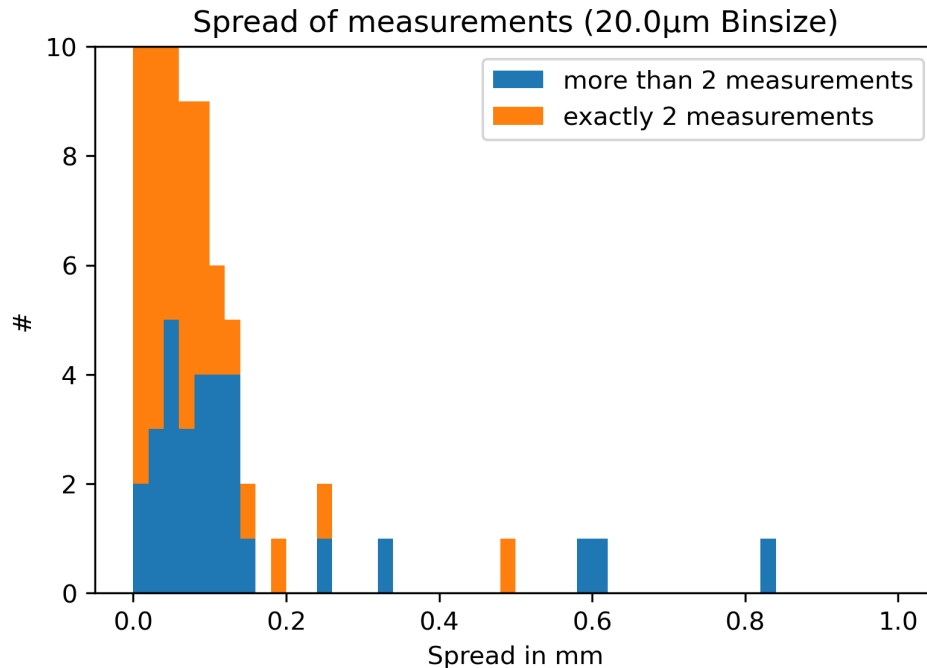


Figure 6.22: The figure shows a zoomed in version of figure 6.21. The median of the distribution of more than two measurements (ignoring outliers above $200\ \mu\text{m}$) is $79\ \mu\text{m}$. Half of that ($40\ \mu\text{m}$) was then chosen to be the error on the optimal positions of all the quadrupoles, as calculating an appropriate error with only few data points heavily depends on the spread of those.

Stollenwerk [57]. This clearly shows that this measurement was for sure required to correct for systematics effects, as a wrong beam position of that magnitude will lead to significantly different results in simulations.

6.8.7 Improvement of the Orbit

With the new BPM calibration one can also have a look at the orbit in the accelerator. As explained in section 4.4 one can use the orbit control software to correct the orbit to a desired position. By default that is the zero position, which is what is wanted most of the time. The orbit control software has been used to check by how much better the orbit in the machine is when using the new BPM offsets determined with the beam-based alignment. For that, the old BPM calibration was applied to the BPMs again and the orbit was corrected. Then the better BPM calibration, which was determined with the beam-based alignment, was applied to the BPMs and another orbit correction was performed. In between the two tests the orbit correction values of the steerers were reset, so that the same starting conditions could be used. In order to compare those orbits in a better way, the Root Mean Square (RMS) was calculated for both, horizontal and vertical directions. The resulting values can be seen in table 6.4. In addition, one can also see the RMS for the steerer strength used to achieve that orbit in the machine.

Out of table 6.4 one can see that for the orbit correction one needs significantly less steerer

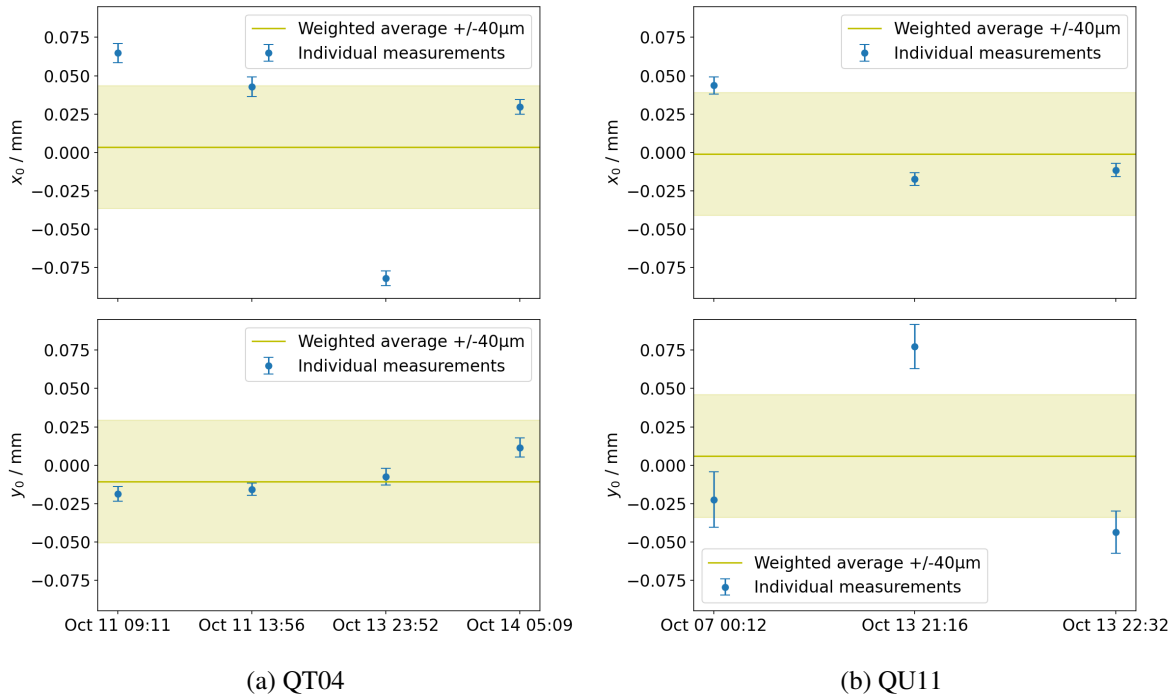


Figure 6.23: Spread of measured optimal positions inside quadrupole QT04 and QU11 respectively. The data points are the results from the individual fits with the errors obtained by the fitting procedure. On the x-axis the date and time of the measurement are shown. In addition the weighted average values of the individual measurements are shown as the horizontal yellow lines. The yellow shaded band around those has a size of $\pm 40 \mu\text{m}$, which is the error assigned to all average positions, as explained in the text. This figure has also been included in [56].

power for a similar correction, which is a measure by how much better the calibration is now. The necessary steerer power dropped by 80% for the vertical direction and by 20% for the horizontal direction. This is a very good improvement, as one does not need to use more steering strength to act against the quadrupoles if the beam passes the quadrupole off-center. Unfortunately, the performance of this test was not equally good for the horizontal and vertical direction. This is due to a constraint on the correction at the time of the measurement, as some horizontal steerers could not be varied and had to stay at fixed values. This then lead to the beam being offset by 10 mm horizontally in one straight section, which impacted the performance of the orbit correction.

6.8.8 Crosscheck of the Mechanical Alignment of the Quadrupoles

With the beam-based alignment measurement it was also possible to gain insight into the alignment of some of the quadrupoles. During the analysis it turned out that some of the quadrupoles in the straight section are not as well aligned as it was assumed. For the quadrupoles in the arcs it is not possible to make a statement with the beam-based alignment data for the alignment of the quadrupoles.

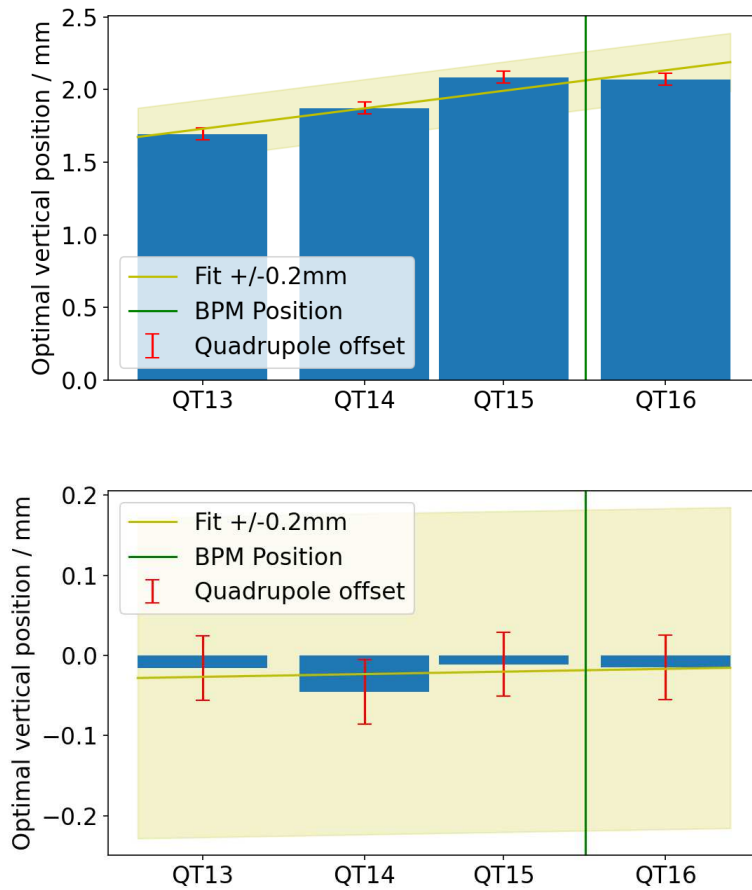


Figure 6.24: In order to calibrate a Beam Position Monitor (BPM) in the straight sections all four quadrupoles were used to calculate the BPM offset. The bars are the optimal positions in the quadrupoles, where one can fit a straight line (top plot). With that line one can then calculate the offset at the position of the BPM, which is the new BPM offset calibration. The optimal quadrupole position after the BPM offset calibration can be seen in the lower plot, where the optimal quadrupole positions are all close to zero. The shaded region around the fit is used to indicate the alignment precision that the company Stollenwerk achieved. For this specific set of quadrupoles it was better than 0.2 mm, but this is not the case for all of them. This figure has also been included in [56].

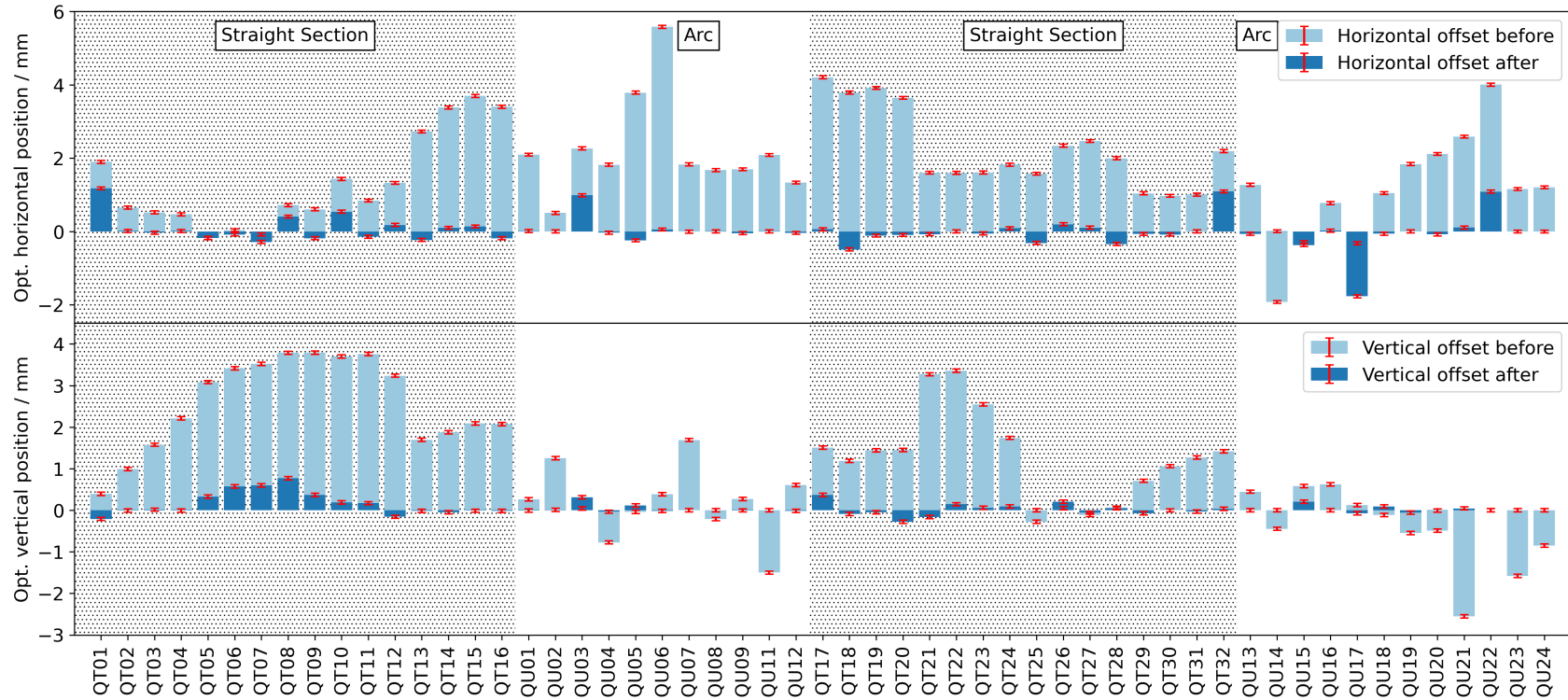


Figure 6.25: The optimal beam position in all quadrupoles. The top part of the plot shows the horizontal direction and the bottom part shows the vertical direction. The optimal position inside the quadrupole before the Beam Position Monitor (BPM) offset calibration can be seen in the light blue color and after the BPM offset calibration it is shown in the dark blue color. The error on the optimal positions is $40\ \mu\text{m}$ as indicated by the red error bars. The optimal positions before the offset calibration are not close to zero, which is corrected after the offset calibration, as the optimal positions have been pulled closer to zero. In the straight sections the quadrupoles labelled QT are close together in sets of four and are expected to be on the same axis, as they refer to the same BPMs. Thus one can fit a straight line through them to calibrate the BPMs there. For the arcs, where the quadrupoles are labeled with QU, this is not the case, as they are distributed more equally along the arc. After the offset calibration one can still see some patterns that deviate from zero, which correspond to individual quadrupoles that are off by up to 1.2 mm. In the straight sections one can compare that to the other three quadrupoles in the set and see a misalignment of the quadrupole. In the arcs the three deviating quadrupoles without a BPM close by and thus one can not pull them to the zero line. There it is not clear which quadrupole could be misaligned as a comparison is not possible and one has to trust in the mechanical alignment to be correct. This figure has also been included in [56].

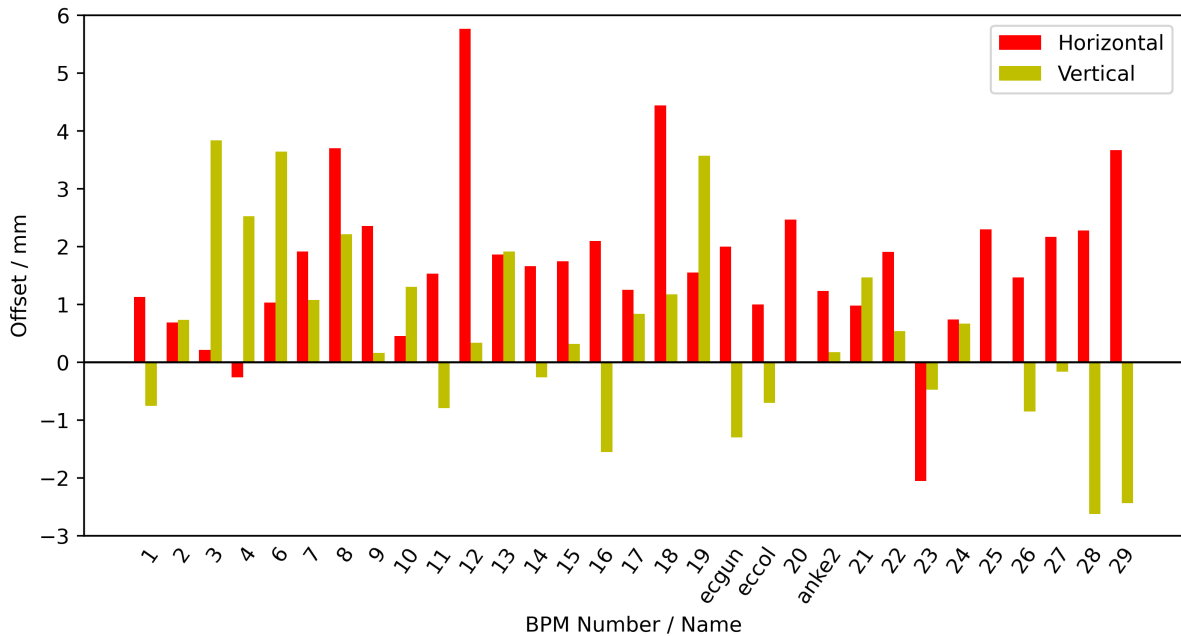


Figure 6.26: The new Beam Position Monitor (BPM) offset calibration calculated with the measurement of all quadrupoles. The horizontal offsets are shown in red and the vertical ones in yellow. On the horizontal axis the BPM name is displayed and on the vertical axis the corresponding offsets. Before the beam-based alignment was done, most of the offsets were zero and the BPMs were not properly calibrated. One sees that the BPMs are off by several mm with respect to the optimal beam axis given by the magnets, which are aligned with a precision of 0.2 mm. This figure has also been included in [56].

As the quadrupoles in the straight sections are located in sets of four quadrupoles close together, all having the same BPM close by, one can assume that they are all aligned to a straight line within the 0.2 mm specification given by the alignment campaign by the company Stollenwerk [57]. The data measured by the company Stollenwerk is given in table A.2 and table A.3 in appendix A. For some of the quadrupoles it turned out that the assumption, that they are all aligned that way, was not true and that those are off by up to 1.2 mm with respect to the other three in the set. Those have then been excluded for the calibration of the BPMs, as including them would make the optimization worse in the other three quadrupoles in the set. One example of that can be seen in figure 6.27. Independent of the beam-based alignment also the same quadrupoles have been identified as not perfectly aligned by Vera Poncza, by fitting the COSY model to measured data with the Linear Optics from Closed Orbit (LOCO) method [24].

Shortly after that has been discovered, a mechanical alignment measurement for specifically those quadrupoles has been done. Not only the measurement frame put on top of the quadrupoles has been measured again, but also the edges of the iron yoke to see if there is any discrepancy to the assumption that everything is aligned. For the measurement frame it turns out that it is aligned as expected, but the edges of the iron yokes of the quadrupoles are not

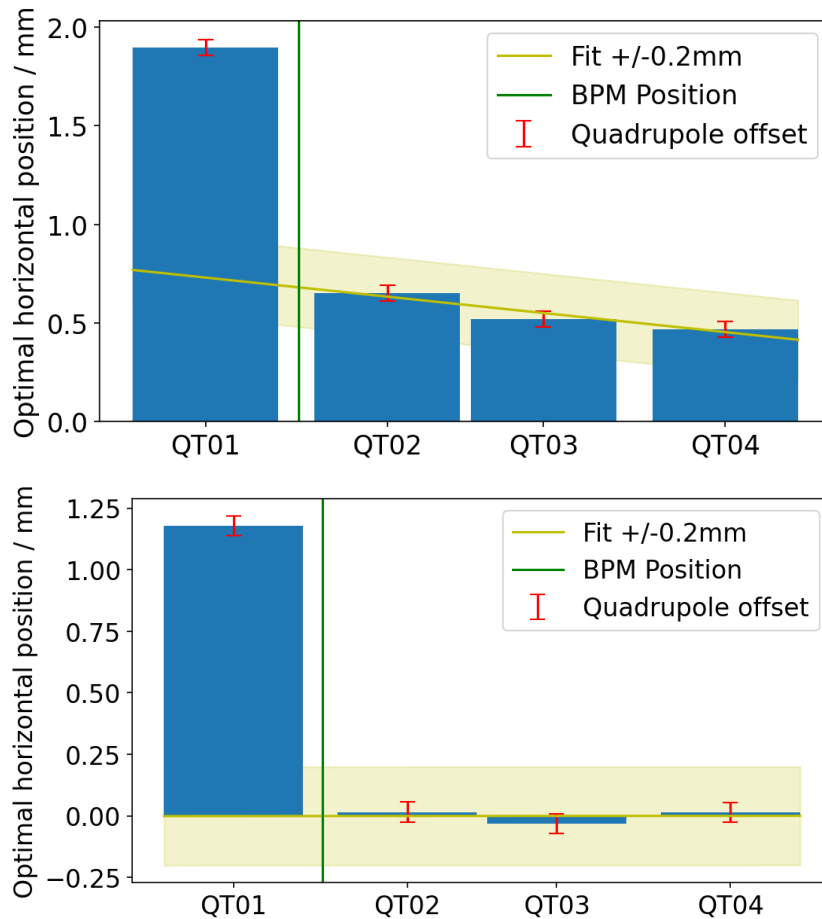


Figure 6.27: In order to calibrate a Beam Position Monitor (BPM) in the straight sections all four quadrupoles were used to calculate the BPM offset. For most of the sets of four quadrupoles that worked nicely, but there are some where that fails. One example of that is shown here, where it is obvious that the four quadrupoles are not aligned with respect to each other. The bars are the optimal positions in the quadrupoles, where one can fit a straight line (top plot). For that fit the quadrupole QT01 had to be excluded, as it is not well aligned. Then one can calculate the BPM calibration, like explained previously. The optimal quadrupole position after the BPM offset calibration can be seen in the lower plot, where the optimal quadrupole positions are close to zero with the exception of QT01. If QT01 would have been used for the calculation of the calibration, then the calibration would be way worse and the new optimal positions would not be close to zero. The shaded region around the fit is used to indicate the alignment precision that the company Stollenwerk achieved.

Table 6.4: Change of Steerer current RMS depending on the calibration of the Beam Position Monitors (BPMs) with similar corrected orbit RMS. Before the calibration with the obtained results, only known and deliberate shifts of BPMs were included, which was the case for 3 out of 31 BPMs. Afterwards, all of the BPMs were calibrated to show zero when the beam in centered in the nearby quadrupoles. The Orbit was corrected to minimal orbit RMS, where the goal was to reach a zero orbit, and the values for the corresponding steerer currents, which are given in a percentage of the maximal current, were recorded. Due to constraints during this test the performance of the horizontal direction was not as good as it could have been, as one straight section could not be corrected properly and was deviating by 10 mm from zero.

	Horizontal	
	Orbit RMS _x	Steerer RMS _x
Before calibration	2.27 mm	5.03 % / 0.63 mrad
After calibration	3.26 mm	3.90 % / 0.49 mrad
	Vertical	
	Orbit RMS _y	Steerer RMS _y
Before calibration	1.09 mm	4.39 % / 0.25 mrad
After calibration	0.52 mm	0.79 % / 0.05 mrad

aligned that precisely. This can be due to the fact that the measurement frame is positioned on top of the iron yoke in dedicated holders, which have been mounted yeas ago and some of them got loose and have been glued back on. There a small deviation in the position of that holders could have happened and thus the good alignment of the measurement frame does not equate to a good alignment of the magnet itself.

A comparison of the measured data for the edges of the iron yokes of the quadrupoles, which were found not to be aligned well with the beam-based alignment, has been done. The result of that is that the surveying of the edges of the iron yoke and the beam-based alignment measurement agree with each other about the alignment of the magnets, which are off by up to the above mentioned amount. This is mostly due to rotations, which are minimal on the top of the measurement frame, but due to the lever arm, towards the center of the magnet it leads to a deviation of the positioning.

Also a deviation of an other quadrupole could be seen with that alignment measurements of the iron yokes, which did not show up in the beam-based alignment measurement. There then the question emerged why it was not seen. After some analysis of the measured data, it turned out that there were two effects happening in parallel, a shift and a rotation. The shift and rotation combined were compensating for each other, so that the magnetic center of the quadrupole is actually not shifted, but still there is a tiny unwanted rotation of the magnet.

After discussing these observations, the decision was made to not change the positioning of the magnets for now, as most of them are well aligned and instead to wait for the next measurement by the company Stollenwerk and see what they report on the alignment.

6.9 Further Beam-based Alignment Measurements at COSY

With the finished beam-based alignment, there were some more ideas where this measurement procedure could help improving the accelerator COSY. One example is the alignment of other magnets in the accelerator. Such a measurement was done in early November 2020 for the Siberian Snake, a solenoid magnet. In previous measurement campaigns, the observation was made that the Siberian Snake was not perfectly on axis in the accelerator, as when turned on, it steers the beam, although it should not. The idea was to find out, how the magnet would be properly positioned by finding the beam path with no steering through the Siberian Snake and then rotate it accordingly.

For that measurement one had to first determine the optimal beam path through the quadrupoles up and downstream of the Siberian Snake to define the magnetic axis of COSY. In order to do that a small, manual, beam-based alignment measurement was performed to position the beam centered through the quadrupoles up and downstream of the Siberian Snake. The beam was moved, the quadrupole strength was varied and the beam position, where the influence on the orbit is minimal was found. This was done first using parallel shifts of the beam to optimally position the beam in one of the quadrupoles. The alignment in the second quadrupole was done by changing the angle of the beam passing through the first quadrupole, while keeping the position there fixed and aiming for the optimal position of the second quadrupole. After that the BPM readings were recorded, which were very close to zero and in agreement with the measurements from the beam-based alignment from September/October 2019, which was described in the previous section 6.8. When now turning on the Siberian Snake an orbit distortion could be observed, where the numbers for that are given in table 6.5. This distortion should be minimized by finding a better beam path through the Siberian Snake. Over several hours the beam was optimized inside the Siberian Snake by changing the angle and offset of the beam, when passing the Siberian Snake. One example of the observed changes by changing the orbit in the Siberian Snake can be seen in figure 6.28. The optimal beam path through the Siberian Snake was found and a significantly smaller orbit distortion was recorded. With that information the Siberian Snake was then rotated and shifted accordingly in the accelerator. The rotation in the horizontal plane was 0.1445° clockwise, when looking from above, and in the vertical direction it was 0.1051° counter-clockwise when looking from the inside of the ring. The shift was 1.385 mm towards the outside of the ring in the horizontal direction and 0.27 mm downwards in the vertical direction. Afterwards, the beam was put back on the magnetic axis of COSY, as found with the beam-based alignment, and a comparison measurement was done. These numbers are also given in table 6.5. This then showed that the Siberian Snake was now, after moving it, well aligned and the orbit distortions were minimized by a factor of 10.

Table 6.5: Measured orbit differences between two time-points in a cycle. The orbit was recorded at 30 s and at 80 s in the cycle and the Root Mean Square (RMS) of the difference of the two orbits has been computed. Between the two time-points the Siberian Snake has been ramped from 0 A (off) to 15 A (on). This then disturbed the orbit, which can be seen in a non-zero value of the orbit difference RMS. All the measurements have been done with the beam on the magnetic axis of COSY, which is defined by the quadrupoles up and downstream of the Siberian Snake. The alignment of the Snake was a success, as the orbit distortions have been reduced by a factor of 10 and are much closer to the values one gets with the Siberian Snake permanently off, given in the third row.

	Orbit Difference RMS	
	Horizontal	Vertical
With Siberian Snake before alignment	0.351 mm	0.337 mm
With Siberian Snake after alignment	0.037 mm	0.020 mm
Siberian Snake off, only COSY	0.022 mm	0.009 mm

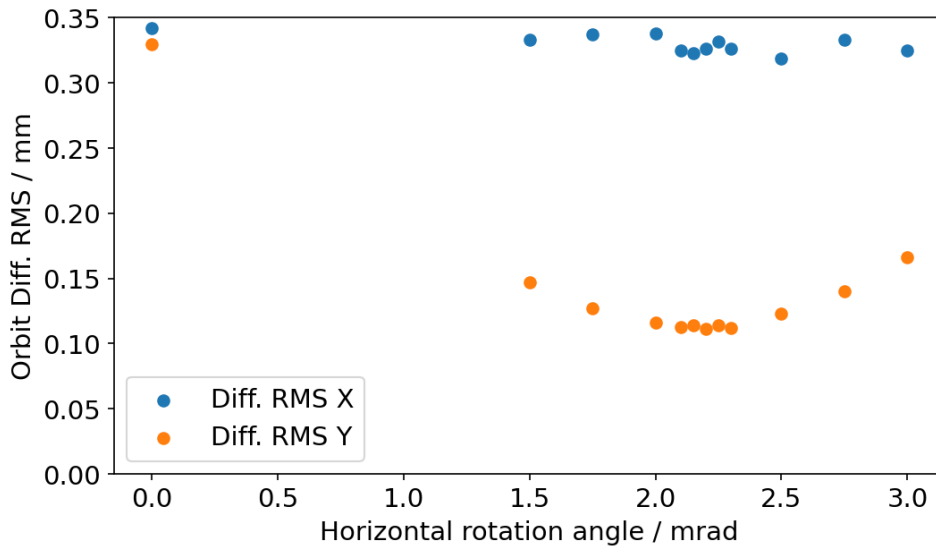


Figure 6.28: Changes in the orbit difference Root Mean Square (RMS) measurement depending on the horizontal beam rotation angle. The measurement pattern and calculation of the orbit difference RMS is explained in the caption of table 6.5. The change of the horizontal angle is done with respect to the initial orbit, which passes through the center of the quadrupoles up- and downstream of the Siberian Snake. One can see that the change of the angle in horizontal direction leads to a decrease of the vertical orbit difference RMS with a minimum around 2.2 mrad. From there on the optimization has been continued with alternating shifting and rotating the beam (not depicted). Also the beam has been rotated and shifted in vertical direction for an optimization of the horizontal orbit difference RMS (not depicted).

Outlook: Future EDM Ring Design

In this section a look will be taken at Beam Position Monitors (BPMs) and their alignment in other accelerators and how one can use the insight gained in this thesis, due to the beam-based alignment, to get a better idea on how to mount and position BPMs in the Final Ring for the Electric Dipole Moment (EDM) measurement.

7.1 BPMs and Alignment in other Accelerators

One example for a recently designed accelerator, which is now in the process of being built, is the High Energy Storage Ring (HESR) at the Facility for Antiproton and Ion Research (FAIR) in Darmstadt. This accelerator is designed with similar specifications as COSY, but with a higher maximum energy and is being constructed by IKP-4 of Forschungszentrum Jülich. A lot of the technology used at the HESR is being tested with the COSY BPMs, like the Libera Hadron system [58]. The design of the BPMs for the HESR is constrained by the other accelerator elements as the BPMs are partially inside some of the accelerator magnets [59]. Some designs for the BPMs have been looked at, comparing their functionality [60]. In the end the same design of the BPMs as in COSY has been chosen, as told in [60].

Next to picking the design of a BPM one also has to carefully consider the mechanical positioning of the BPM, but there is no information available for the HESR design. However for other accelerators that has been discussed [48, 49, 51, 61, 62] in more detail. Options to precisely mount and long-term monitor the positioning of a BPM are done with laser tracking and beam-based alignment. Future requirements on the precision and alignment of BPMs was also discussed in [63], where the difficulty of the alignment regarding thermal expansion of the materials has been investigated. As one can not stabilize the temperature to the level needed, one has to instead measure the effects precisely and correct for them. All these effects have to be kept in mind when deciding on the design and mounting of BPMs for future accelerators.

7.2 Prototype and All-electric Ring Design

The future development of the measurements of the Electric Dipole Moment (EDM) of charged particles by the Jülich Electric Dipole moment Investigations (JEDI) and Charged Particle Electric Dipole Moment (CPEDM) collaborations envisions a two staged approach. After the

currently running "Precursor Experiment" at COSY the measurements of the EDM will be continued with new accelerators. In order to prove that it is possible to build and operate an "All-electric Ring", first a "Prototype Ring" should be built to test and develop the needed expertise. More details of this process are discussed in [64]. Here, at first the design ideas for the Prototype Ring will be explained and then the plan for the All-electric Ring will be shortly discussed.

7.2.1 Prototype Ring

The design of the Prototype Ring is an ongoing process within the CPEDM collaboration. It should have a circumference of about 100 m and operate in two modes. The first mode should be operation with purely electric bending elements with a kinetic energy $T = 30$ MeV in order to prove the concept and also demonstrate the feasibility of operation with simultaneous counter-rotating beams. The second mode should operate with electric and magnetic bending in parallel with a kinetic energy $T = 45$ MeV, which due to the magnetic field excludes the simultaneous counter-rotating beams, but allows for freezing the spin of a proton beam, such that its projection into the horizontal plane stays aligned with the momentum of the beam. Also reversing the magnetic field should allow for alternating fills in opposing directions in order to cancel the average radial magnetic field, which is the leading cause of systematic error.

The Prototype Ring is foreseen to have a squared fourfold structure with 8 m long straight sections and 4 unit cells with a bending radius of 90° . Each bending section should consist of a QF-bend-QD-bend-QF, where the bending element has combined electric and magnetic bending. The combination of electric and magnetic bending requires a special geometry to match the fringe fields and no iron to easily reverse the magnetic field [64]. An illustration of the Prototype Ring is depicted in figure 7.1.

Simulations on the exact design specifications have been done in [66, 67]. Effects of different focusing configurations on the beam lifetime and particle losses have been investigated in [66]. Spin tracking simulations for the Prototype Ring have been done in [67].

7.2.2 All-electric Ring

In order to obtain the frozen spin condition with only electric bending elements one has to use protons with a kinetic energy $T = 232.8$ MeV. The frozen spin condition is not possible for deuterons without a magnetic field. Here, for protons, the operation of clockwise and counter-clockwise beams with frozen spin is now possible, as the bending happens only with electric elements. The design of such a ring has been initially proposed in [68] and more recently an evolved design has been published in [69]. The total length of the ring would be 500 m with 40 bending sections. In between the bending sections there are 36 straight sections of 2.7 m length for electrostatic quadrupoles and 4 straight sections of 20.8 m for polarimetry and beam injection.

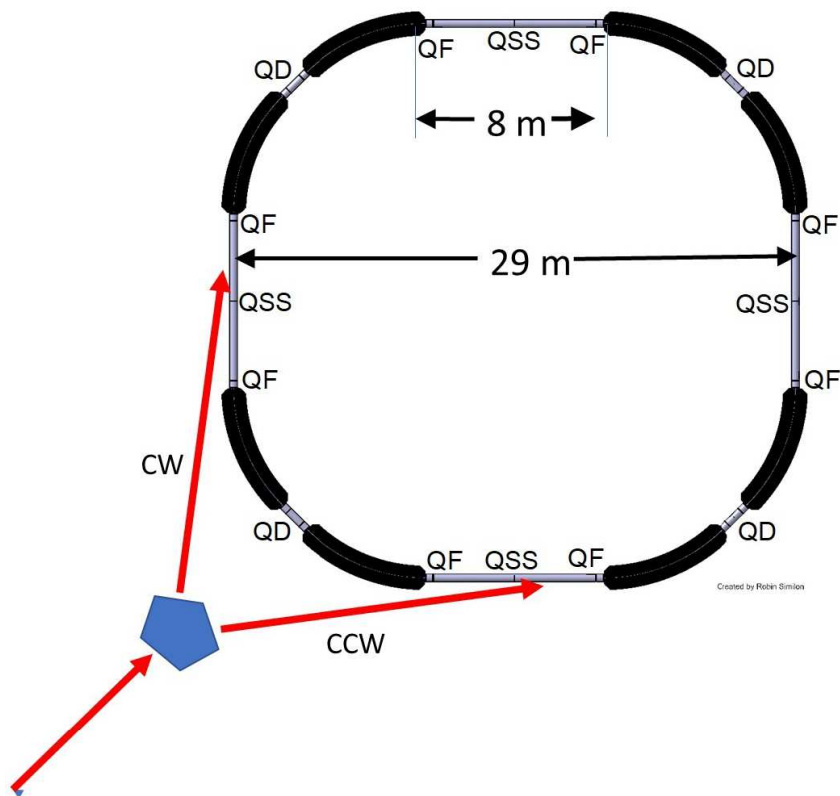


Figure 7.1: Depiction of the Prototype Ring with 8 bending elements, where electric and magnetic bending is superimposed. Quadrupoles are indicated with QF and QD for focusing and defocusing quadrupoles and QSS for straight section quadrupoles. The clockwise and counter-clockwise injection is depicted by arrows. Picture taken from [65].

7.3 Suggestions for the Ring Design

Knowing the beam position at as many positions in the accelerator is preferable, but one can not install BPMs at each element used in the accelerator due to space constraints. Thus one has to prioritize the elements, where the knowledge is most important. The first thing that is important is the knowledge of the beam position around the detector in order to properly position the beam and have a smooth extraction. Another important element are the quadrupoles or other higher order multi-poles, where one needs to know the beam position well, as one does not want to pick up additional field components, which add to systematics. An optimal design would have the BPM inside the center of the quadrupole, with the calibration such that the center of the BPM is exactly on the quadrupole center. There are some examples of BPMs used inside or partially inside magnets [59, 70, 71], but in general it is not favored to have a BPM inside a magnet, as that would mean one has to widen the gap for that magnet in order to accommodate the BPM. A good compromise is to have a BPM next to each quadrupole. This way one can make sure that the beam is centered in each of the quadrupoles. Another aspect that is very important is to be able to measure the BPM position accurately without beam operation. This is possible if one mounts fixed measurement markers to the BPM or, more precisely, to the

beam pipe which houses the BPM. For that, it has to be made sure that the BPM is not able to move in the beam pipe, which is usually the case. With that, one can then easily measure the BPM position and with appropriate calibration measurements done in the lab also determine the position of the electric center of the BPM. In addition, it is also possible to perform a beam-based alignment measurement to correct for potential mounting errors. This beam-based alignment measurement then does not need to be repeated to make sure that the BPM did not move if some changes were done in the vicinity of the BPM, which potentially moved it, as a position measurement with the measurement markers is possible and easier to perform.

One more idea is to affix the beam pipe and thus the BPM to the magnets and thus prevent movement of the BPM with respect to the magnets. This however then constrains the possibility of aligning the magnets with respect to each other, as the beam pipe would be affixed to each of them and if there are small differences, it is difficult to correct for them. Thus the idea of permanently mounting the BPMs to the magnets is not an optimal solution.

Another aspect one has to think about is the number of BPMs one wants to install in the accelerator. Regarding the optimal alignment of the beam inside all of the quadrupoles, it would be optimal to know the beam position in each quadrupole and thus install a BPM in or very close to each quadrupole. With such a high number of BPMs one has to consider, that one is most likely not able to perfectly correct the beam through all quadrupoles, if the quadrupoles themselves are not aligned perfectly. For that, one also has to increase the number of steerers, which can be used for correcting the beam path. This number of steerers has to be similar to the number of BPMs in order to try to correct the beam through all the BPMs. If the number of steerers is lower than the number of BPMs, then one can only get a solution which approaches a good solution, as the orbit can not be perfectly adjusted everywhere. In addition, if one includes one BPM for each quadrupole, then either it has to be mounted inside the quadrupole, which in return makes the aperture of the magnet larger, or the BPM has to be mounted close to the quadrupole, which will potentially lead to space constraints.

In the end, one has to find a compromise between the number of BPMs chosen and the required space for them in the accelerator. One way to alleviate the space constraints is to choose a small form-factor BPM to be used in the accelerator. An example for that would be Rogowski coil based BPMs [41], which are significantly shorter than common BPMs used e.g. in COSY. These Rogowski coil BPMs are already used in COSY around the RF Wien filter, where there is no space to mount regular BPMs, but the knowledge of the beam position is required.

An important part that should be considered when building an accelerator should be to make the beam-based alignment an easy process. This is important, as most likely the exact positioning of the BPMs is not easily measurable with respect to the magnetic field of the quadrupoles and thus a beam-based alignment measurement is required. It can be made easier by making it possible to quickly vary the current through an individual quadrupole. This can be either done by having a single power supply per quadrupole or directly incorporating a method to bypass some current into the design of the quadrupole with the use of an active or passive shunt.

One can also think about an active beam-based alignment technique, where one does not only measure the alignment of the BPMs with respect to the quadrupoles once with beam-based alignment, but does it continuously during operation. With a suitable way to integrate it into the machine operation at a regular interval, e.g. at the end of each cycle, one could reach a more precise alignment. This would then also correct for the time drift of the measure-

ments, as it is continuously corrected for. It could then allow to improve the precision of the beam-based alignment measurement from currently $40\ \mu\text{m}$, which originates from fluctuations between measurements with a gap of time of a several hours in between, to $\approx 10\ \mu\text{m}$, which is the precision of a single measurement. Also, drifts of elements in this order of magnitude are anyways expected due to temperature changes.

Summary and Conclusion

Within this thesis, the alignment of the Beam Position Monitors (BPMs) in the Cooler Synchrotron (COSY) with the beam-based alignment technique has been performed. It was possible to determine the center of the quadrupoles of COSY with a precision of $40\ \mu\text{m}$ and then calibrate the BPMs accordingly.

In chapters 1 to 4 the motivation and the theory required for this thesis have been discussed. For the process of the beam-based alignment several developments at COSY were made, which for example include the electronic calibration of the BPMs, which is discussed in chapter 5 and the development of a measurement procedure for the beam-based alignment, which is included in chapter 6. The results of the beam-based alignment measurement are an important ingredient for spin tracking simulations to further improve the COSY model and to finally understand the systematic errors of the Electric Dipole Moment (EDM) measurement at COSY. The BPMs were calibrated such that the quadrupoles are now located at or close to the zero line of the coordinate system spanned by the BPMs. This enables the correction of the orbit in COSY such that the beam passes very close to the center of the quadrupoles, which results in less steering power needed, as one does not have to steer against being offset inside the quadrupoles. As the quadrupoles in COSY are only aligned with a precision of $200\ \mu\text{m}$ some steering power will always be required. The precision of the beam-based alignment of $40\ \mu\text{m}$ could be further improved, as this limit originates from fluctuations between measurements with a gap of time of several hours in between. Also drifts of elements in this order of magnitude are expected e.g. due to temperature changes. Running an active feedback system with a continuously monitored alignment of the elements could allow one to reach the precision of a single measurement of $\approx 10\ \mu\text{m}$.

In addition to the calibration of the BPMs, mechanical misalignments of some quadrupoles have been observed, which were not visible with the regularly performed alignment campaign. These misalignments were confirmed by a laser tracking measurement and will eventually be corrected during the next alignment campaign of the magnets to improve the accelerator further. Another small aspect, which was only possible due to the beam-based alignment, was the alignment of the Siberian Snake, a solenoid magnet, to prevent orbit distortions between turned on and turned off state. Further suggestions to keep in mind when designing future accelerators have been made in chapter 7, which include, but are not limited to, to incorporate the easy possibility of beam-based alignment into the design of an accelerator by enabling the current through individual quadrupoles to be easily varied.

Next steps for the improvement of the beam-based alignment at COSY would be to build an

active feedback system for an automated and continuous beam-based alignment for a higher precision and correction for long-term drifts.

Appendix A

A.1 BPM Calibration

The calibration numbers for the Beam Position Monitors (BPMs) are given in table A.1.

A.2 Mechanical Alignment Data of the Quadrupoles

This section contains two tables (A.2 and A.3) listing the values for the mechanical alignment of the quadrupoles. The goal for the mechanical alignment of the quadrupoles was to align them better than 0.2 mm in transverse (x) direction, better than 0.5 mm in height (y) and better than 1 mm in beam (z) direction. This alignment goal was achieved for most of the quadrupoles. The quadrupoles, which are significantly off in beam direction, e.g. QU23, could not be adjusted further due to nearby installations of other accelerator equipment. The alignment survey by Vermessungsbüro Stollenwerk & Burghof has been first started in 2016 and in the following years remeasured and readjusted as needed. The data shown in the tables are from 2019.

The measurement is based on measurement-frames, which are mounted on top of markers on the quadrupoles. When those markers were mounted they were measured relative to the field of the quadrupole, thus the alignment of the magnets is the alignment of the magnetic centers and not the mechanical centers of the quadrupoles.

Table A.1: Numbers for the offset of all Beam Position Monitors (BPMs) in COSY. The values given are the position, which the BPM measures, when no offset is applied to it and the beam is centered in the nearby quadrupoles. For the calibration of the Libera Hadron System, the numbers have to be entered with a negative sign when a zero should be read at that position, as it adds the implemented offsets. These numbers can be used to reproduce figure 6.26 with the exception of BPM 25, where a known mechanical offset of -22.5 mm, which is due to its vicinity to the extraction, has been subtracted for the depiction in that figure. For the two electron cooler BPMs (ecolgun and ecolcol) the numbers are given with a lower precision, as there the determination was not as precise due to a longer distance to nearby quadrupoles. There is no number given for the vertical direction for BPM 25, as this part of the BPM does not exist.

BPM Name	Horizontal Offset	Vertical Offset
1	1.127 mm	-0.754 mm
2	0.690 mm	0.736 mm
3	0.213 mm	3.839 mm
4	-0.259 mm	2.526 mm
6	1.033 mm	3.642 mm
7	1.915 mm	1.077 mm
8	3.699 mm	2.217 mm
9	2.357 mm	0.165 mm
10	0.457 mm	1.303 mm
11	1.532 mm	-0.795 mm
12	5.764 mm	0.337 mm
13	1.865 mm	1.914 mm
14	1.662 mm	-0.258 mm
15	1.750 mm	0.320 mm
16	2.096 mm	-1.555 mm
17	1.254 mm	0.837 mm
18	4.444 mm	1.178 mm
19	1.551 mm	3.570 mm
ecolgun	2.0 mm	-1.3 mm
ecolcol	1.0 mm	-0.7 mm
20	2.470 mm	0.016 mm
anke2	1.233 mm	0.175 mm
21	0.982 mm	1.468 mm
22	1.907 mm	0.540 mm
23	-2.050 mm	-0.477 mm
24	0.738 mm	0.667 mm
25	-20.203 mm	—
26	1.468 mm	-0.849 mm
27	2.170 mm	-0.161 mm
28	2.282 mm	-2.622 mm
29	3.671 mm	-2.435 mm

Table A.2: Mechanical alignment of COSY quadrupoles in the straight sections relative to design specifications. Δz is along beam direction and Δx and Δy are horizontally and vertically, respectively. The mean error on those measurements is 0.06 mm. The additional separation in the table indicates the sets of quadrupoles which are located close together. The alignment and measurement of the data has been performed by Vermessungsbüro Stollenwerk & Burghof.

Element	Translation [mm]		
	Δz	Δx	Δy
QT01	-1.21	0.02	-0.37
QT02	0.42	0.01	-0.11
QT03	-0.46	0.02	-0.18
QT04	3.43	0.07	-0.34
QT05	0.39	-0.04	-0.06
QT06	-0.73	-0.06	-0.07
QT07	-0.14	-0.07	-0.03
QT08	-0.62	-0.08	0.98
QT09	-0.33	0.03	0.06
QT10	-0.13	-0.19	0.15
QT11	-0.43	-0.07	-0.10
QT12	-0.45	-0.03	0.09
QT13	-0.34	0.08	0.21
QT14	-0.07	-0.18	0.18
QT15	-0.25	-0.22	0.16
QT16	-0.33	-0.09	0.01
QT17	0.11	-0.13	0.56
QT18	0.08	-0.26	-0.28
QT19	0.13	-0.12	0.34
QT20	-0.92	-0.23	0.24
QT21	2.72	-0.31	0.35
QT22	0.76	-0.39	0.10
QT23	0.60	-0.21	0.02
QT24	0.75	-0.27	0.12
QT25	0.45	-0.28	0.04
QT26	0.51	-0.30	0.86
QT27	0.59	-0.30	-0.11
QT28	0.70	-0.19	-0.04
QT29	1.78	-0.16	-0.12
QT30	0.32	0.15	0.13
QT31	0.50	0.05	0.23
QT32	0.43	-0.24	0.16

Table A.3: Mechanical alignment of COSY quadrupoles in the arcs relative to design specifications. Δz is along beam direction and Δx and Δy are horizontally and vertically, respectively. The mean error on those measurements is 0.06 mm. The alignment and measurement of the data has been performed by Vermessungsbüro Stollenwerk & Burghof.

Element	Translation [mm]		
	Δz	Δx	Δy
QU01	-0.69	-0.14	-0.10
QU02	0.13	-0.06	-0.22
QU03	0.22	0.04	-0.37
QU04	0.68	0.04	-0.40
QU05	-0.20	-0.02	-0.39
QU06	-0.91	-0.07	-0.37
QU07	-0.12	0.12	-0.24
QU08	0.06	0.23	-0.93
QU09	-0.18	0.21	-0.25
QU10	-5.22	0.25	-0.38
QU11	0.29	-0.15	-0.06
QU12	0.43	-0.22	0.10
QU13	-0.18	-0.05	0.11
QU14	0.47	-0.14	-0.13
QU15	0.08	-0.02	-0.15
QU16	-0.12	-0.02	-0.06
QU17	0.06	-0.02	-0.07
QU18	0.03	-0.04	-0.17
QU19	0.28	0.14	-0.20
QU20	0.49	0.11	-0.26
QU21	0.32	0.09	-0.46
QU22	-9.78	0.11	-0.47
QU23	16.82	-0.22	-0.32
QU24	-0.95	-0.07	-0.27

APPENDIX A

Bibliography

- [1] N. Aghanim et al. “Planck 2018 results. VI. Cosmological parameters”. In: *Astron. Astrophys.* 641 (2020), A6. doi: 10.1051/0004-6361/201833910. arXiv: 1807.06209 [astro-ph.CO].
- [2] Werner Bernreuther. “CP violation and baryogenesis”. In: *Lect. Notes Phys.* 591 (2002), pp. 237–293. arXiv: hep-ph/0205279.
- [3] Andrei D Sakharov. “Violation of CP invariance, C asymmetry, and baryon asymmetry of the universe”. In: *Soviet Physics Uspekhi* 34.5 (May 1991), pp. 392–393. doi: 10.1070/pu1991v034n05abeh002497.
- [4] C. S. Wu et al. “Experimental Test of Parity Conservation in Beta Decay”. In: *Phys. Rev.* 105 (4 Feb. 1957), pp. 1413–1415. doi: 10.1103/PhysRev.105.1413. URL: <https://link.aps.org/doi/10.1103/PhysRev.105.1413>.
- [5] A. Angelopoulos et al. “First direct observation of time-reversal non-invariance in the neutral-kaon system”. In: *Physics Letters B* 444.1 (1998), pp. 43–51. ISSN: 0370-2693. doi: [https://doi.org/10.1016/S0370-2693\(98\)01356-2](https://doi.org/10.1016/S0370-2693(98)01356-2). URL: <http://www.sciencedirect.com/science/article/pii/S0370269398013562>.
- [6] Julian Schwinger. “The Theory of Quantized Fields. I”. In: *Phys. Rev.* 82 (6 June 1951), pp. 914–927. doi: 10.1103/PhysRev.82.914. URL: <https://link.aps.org/doi/10.1103/PhysRev.82.914>.
- [7] J. H. Christenson et al. “Evidence for the 2π Decay of the K_2^0 Meson”. In: *Phys. Rev. Lett.* 13 (4 July 1964), pp. 138–140. doi: 10.1103/PhysRevLett.13.138. URL: <https://link.aps.org/doi/10.1103/PhysRevLett.13.138>.
- [8] Makoto Kobayashi and Toshihide Maskawa. “CP-Violation in the Renormalizable Theory of Weak Interaction”. In: *Progress of Theoretical Physics* 49.2 (Feb. 1973), pp. 652–657. ISSN: 0033-068X. doi: 10.1143/PTP.49.652. eprint: <https://academic.oup.com/ptp/article-pdf/49/2/652/5257692/49-2-652.pdf>. URL: <https://doi.org/10.1143/PTP.49.652>.
- [9] N. F. Ramsey and A. Weis. “Suche nach permanenten elektrischen Dipolmomenten: ein Test der Zeitumkehrinvarianz”. In: *Physikalische Blätter* 52.9 (1996), pp. 859–863. doi: 10.1002/phbl.19960520906. eprint: <https://onlinelibrary.wiley.com/doi/pdf/10.1002/phbl.19960520906>. URL: <https://onlinelibrary.wiley.com/doi/abs/10.1002/phbl.19960520906>.

- [10] V. Andreev et al. “Improved limit on the electric dipole moment of the electron”. In: *Nature* 562.7727 (2018), pp. 355–360. doi: 10.1038/s41586-018-0599-8.
- [11] G.W. Bennett et al. “An Improved Limit on the Muon Electric Dipole Moment”. In: *Phys. Rev. D* 80 (2009), p. 052008. doi: 10.1103/PhysRevD.80.052008. arXiv: 0811.1207 [hep-ex].
- [12] C. Abel et al. “Measurement of the permanent electric dipole moment of the neutron”. In: *Phys. Rev. Lett.* 124.8 (2020), p. 081803. doi: 10.1103/PhysRevLett.124.081803. arXiv: 2001.11966 [hep-ex].
- [13] B.K. Sahoo. “Improved limits on the hadronic and semihadronic CP violating parameters and role of a dark force carrier in the electric dipole moment of ^{199}Hg ”. In: *Phys. Rev. D* 95.1 (2017), p. 013002. doi: 10.1103/PhysRevD.95.013002. arXiv: 1612.09371 [hep-ph].
- [14] M. Tanabashi et al. “Review of Particle Physics”. In: *Phys. Rev. D* 98 (3 Aug. 2018), p. 030001. doi: 10.1103/PhysRevD.98.030001. URL: <https://link.aps.org/doi/10.1103/PhysRevD.98.030001>.
- [15] J. Pretz. “Measurement of permanent electric dipole moments of charged hadrons in storage rings”. In: *Hyperfine Interact* 214 (2013), 111–117. doi: 10.1007/s10751-013-0799-4.
- [16] W. Dekens et al. “Unraveling models of CP violation through electric dipole moments of light nuclei”. In: *JHEP* 07 (2014), p. 069. doi: 10.1007/JHEP07(2014)069. arXiv: 1404.6082 [hep-ph].
- [17] Takeshi Fukuyama. “Searching for New Physics beyond the Standard Model in Electric Dipole Moment”. In: *Int. J. Mod. Phys. A* 27 (2012), p. 1230015. doi: 10.1142/S0217751X12300153. arXiv: 1201.4252 [hep-ph].
- [18] Abel, C. et al. “nEDM experiment at PSI: Data-taking strategy and sensitivity of the dataset”. In: *EPJ Web Conf.* 219 (2019), p. 02001. doi: 10.1051/epjconf/201921902001. URL: <https://doi.org/10.1051/epjconf/201921902001>.
- [19] F.J.M. Farley et al. “A New method of measuring electric dipole moments in storage rings”. In: *Phys. Rev. Lett.* 93 (2004), p. 052001. doi: 10.1103/PhysRevLett.93.052001. arXiv: hep-ex/0307006.
- [20] J. Slim et al. “Electromagnetic Simulation and Design of a Novel Waveguide RF Wien Filter for Electric Dipole Moment Measurements of Protons and Deuterons”. In: *Nucl. Instrum. Meth. A* 828 (2016), pp. 116–124. doi: 10.1016/j.nima.2016.05.012. arXiv: 1603.01567 [physics.ins-det].
- [21] Jamal Slim. “First commissioning results of the waveguide RF Wien filter”. In: *Hyperfine Interact.* 240.1 (2019), p. 7. doi: 10.1007/s10751-018-1547-6.
- [22] Paolo Lenisa and Frank Rathmann. “COSY Prepares the First Measurement of the Deuteron Electric Dipole Moment”. In: *Nucl. Phys. News* 27.3 (2017), pp. 10–13. doi: 10.1080/10619127.2017.1317175.

-
- [23] Vera Poncza and Andreas Lehrach. “Search for Electric Dipole Moments at Cosy in Jülich - Spin-Tracking Simulations Using Bmad”. In: *10th International Particle Accelerator Conference*. 2019, MOPTS028. doi: 10.18429/JACoW-IPAC2019-MOPTS028.
- [24] Vera Poncza. “Extensive Optimization of a Simulation Model for the Electric Dipole Moment Measurement at the Cooler Synchrotron COSY”. to be published. PhD thesis. RWTH Aachen University, 2020.
- [25] Helmut Wiedemann. *Particle Accelerator Physics*. Graduate Texts in Physics. Berlin, Germany: Springer, 2015. ISBN: 978-3-319-18316-9, 978-3-319-18317-6. doi: 10.1007/978-3-319-18317-6.
- [26] B.J. Holzer. “Lattice Design in High-energy Particle Accelerators”. In: *CERN Accelerator School: Advanced Accelerator Physics Course*. 2014, pp. 61–100. doi: 10.5170/CERN-2014-009.61. arXiv: 1601.04913 [physics.acc-ph].
- [27] B. Autin. “DISPERSION SUPPRESSION WITH MISSING MAGNETS IN A FODO STRUCTURE - APPLICATION TO THE CERN ANTI-PROTON ACCUMULATOR.” In: *IEEE Trans. Nucl. Sci.* 26 (1979), pp. 3493–3495. doi: 10.1109/TNS.1979.4330077.
- [28] K. Steffen. “PERIODIC DISPERSION SUPPRESSORS. 2.” In: *DESY-HERA-83-02* (Jan. 1983).
- [29] H. Stein et al. “Current Status of the COSY Electron Cooler (Jülich, Germany)”. In: *Atomic Energy* 94.1 (Jan. 2003), pp. 24–26. ISSN: 1573-8205. doi: 10.1023/A:1023486402224.
- [30] Beñat Alberdi Esuain. “Optimization of Injection in COSY”. MA thesis. RWTH Aachen University, Oct. 2019.
- [31] H. Stockhorst et al. “Progress and Development at the Cooler Synchrotron COSY”. In: *EPAC 2002 Proceedings* (2002).
- [32] R. Maier et al. “Cooler synchrotron COSY”. In: *Nuclear Physics A* 626.1 (1997). Proceedings of the Third International Conference on Nuclear Physics at Storage Rings, pp. 395–403. ISSN: 0375-9474. doi: 10.1016/S0375-9474(97)00562-9.
- [33] U. Bechstedt et al. “Field Measurement of the Magnets for COSY - Jülich”. In: *EPAC 1992 Proceedings* (1992).
- [34] Vsevolod Kamerzhiev et al. “2MeV Electron Cooler for COSY and HESR – First Results”. In: *5th International Particle Accelerator Conference*. July 2014, MOPRI070. doi: 10.18429/JACoW-IPAC2014-MOPRI070.
- [35] W. Derissen et al. “Technical features and final electron beam tests of the COSY electron cooler and first proton beam cooling”. In: *Workshop on Beam Cooling and Related Topics*. 1993, pp. 317–321.
- [36] O. Javakhishvili, I. Keshelashvili and D. Mchedlishvili. “A storage ring EDM polarimeter”. In: *J. Phys. Conf. Ser.* 1561.1 (2020), p. 012011. doi: 10.1088/1742-6596/1561/1/012011.

- [37] *COSY Parameterliste*. URL: <http://www.ikp.fz-juelich.de/cosy/cosyParameter.pdf>.
- [38] R. Maier et al. “Non-beam disturbing diagnostics at COSY-Jülich”. In: *EPAC 90* (1990), pp. 800–802. DOI: 10.1023/A:1023486402224.
- [39] Vladimir Reva et al. “COSY 2 MeV Cooler: Design, Diagnostic and Commissioning”. In: *5th International Particle Accelerator Conference*. July 2014, MOPRI075. DOI: 10.18429/JACoW-IPAC2014-MOPRI075.
- [40] Fabian Hinder et al. “Development of New Beam Position Monitors at COSY”. In: *4th International Beam Instrumentation Conference*. 2016, TUPB015. DOI: 10.18429/JACoW-IBIC2015-TUPB015.
- [41] Falastine Abusaif. “Development of compact highly sensitive beam position monitors for storage rings”. In: *Hyperfine Interact.* 240.1 (2019), p. 4. DOI: 10.1007/s10751-018-1543-x.
- [42] Frank Rathmann and Nikolai N. Nikolaev. “Electric dipole moment searches using storage rings”. In: *PoS SPIN2018* (2019). Ed. by Paolo Lenisa et al., p. 004. DOI: 10.22323/1.346.0004. arXiv: 1904.13166 [nucl-ex].
- [43] Christian Bohme, Arthur Halama and Vsevolod Kamerdzhev. “COSY BPM Electronics Upgrade”. In: *5th International Beam Instrumentation Conference*. 2017, TUPG26. DOI: 10.18429/JACoW-IBIC2016-TUPG26.
- [44] Matjaž Žnidarčič. *Libera Hadron: Hadron Beam Position Processor, Specifications*. v1.02. Instrumentation Technologies. Velika Pot 22, SI-5250 Solkan, Slovenia, Feb. 2018.
- [45] *Control System Studio*. URL: <http://controlsystemstudio.org/>.
- [46] T. Wagner. *Gain Zero Search*. <https://gitlab.cce.kfa-juelich.de/BCC/BPM/GainZeroSearch>. 2019.
- [47] I. Bekman. *Gain Zeroing*. <https://gitlab.cce.kfa-juelich.de/BCC/BPM/beamposzero>. 2019.
- [48] G. Portmann, D. Robin and L. Schachinger. “Automated beam based alignment of the ALS quadrupoles”. In: *Conf. Proc. C 950501* (1996), pp. 2693–2695.
- [49] S. Ogur et al. “Beam-based alignment of the SuperKEKB linac quadrupoles”. In: *Nucl. Instrum. Meth. A* 925 (2019), pp. 199–211. DOI: 10.1016/j.nima.2019.02.018.
- [50] Saroj Kumar Jena et al. “Beam based alignment and its relevance in Indus-2”. In: *Rev. Sci. Instrum.* 86.9 (2015), p. 093303. DOI: 10.1063/1.4930277.
- [51] Naoki Hayashi et al. “Beam Based Alignment of the Beam Position Monitor at J-PARC RCS”. In: *Conf. Proc. C 100523* (2010). Ed. by Akira Noda et al., MOPE020.

- [52] Peter Röjssel. “A beam position measurement system using quadrupole magnets magnetic centra as the position reference”. In: *Nuclear Instruments and Methods in Physics Research Section A: Accelerators, Spectrometers, Detectors and Associated Equipment* 343.2 (1994), pp. 374–382. ISSN: 0168-9002. DOI: [https://doi.org/10.1016/0168-9002\(94\)90214-3](https://doi.org/10.1016/0168-9002(94)90214-3). URL: <http://www.sciencedirect.com/science/article/pii/0168900294902143>.
- [53] I. Barnett et al. “Dynamic beam based alignment”. In: *AIP Conf. Proc.* 333 (1995). Ed. by G. H. Mackenzie, B. Rawnsley and J. Thomson, pp. 530–535. DOI: 10.1063/1.48033.
- [54] L. Deniau et al. *The MAD-X Program - User’s Reference Manual*. English. Version 5.06.01. EUROPEAN LABORATORY FOR PARTICLE PHYSICS. Sept. 2020.
- [55] C. Weidemann and F. Trinkel. private communication.
- [56] T. Wagner et al. “Beam-based alignment at the Cooler Synchrotron COSY as a prerequisite for an electric dipole moment measurement”. In: *Journal of Instrumentation* 16.02 (Feb. 2021), T02001–T02001. DOI: 10.1088/1748-0221/16/02/t02001. arXiv: 2009.02058 [physics.acc-ph]. URL: <https://doi.org/10.1088/1748-0221/16/02/t02001>.
- [57] Vermessungsbüro Stollenwerk & Burghof. private communication. 50126 Bergheim, Aug. 2018.
- [58] Matjaz Žnidarčič et al. “Hadron BPM for the FAIR Project”. In: *6th International Particle Accelerator Conference*. 2015, MOPTY040. DOI: 10.18429/JACoW-IPAC2015-MOPTY040.
- [59] C. Böhme, V. Kamerdziev and F. Klehr. “Beam Position Monitors for the HESR”. In: *Annual Report 2014, Forschungszentrum Jülich* (2014).
- [60] Arthur Halama et al. “Numerical Comparative Study of BPM Designs for the HESR at FAIR”. In: *5th International Beam Instrumentation Conference*. 2017, WEPG01. DOI: 10.18429/JACoW-IBIC2016-WEPG01.
- [61] Jian-Dong Yuan et al. “Alignment of beam position monitors in cryomodule of CADS injector II”. In: *Nuclear Science and Techniques* 28.6 (Apr. 2017), p. 75. ISSN: 2210-3147. DOI: 10.1007/s41365-017-0232-9. URL: <https://doi.org/10.1007/s41365-017-0232-9>.
- [62] J. Niedziela, C. Montag and T. Satogata. “Quadrupole beam-based alignment at RHIC”. In: *Conf. Proc. C 0505161* (2005). Ed. by Charlie Horak, p. 3493.
- [63] G. Decker. “Beam Position Monitors: How to Meet the Specifications of Most Recent Accelerators”. In: *2nd International Beam Instrumentation Conference*. Feb. 2014, p. 623.
- [64] F. Abusaif et al. “Storage Ring to Search for Electric Dipole Moments of Charged Particles - Feasibility Study”. In: (Dec. 2019). arXiv: 1912.07881 [hep-ex].
- [65] Andreas Lehrach, Siegfried Martin and Richard Talman. “Design of a Prototype EDM Storage Ring”. In: *PoS SPIN2018* (2019). Ed. by Paolo Lenisa et al., p. 144. DOI: 10.22323/1.346.0144.

- [66] Saad Siddique. “Beam Simulation of a Prototype Proton Electric Dipole Moment Storage Ring”. MA thesis. RWTH Aachen University, 2019.
- [67] Maximilian Vitz. “Simulation and Optimization of the Spin Coherence Time of Protons in a Prototype EDM Ring”. MA thesis. RWTH Aachen University, 2020.
- [68] V. Anastassopoulos et al. *A Proposal to Measure the Proton Electric Dipole Moment with 10^{-29} ecm Sensitivity by the Storage Ring EDM Collaboration*. https://www.bnl.gov/edm/files/pdf/proton_EDM_proposal_20111027_final.pdf. 2011.
- [69] V. Anastassopoulos et al. “A Storage Ring Experiment to Detect a Proton Electric Dipole Moment”. In: *Rev. Sci. Instrum.* 87.11 (2016), p. 115116. doi: 10.1063/1.4967465. arXiv: 1502.04317 [physics.acc-ph].
- [70] B. Kulke et al. “A compact beam position monitor for use inside a free electron laser wiggler”. In: *Nuclear Instruments and Methods in Physics Research Section A: Accelerators, Spectrometers, Detectors and Associated Equipment* 272.1 (1988), pp. 241–246. ISSN: 0168-9002. doi: [https://doi.org/10.1016/0168-9002\(88\)90231-8](https://doi.org/10.1016/0168-9002(88)90231-8). URL: <http://www.sciencedirect.com/science/article/pii/0168900288902318>.
- [71] D. Noelle et al. “Precision alignments of stripline BPMs with quadrupole magnets for TTF2”. In: *Proceedings of LINAC 2004*. 2004, TUP69. URL: <https://accelconf.web.cern.ch/104/papers/tup69.pdf>.

List of Figures

2.1	Behavior of the EDM (\vec{d}) and MDM ($\vec{\mu}$) under parity transformation (\mathcal{P}) and time reversal (\mathcal{T}).	6
3.1	Depiction of coordinate system commonly used in accelerator physics.	10
3.2	Picture illustrating the general principle of focusing, taken from [25].	12
3.3	Pattern of the magnetic field of a quadrupole, taken from [25].	13
4.1	Schematic showing the accelerator COSY	19
4.2	Connections of main power supplies to straight section quadrupoles.	20
4.3	Connections of main power supplies to arc quadrupoles.	21
4.4	Illustration of a diagonally cut cylindrical BPM	21
4.5	BPM block diagram picture	22
4.6	Orbit correction main window	24
4.7	Orbit correction settings window	26
5.1	Gain adjustment interface	29
5.2	Screen capture of first version of gain calibration	31
5.3	Flowchart for decision making process during gain calibration	32
5.4	Screen capture of new gain calibration software	33
6.1	Simulated bump at the position of the quadrupole QT12	38
6.2	Simulated orbit distortion with changed quadrupole strength	39
6.3	Paraboloid fits of the simulated beam-based alignment	40
6.4	Measurement pattern May 2018 and February 2019	41
6.5	Example pictures of orbit bumps in November 2017	43
6.6	Parabola fit horizontal November 2017 measurement	44
6.7	Parabola fit vertical November 2017 measurement	44
6.8	Paraboloid fit November 2017 measurement	45
6.9	Fit example for one of the four measured sets in May 2018	47
6.10	Optimal position in QT12 measured in May 2018	47
6.11	Distributions for optimal position fit depending on number of points	49
6.12	Example fit for the measurement in February 2019 of quadrupole QT04	51
6.13	Comparison of all fits for quadrupole QT04	51
6.14	Optimal beam position inside the 12 quadrupoles with back-leg windings	52
6.15	Schematic of additional power supply connected to family of quadrupoles	54
6.16	Picture of connected additional power supplies	55

6.17	PV Display during the BBA measurement	56
6.18	Control Interface for BBA measurement	57
6.19	Measurement pattern for all quadrupoles	58
6.20	Example of a fit for the determination of the optimal position inside a quadrupole	59
6.21	Spread of quadrupole optimal positions for error determination	61
6.22	Zoomed in version of figure 6.21	62
6.23	Spread of measured optimal positions inside quadrupole QT04 and QU11	63
6.24	Example of BPM calibration in straight section of COSY	64
6.25	The optimal beam position in all quadrupoles	65
6.26	BPM calibration using all quadrupoles	66
6.27	Example of BPM calibration in straight section of COSY where one BPM had to be excluded	67
6.28	Example for Siberian Snake alignment measurement	70
7.1	Depiction of the Prototype Ring	73

List of Tables

2.1	Measured limits on EDMs for different particles	5
6.1	Explanation of the parameters of equation (6.1).	35
6.2	Comparison of the optimal position for different settings for the back-leg winding	45
6.3	Beam Position Monitor offsets from February 2019	53
6.4	Orbit and steerer RMS before and after calibration	68
6.5	Siberian Snake alignment measurement	70
A.1	BPM offset numbers	80
A.2	Mechanical alignment of COSY quadrupoles in the straight sections	81
A.3	Mechanical alignment of COSY quadrupoles in the arcs	82

Acronyms

ADC	Analog to Digital Converter
BBA	Beam-based alignment
BPM	Beam Position Monitor
COSY	Cooler Synchrotron
CPEDM	Charged Particle Electric Dipole Moment
CSS	Control System Studio
EDM	Electric Dipole Moment
EPICS	Experimental Physics and Industrial Control System
FAIR	Facility for Antiproton and Ion Research
GUI	Graphical User Interface
HESR	High Energy Storage Ring
IOC	Epics Input / Output Controller
JEDI	Jülich Electric Dipole moment Investigations
JePo	Jedi Polarimeter
JULIC	Jülich Isochronous Cyclotron
MAD-X	Methodical Accelerator Design
MDM	Magnetic Dipole Moment
ORM	Orbit Response Matrix
PV	Process Variable
RF	Radio Frequency
RMS	Root Mean Square
SCPI	Standard Commands for Programmable Instruments
SVD	Singular Value Decomposition
VGA	Variable Gain Amplifier
WASA	Wide-Angle Shower Apparatus

Eidesstattliche Erklärung

Ich, Tim Wagner,

erkläre hiermit, dass diese Dissertation und die darin dargelegten Inhalte die eigenen sind und selbstständig, als Ergebnis der eigenen originären Forschung, generiert wurden.

Hiermit erkläre ich an Eides statt

1. Diese Arbeit wurde vollständig oder größtenteils in der Phase als Doktorand dieser Fakultät und Universität angefertigt;
2. Sofern irgendein Bestandteil dieser Dissertation zuvor für einen akademischen Abschluss oder eine andere Qualifikation an dieser oder einer anderen Institution verwendet wurde, wurde dies klar angezeigt;
3. Wenn immer andere eigene- oder Veröffentlichungen Dritter herangezogen wurden, wurden diese klar benannt;
4. Wenn aus anderen eigenen- oder Veröffentlichungen Dritter zitiert wurde, wurde stets die Quelle hierfür angegeben. Diese Dissertation ist vollständig meine eigene Arbeit, mit der Ausnahme solcher Zitate;
5. Alle wesentlichen Quellen von Unterstützung wurden benannt;
6. Wenn immer ein Teil dieser Dissertation auf der Zusammenarbeit mit anderen basiert, wurde von mir klar gekennzeichnet, was von anderen und was von mir selbst erarbeitet wurde;
7. Ein Teil oder Teile dieser Arbeit wurden zuvor veröffentlicht und zwar in:
 - T. Wagner et al. "Beam-based alignment at the Cooler Synchrotron COSY as a prerequisite for an electric dipole moment measurement". In: *Journal of Instrumentation* 16.02 (Feb. 2021), T02001. DOI: 10.1088/1748-0221/16/02/t02001. arXiv: 2009.02058.
 - T. Wagner. "Results for Beam-Based Alignment at COSY". In: *Annual Report 2019, Forschungszentrum Jülich* (2019).
 - T. Wagner and J. Pretz. "Beam-based Alignment at the Cooler Synchrotron (COSY)". In: *10th International Particle Accelerator Conference*. (2019), THPGW024. DOI: 10.18429/JACoW-IPAC2019-THPGW024.

- T. Wagner. "Beam-based alignment tests at the Cooler Synchrotron (COSY)". In: *Hyperfine Interact.* 239.1 (2018), p. 61. DOI: 10.1007/s10751-018-1539-6.
- S. Merzliakov et al. "Correction of BPM electrical offsets and gain errors". In: *Annual Report 2018, Forschungszentrum Jülich* (2018).

Ort, Datum

Tim Wagner